Towards Rational and Sustainable Design of Graphitic Carbon Nitride for Antibacterial Applications

by

Nathália Aquino de Carvalho

Bachelor of Science in Environmental Engineering, Federal University of Paraiba, Brazil, 2014

Master of Science in Civil Engineering, University of Pittsburgh, 2017

Submitted to the Graduate Faculty of the

Swanson School of Engineering in partial fulfillment

of the requirements for the degree of

Doctor of Philosophy

University of Pittsburgh

2022

UNIVERSITY OF PITTSBURGH

SWANSON SCHOOL OF ENGINEERING

This dissertation was presented

by

Nathália Aquino de Carvalho

It was defended on

December 14, 2021

and approved by

Leanne M. Gilbertson, Ph.D., Associate Professor, Department of Civil and Environmental Engineering, Department of Chemical and Petroleum Engineering

Kyle J. Bibby, Ph.D., Professor and Wanzek Collegiate Chair, Department of Civil and Environmental Engineering and Earth Sciences, University of Notre Dame

Vikas Khanna, Ph.D., Wellington C. Carl Faculty Fellow and Associate Professor, Department of Civil and Environmental Engineering, Department of Chemical and Petroleum Engineering

Carla A. Ng, Ph.D., Assistant Professor, Department of Civil and Environmental Engineering

Dissertation Director: Leanne M. Gilbertson, Ph.D., Associate Professor, Department of Civil and Environmental Engineering, Department of Chemical and Petroleum Engineering

Towards Rational and Sustainable Design of Graphitic Carbon Nitride for Antibacterial Applications

Nathália Aquino de Carvalho, Ph.D.

University of Pittsburgh, 2022

Graphitic carbon nitride (g-C_3N_4) is an emerging visible-light-responsive photocatalyst with desirable antimicrobial activity. Considering synthesis choices that lead to competitive performance and minimize environmental and human health impacts is critical for developing g-C_3N_4 as an effective and sustainable disinfection alternative. This dissertation demonstrates the ability to rationally design g-C_3N_4 by chemical composition manipulations during synthesis, enabling control of g-C_3N_4 photocatalytic antibacterial response. Further, a life cycle assessment (LCA) of g-C_3N_4 syntheses offers concrete opportunities for the reduction of synthesis related impacts.

g-C_3N_4 properties that influence photocatalytic bacterial inactivation (i.e., band gap, intermediate defect states, dispersed surface area, absorbance in suspension, and charge separation) are compared across six samples modified using different synthesis temperature and carbon-doping. The effect of altering these material properties on the production of reactive oxygen species is investigated and linked to the ability to inactivate *Escherichia coli* bacteria. Results indicate that C-doping is an effective avenue to modulating g-C_3N_4 properties, and it induces variable levels of bacterial inactivation. C-doping is also successful in expanding g-C_3N_4 visible light range from 449 nm to 588 nm while maintaining a level of antibacterial activity.

To evaluate the sustainability of g-C_3N_4, a LCA is completed for predominant synthesis routes, and their environmental impacts are benchmarked to a competitive photocatalyst

alternative, titanium dioxide nanoparticles (nano-TiO_2). Results reveal energy demand during synthesis as the major contributor to the environmental impacts, highlighting opportunities to reduce the impacts through several suggested synthesis process modifications. The sustainability claim of g-C_3N_4 is found to depend on the particular synthesis route and underlying assumptions of the comparison to nano-TiO_2. Expanding the analysis of g-C_3N_4 to the use-stage shows benefits from activating g-C_3N_4 with visible wavelength light emitting diodes instead of ultraviolet (UV) wavelengths for nano-TiO_2. Given g-C_3N_4 high embodied resource footprint, any mass of g-C_3N_4 used for disinfecting drinking water to viral load reduction standards results in greater impact than UV disinfection.

Collectively, the research in this dissertation provides novel findings contributing to further development of g-C_3N_4 as a competitive sustainable antimicrobial, supporting rational design through synthesis modifications to control disinfection performance and reduce synthesis associated environmental impacts.

Table of Contents

List of Tables

List of Figures

Preface

As I sit to write this dissertation, I cannot help but reflect on the unforeseen journey I embarked when starting my PhD in the Fall of 2015, having just finished my undergraduate studies, coming from a different country, speaking a different native language, and being a hemisphere apart from my family and friends. That adventurous young woman ready for anything to come her way could not imagine that there would be a change in advisor and research focus, a husband, a daughter, a universal sickness, and other hardships between the start and finish line of this adventure. With the fog going away and my being able to see the end of the tunnel right now, I can honestly say it was all worth it and I would do it all again. It is a dream coming to reality, it is me making myself and my family proud. Six months ago, it also became my way of showing my daughter by example that she can achieve anything she wants. It has been six years filled with amazing friendships, personal development, and so much scientific learning.

I want to dedicate this dissertation to those who are my biggest motivation and give meaning to my life: my husband Luke, my daughter Anabella, and my mother Rebeca. They nourish me unconditionally with love and support, and to them there is no limit to what I can accomplish. They are my purpose and my guiding light.

I am so grateful for my brothers and my family and friends from Brazil that never made me feel distant even living so far away. They embraced this dream with me and were always available so I would never feel alone on this journey.

As I could not succeed alone, I want to thank all my friends from Benedum, especially Daniel, Alen, Omkar, Shardul, Vaclav, and Zhewei (Joey), for the long nights and days studying for classes and doing research, for eating lunch together, for always having my back, and for the many adventures and laughter we shared. They were surely a key part of my support system.

My dear friends Lisa and Yan deserve a special acknowledgement (now Dr. Stabryla and Dr. Wang!). They became my inspirations to grow as a hard-working and intelligent scientist. There was no bad weather when we were together. Lisa can brighten up my day with a smile, and Yan's advice is the best. They made my PhD journey lighter, and the experiences we shared have a special place in my heart. Our friendship is surely one I look forward to cultivating my whole life.

Words cannot express how much I appreciate my advisor, Dr. Leanne Gilbertson, for her role in my PhD path, and ultimately in my life. She has been a true mentor to me, providing support in times of need, celebrating my accomplishments, and guiding my professional development. She has been patient and kind when tough life challenges clouded my mind, giving me the courage and strength to keep going. More than that, she became a friend, one that is caring and wants the best for me and my family. I admire her as a scientist, as a woman, and as a mother. She is an amazing leader, intelligent and insightful researcher, and a role model to me.

Dr. Kyle Bibby was also critical in my growth as a scientist. It is thanks to him that I discovered my passion for microbiology. I want to thank him for welcoming me into PhD life with great disposition and eagerness to help me succeed. His encouragement and "let's just rip off the band-aid" attitude gave me the confidence I needed to share my scientific findings at conferences

and through written publications. I am so happy that we could continue working together even while in different research groups.

I would further like to thank Dr. Carla Ng and Dr. Vikas Khanna for accepting the invitation to be members of my committee. I respect and value their ideas and opinions and am grateful for their contributions to this dissertation. I am also thankful to them for the knowledge and experiences shared with me in classes, during the development of outreach activities, and during my teaching assistantship.

I also want to thank the Gilbertson Group and Bibby's Lab for welcoming me, teaching me in the lab, providing feedback so I could improve my work, and for all the fun we had together. A special thanks to Elyse for patiently sharing with me so much of what she knew when we worked together.

I would like to give a special shoutout to Dr. Radisav Vidic for inspiring and motivating me, and for believing in me as a teaching assistant. I love that outstanding TA award! I also want to thank Dr. Malehorn (Dave) for his sunny disposition to help with anything I ever needed in the lab.

Lastly, I am grateful for those who wrote recommendation letters for my PhD application and were amazing research advisors during my undergraduate studies: Elisângela Rocha and Steven Dentel (in memorian). I know they were key to my acceptance in the program, and I would not be here if it were not for them.

This is for you

Anabella, Luke, and Rebeca,

You are my everything.

xx

1.0 Dissertation Introduction

1.1 Motivation

1.1.1 The Use of and Need for Antimicrobial Agents

Antimicrobial agents are necessary for control and prevention of infectious diseases. The World Health Organization (WHO) reported in 2019 that at least 2 billion people worldwide depend on a drinking-water source that is contaminated with feces, and estimated 485,000 diarrheal deaths each year caused by drinking contaminated water.[1] Contamination of water is linked to the transmission of diseases that pose risk to human health (e.g., cholera, diarrhea, dysentery, hepatitis A, typhoid, polio) and remains a major public health concern. Conventional disinfection methods (e.g., chlorination, ozonation, ultraviolet irradiation) are effective in inactivating pathogens, but their applications are limited because of the harmful byproducts formed during disinfection, immense energy demands, expensive equipment requirements, and/or resistance in target pathogens.[2-4] Therefore, there is a pressing need to develop effective, stable, sustainable, and low-cost disinfectant technologies. Driven by challenges associated with water quantity, water quality and aging infrastructure, the global market for advanced technologies for municipal water treatment was valued at $12.8 billion in 2020 and expected to reach $20.5 billion in 2026,[5] highlighting the worldwide high investments in technologies to obtain clean water.

In addition to uses in water treatment, antimicrobial agents are widely applied to coatings.[6-8] Antimicrobial coatings aid in infection-control by eliminating disease-causing microorganisms on surfaces that otherwise serve as effective transmission pathways. Silver, copper, and titanium

dioxide (TiO_2) dominate this multi-billion-dollar industry, with primary applications found in medical and healthcare, food and beverage, building and construction, HVAC systems, protective clothing, and transportation sectors.[9] The global market for the antimicrobial coating industry was valued at $3.2 billion in 2020 and is expected to increase to $5.9 billion by 2026,[9] presenting further evidence of the need for antimicrobial agents as well as motivation to continue their development.

1.1.2 Photocatalysts as Antimicrobial Agents

Heterogenous photocatalysis was first reported by Fujishima and Honda in 1972, when they demonstrated photolysis of water on a TiO_2 electrode.[10] Since then, it has been widely explored and shows great potential to address global energy and environmental issues.[11-13] The global market for photocatalyst-based products is projected to generate nearly $5.1 billion in 2026, increasing from $2.9 billion in 2020, including antimicrobial applications across the environmental, consumer product, construction, automotive, and medical/dental industry sectors.[14] Preferred photocatalyst characteristics include visible-light activation (to avoid high energy requirements to initiate the process), chemical stability, efficient generation of photoinduced charges and subsequent transfer to the material surface, and economic viability for the desired application.[15]

The photocatalytic process consists of four main steps outlined in **Figure 1.1**: (I) energy of equal or higher magnitude than the optical band gap energy is absorbed by the photocatalyst exciting the electrons from the valence band (VB) to the conduction band (CB), forming electron-hole pairs; (II) partial recombination of generated electron-hole pairs occurs, releasing energy as heat; (III) photoinduced charges migrate to the surface of the photocatalyst; and (IV) excited

electrons and holes at the material surface serve as active sites for redox reactions, generating reactive oxygen species (ROS), such as hydroxyl radical (•OH), superoxide radical ($•O_2^-$), hydrogen peroxide (H_2O_2), and singlet oxygen ($^1O_2$).[16]

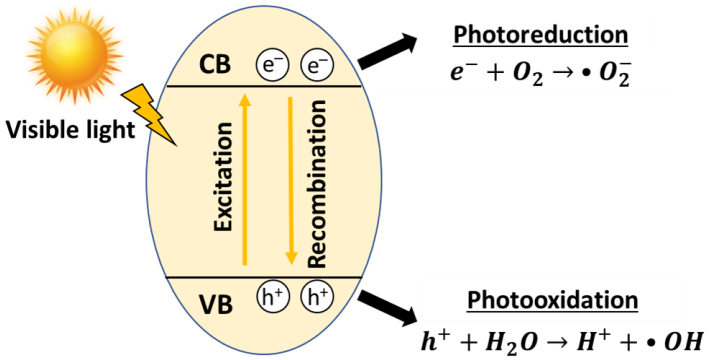

Figure 1.1. Schematic of the visible light photocatalytic process. CB = conduction band, VB = valence band, ROS = reactive oxygen species, e^- = electrons, h^+ = holes.

Photocatalysis has been extensively studied for antimicrobial applications (e.g., water and wastewater treatment and antimicrobial surface coatings), including bacteria (planktonic and biofilm) and viruses.[17-25] The generation of ROS by photocatalysis is crucial for microbial pathogen inactivation since ROS react with components of the cell that can lead to inactivation (e.g., by protein inhibition, DNA damage, and/or alteration in metabolism).[26-28] ROS generated by the photocatalytic process can inactivate pathogens effectively due to their high oxidizing power and fast disinfection kinetics. Since photocatalytic disinfection process occurs *in situ*, it eliminates challenges associated with transport, handling, and storage of strong oxidants. Further, visible-light-activated photocatalysts take advantage of a larger proportion of the solar spectrum (43% is in the visible region, 400 – 700 nm wavelength, as opposed to 9% for ultraviolet (UV), 280 – 399 nm wavelength[29]), reducing the energy and chemical footprint for the disinfection process.

TiO_2 is the most established photocatalytic material, with a global market value of $2.9 billion in 2020 and projected to reach $5.1 billion in 2026.[14] However, TiO_2 requires high energy UV light, limiting the utility of solar activation and necessitating higher cost (economic and energy) artificial light sources. Thus, there is an opportunity to contribute to the multi-billion-dollar photocatalyst global market with sustainable, visible-light-responsive photocatalysts.[30-32] Graphitic carbon nitride (g-C_3N_4) is emerging in this area as a non-metal, sustainable alternative to existing TiO_2-based, bismuth-based, carbon-based, ZnO-based, MoS_2-based, (oxy)nitrides-based, and oxysulfide-based visible-light-responsive photocatalyst candidates.[33,34]

1.1.3 g-C_3N_4 as a Promising Photocatalyst for Antibacterial Applications

g-C_3N_4 was first reported by Berzelius and Liebig in 1834, but it was in 2009 that it emerged in the photocatalysis field.[35] Since then, g-C_3N_4 research for photocatalytic applications has substantially increased (**Figure 1.2**). g-C_3N_4 was revealed in 2014 as a visible-light-responsive photocatalyst with bactericidal effects against *Escherichia coli* in liquid media.[36,37] The excellent antimicrobial potential of this material has been explored (**Figure 1.2 insert**) and confirmed for relevant pathogens such as methicillin-resistant *Staphylococcus aureus* (MRSA), *Salmonella, Staphylococcus aureus*, antibiotic-resistant bacteria belonging to *Enterobacteriaceae* family, and the bacteriophage MS2.[28,38-41] g-C_3N_4 has also been studied for applications in pollutant degradation, hydrogen evolution via water splitting, and carbon dioxide reduction.[42,43] Outside the realm of photocatalysis, it has applications in the fields of sensing, imaging, light-emitting devices, electrocatalysis, and energy storage and conversion.[44,45] The success of g-C_3N_4 in those applications fueled increased interest in its design for improved performance.

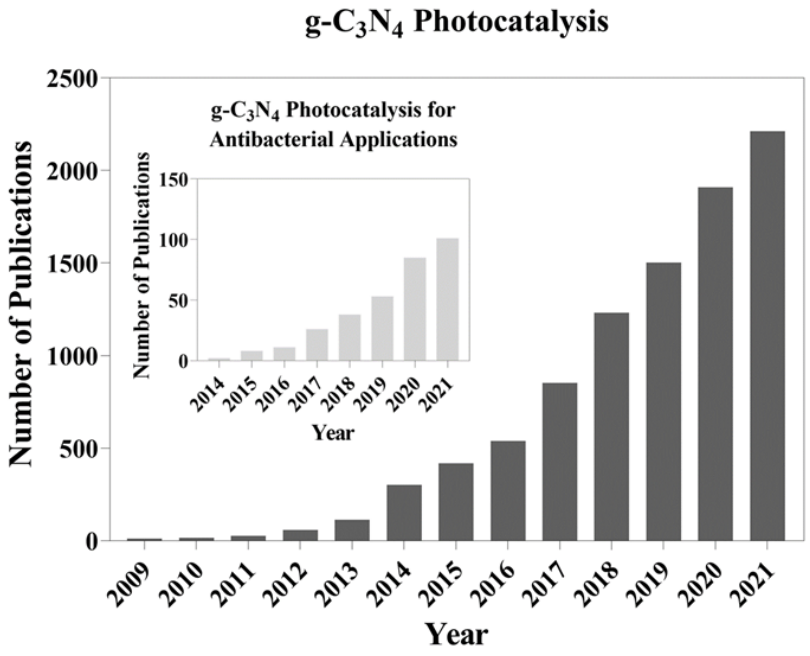

Figure 1.2. Journal publications reporting g-C_3N_4 photocatalysis by year. Search in Scopus using "carbon nitride" OR "g-C3N4" AND photocataly*. The inset refers to publications focusing on g-C_3N_4 photocatalysis for antibacterial applications, with search in Scopus using ("carbon nitride" OR "g-C3N4" AND photocataly*) AND (disinfect* OR *bacteria*).

The attractiveness of this emergent photocatalytic nanomaterial comes from its optical, electronic, and chemical properties, which can be tailored to modulate its photocatalytic activity.[16,46,47] g-C_3N_4 has a relatively facile synthesis from precursors that are earth-abundant and inexpensive (e.g., melamine, urea). Its chemical structure is composed of carbon and nitrogen atoms, making it a metal-free material. It has high thermal stability (i.e., resistant to air oxidation up to 600 °C), and chemical stability in both acidic and alkaline environments (e.g., insoluble in water, organic solvents, bases, and diluted acids), it is biocompatible in the dark, and presents very low inherent human toxicity.[48-50] Since the photocatalytic process primarily depends on the optical band gap of the material, the promise of bulk g-C_3N_4 as a visible-light photocatalyst emerges from

a band gap of 2.70 eV (i.e., the ability to absorb photons up to 460 nm).[51] There is also the ability to modulate the g-C_3N_4 band gap, with reported ranges from 1.80 – 2.88 eV,[52-55] indicating the potential to utilize 13 – 51 % of the solar spectrum (Air Mass 1.5 spectra, global total irradiance on the 37° sun-facing tilted surface).[29] Despite all of these advantages, the photocatalytic activity of bulk g-C_3N_4 is limited owing to low visible light utilization, low surface area, and fast charge recombination.[16,56] Thus, there is a need for research efforts aimed at modifying the g-C_3N_4 chemical structure to overcome these limitations and ultimately design a competitive photocatalyst for practical applications.

1.1.4 Rational Design for Tailoring g-C_3N_4 Antimicrobial Performance

g-C_3N_4 is composed of two-dimensional (2D) interconnected tri-*s*-triazine (heptazine) sheets (**Figure 1.3**),[57,58] The chemical composition of g-C_3N_4 can be manipulated for enhancing its photocatalytic performance.

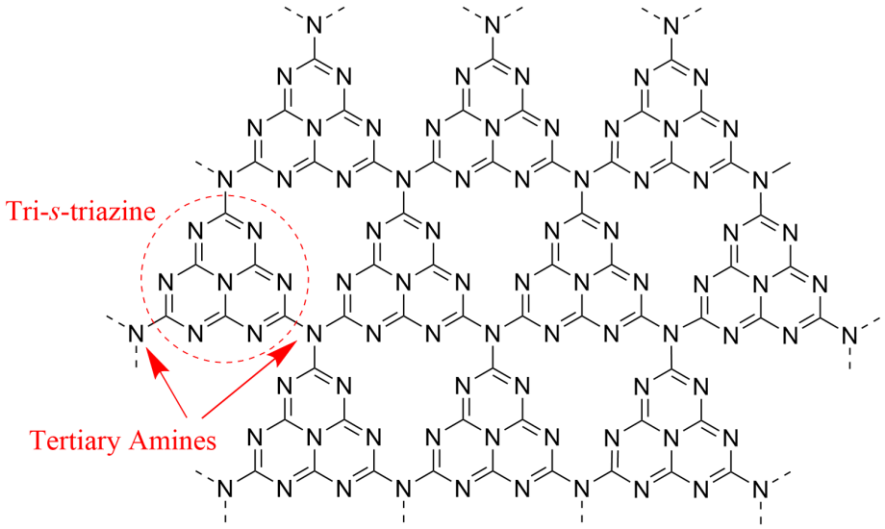

Figure 1.3. Tri-s-triazine (heptazine) structure of g-C_3N_4.

Changing the chemistry by doping or surface functionalization has been shown to enhance charge separation efficiency, increase surface area, properly position band energy locations, and raise visible-light absorption by reducing the band gap.[46,53,59-61] All of these properties contribute to ROS generation,[62] and have been shown to significantly affect g-C_3N_4 antimicrobial activity.[26,63,64] Band gap affects antimicrobial performance because it determines the available photon wavelengths for absorption necessary to generate electrons and holes,[52] and ultimately to produce ROS that react with bacteria to inactivate them.[26] Surface area is important for photocatalytic disinfection because it is linked to migration of the photogenerated electrons and holes to the material surface where it can interact with the environment to produce ROS.[65] Moreover, large surface area provides a higher number of active sites for hole generation, allowing more reactions to occur and enhancing the inactivation potential.[37] Charge separation efficiency is related to photocatalytic activity since production of electrons and holes are necessary for ROS generation. Therefore, it is desirable that these charge carriers remain separated (i.e., do not recombine) for as long as possible.[46] The thermodynamic ability of photocatalysts to produce ROS depends on the CB and VB potential positions relative to the redox potentials of the surface reactions.[60] For instance, oxidation occurs if the oxidation potential of the surface reaction is more negative than the VB potential. Similarly, it is only possible for reduction to be achieved if the reduction potential of the surface reaction is more positive than the CB.[16] Taking bulk g-C_3N_4 as an example, it is thermodynamically possible for this photocatalyst to directly produce $\bullet O_2^-$ via one-electron reduction of O_2 because its CB potential (-1.00 V versus normal hydrogen electrode (NHE)) is more negative than the redox potential of $O_2/\bullet O_2^-$ (-0.33 V versus NHE), but it cannot directly oxidize water to produce •OH on the VB because its VB (1.70 eV) is less positive than $\bullet OH/H_2O$ redox potential (2.32 V versus NHE). While mechanisms of ROS-driven g-C_3N_4

antimicrobial activity have been proposed,[15,36,39,66] there remains an opportunity to elucidate how to control the response based on manipulations of chemical composition.

Bulk g-C_3N_4 is composed of micron-sized multiple stacked layers and suffers from limited photocatalytic activity. Manipulations of g-C_3N_4-based materials for antibacterial applications are used to overcome this limitation and move towards developing g-C_3N_4 as an effective antimicrobial agent. Design strategies for modifying g-C_3N_4 structure have been investigated aiming to increase antibacterial activity and they include molecular doping (e.g., metal doping, non-metal doping, co-doping), nanostructure design (e.g., nanosheets, hollow nanospheres, nanopores, nanowires, nanozymes), and constructing heterojunctions (e.g., binary, ternary, Z-scheme).[42,67,68] Among these pathways to control bacterial inactivation through synthesis, there is a motivation to use non-metal doping to mitigate the potential release of toxic metals as well as eliminate the disadvantages of a high embodied resource footprint (e.g., raw material availability, energy demand associated with metal mining and refining).

While there are several options for non-metal dopants, a literature review on carbon-doping (C-doping) to alter g-C_3N_4 chemical composition highlights the ability to change material properties that affect photocatalytic performance (**Table 1.1**). C-doping is successful in extending visible-light absorption by narrowing the band gap, shifting VB and CB locations, increasing surface area, enhancing separation and transfer efficiency of the photoinduced electron-hole pairs while decreasing their recombination and increasing their lifetimes, and adding defect states (e.g., nitrogen vacancies). This literature review also drew attention to the fact that no study using C-doping as a tool to modify g-C_3N_4 chemical composition had investigated the effect of this synthesis method on the photocatalytic activity response against biological targets (e.g., bacteria and viruses). The promising potential of using C-doping to leverage g-C_3N_4 photocatalytic activity

coupled with the knowledge gap regarding its effect on bacterial inactivation propels research efforts addressed in this dissertation.

Table 1.1. Summary of the C-doped g-C_3N_4 literature showing the photocatalytic endpoints, and the C-doping effects on material properties that affect photocatalytic performance.

Photocatalytic Endpoint	C-doping effects on relevant photocatalytic material properties
H_2 production	Narrow band gap [69-73] Increase band gap [74] Change VB position [70-72,74] Change CB position [69-72,74] Increase charge separation efficiency [69-75] Enhance charge transfer efficiency [69-72,74] Decrease charge transport resistance [69,71,73] Reduce charge recombination rate [69,70,72,74] Increase charge carrier density [70,74] Increase electrical conductivity [71] Increase charge lifetime [74] Add defect states [74] Flatten Fermi levels [74]
Rhodamine B degradation	Narrow band gap [69,76] Change CB position but not VB [69] Shift the potentials of both VB and CB positively [76] Enhance charge separation and transfer efficiency [69,76] Decrease charge transport resistance [69] Reduce charge recombination rate [69] Increase electrical conductivity [76] Enhance photooxidation activity [76] Increase photoreduction activity [76] Increase photocurrent density [76]
Bisphenol A degradation [77]	Narrow band gap Change VB and CB positions Suppress charge recombination
NO removal [78]	Narrow band gap Boost the electron mobility and accelerate charge transport Suppress charge recombination

Table 1.1 (continued)

Gaseous benzene degradation [79]	Enhance light absorption ability Inhibit charge recombination Contribute to charge separation and transfer Improve electronic conductivity
4-Nitrophenol degradation [80]	Narrow band gap Enhance charge separation Improve the electronic conductivity Decrease charge transfer resistance
Sulfamethazine degradation [81]	Narrow band gap Decrease CB and slightly increase VB Inhibit charge recombination Increase the electrical conductivity and facilitate electron transfer
Methylene blue degradation [82]	Enhance visible-light absorption Decrease charge recombination rate Increase charge separation
X–3 B degradation [83]	Narrow band gap Raise VB and downshift CB Restrain charge recombination

1.1.5 Life Cycle Assessment as a guiding tool for sustainable design of g-C_3N_4

Assessing the embodied resources and associated impacts of engineered nanomaterials at early stages of development is critical for their sustainable development. Life cycle assessment (LCA) is an established methodology to determine the cumulative environmental and human health impacts of a defined system over its complete life cycle (i.e., raw materials extraction, manufacturing, use phase, and end of life), and it is guided by the ISO 14040 and 14044 standards.[84,85] This comprehensive tool can be used to determine the resource intensity of a nanomaterial synthesis (e.g., impacts of raw materials, precursors, processing energy, toxic inputs and/or emissions), which is critical to minimizing upstream impacts.

In addition to tailoring the chemical structure of g-C_3N_4 for increased photocatalytic performance, sustainable design can be achieved at synthesis through decisions surrounding precursors, reagents, equipment type, and processing time and temperature, for example. LCA studies comparing the environmental impacts of nanomaterials synthesized by different methods have identified high impact components of the material production, synthesis method tradeoffs, and thus, opportunities for reducing the overall impacts prior to scaling production.[86-88]

While g-C_3N_4 is proposed as a sustainable alternative photocatalyst,[36,64,89,90] there is no study to date that quantitatively supports these claims. Applying the LCA approach to g-C_3N_4 while it is in early stages of development will support proactive design of g-C_3N_4-based photocatalysts along more sustainable pathways before these nanomaterials are widely diffused into the market.

1.2 Dissertation Objectives and Organization

The overall objective of this dissertation is to guide the development of an effective and sustainable antimicrobial agent based on rational design of photocatalytic g-C_3N_4. Accordingly, this study is divided into two specific aims:

i) Inform rational design of g-C_3N_4 for antimicrobial applications by establishing the relationship between chemical composition, physicochemical properties that govern the mechanisms of photocatalytic performance, and bacterial inactivation efficacy. This was achieved by modifying g-C_3N_4 chemical composition by C-doping and investigating how this approach affects reactive species production by altering the

band gap, intermediate defect states, dispersed surface area, absorbance in suspension, and charge separation. This work is presented in Chapter 2.

ii) Uncover opportunities to reduce the resource footprint and associated environmental impacts of g-C_3N_4 syntheses, and assess g-C_3N_4 nanosheet sustainability by benchmarking its environmental impacts to a well-established photocatalyst. This was studied by using life cycle impact assessment to evaluate the environmental impacts of predominant g-C_3N_4 synthesis routes. This work is presented in Chapter 3.

This introductory chapter provides a brief introduction of the use of and need for antimicrobial agents, and presents photocatalysts as potential alternative antimicrobial agents. Chapters 2 and 3 focus on g-C_3N_4 as a potential sustainable alternative photocatalyst for antibacterial applications, offering concrete suggestions for rational design for improved performance and sustainability. An additional contribution to the published literature resulting from my PhD research addresses viral persistence in liquid media. More specifically, the evaluation of the bacteriophage Phi6 persistence in liquid media and its suitability as an enveloped virus surrogate (included in Appendices C and D). Finally, Chapter 4 summarizes major findings in this dissertation and proposes future research directions.

2.0 Using C-Doping to Identify Photocatalytic Properties of Graphitic Carbon Nitride that Govern Antibacterial Efficacy

Reprinted (adapted) with permission from:

Aquino de Carvalho, N.; Wang, Y.; Morales-Soto, N.; Waldeck, D.; Bibby, K.; Doudrick, K.; Gilbertson, L. *ACS Environmental Science &Technology Water* **2021**, 1, 2, 269–280. DOI: 10.1021/acsestwater.0c00053

Graphitic carbon nitride (g-C_3N_4) is a promising sustainable photocatalyst for bacterial disinfection. Herein, carbon-doping (C-doping) was employed to manipulate g-C_3N_4 physicochemical properties and demonstrate a potential avenue towards rationally designing g-C_3N_4 for improved antibacterial efficacy. Six g-C_3N_4 samples were prepared by thermal condensation with increasing amounts of barbituric acid (5-50% C-doping) and varying pyrolysis temperatures (550 and 600°C). Relationships between the synthesis approach, the resulting physicochemical properties, and the efficacy for bacterial inactivation are identified. C-doping was found to decrease the *E. coli* K12 inactivation rate, and the g-C_3N_4 synthesized at 550°C (base sample) was found to have the best photocatalytic performance. The results indicate significant *E. coli* inactivation with 5% and 15% C-doped samples, revealing that C-doping is an effective avenue to expand the visible light range of absorption while inducing disinfection. Further, the base sample is effective against clinically- and environmentally-relevant antibiotic-resistant pathogens, methicillin-resistant *Staphylococcus aureus* (MRSA) and vancomycin-resistant *Enterococcus faecalis*.

2.1 Introduction

The threats to human health that are posed by pathogens from water and solid surfaces remain significant.[91,92] Current control and prevention of bacterial infections requires disinfecting agents generated from chemicals (e.g., sodium hypochlorite) or high energy radiation (e.g., ultraviolet (UV) photons).[93] The transport, toxicity, formation of carcinogenic disinfection byproducts, high cost, and high energy challenges associated with these current approaches motivates the development of sustainable and cost-effective disinfection technologies.[94,95]

Disinfectants are used for a wide range of applications, including healthcare, water treatment, consumer product surfaces, and food packaging.[96-99] They are also incorporated into point-of-use and point-of-entry technologies to prevent exposure caused by recontamination of drinking water in the distribution system, contaminated well water, off-grid living, and space exploration.[100-102] The use of light to activate the production of disinfection agents, namely reactive species (RS), via photocatalysis is a promising alternative. Photocatalysis has been extensively studied for applications in drinking water and wastewater treatment as well as for antimicrobial surface coatings because of its demonstrated ability to inactivate bacteria, viruses, and microalgae,[19,103] suppress biofilm formation,[25,104] and degrade organic compounds[105,106]. Yet, the translation to commercial adoption has been inhibited by the (i) high cost associated with light sources for activation, (ii) low photoconversion efficiencies associated with high recombination rates of photogenerated electron-hole pair excitations, (iii) low-activity of visible-light active photocatalysts, and (iv) use of photocatalysts that are chemically unstable, composed of expensive elements, or made from toxic precursors.[107]

Graphitic carbon nitride (g-C_3N_4) is an attractive non-metal photocatalyst because it is synthesized from precursors that are abundant and cheap (e.g., melamine and urea), responsive to visible light, biocompatible in the dark, resistant to photo-corrosion and air oxidation, chemically stable in most solvents, presents very low toxicity to humans, and its optical properties can be manipulated.[48,49,62] g-C_3N_4 has demonstrated efficacy towards viral and bacterial inactivation,[28,108] chemical pollutants degradation,[16,109] cancer therapy,[110] water splitting, and CO_2 photoreduction[111,112] upon visible-light activation. Despite the aforementioned advantages, bulk g-C_3N_4 displays low photocatalytic activity arising from its poor visible-light absorptivity, low specific surface area, and fast charge recombination rate.[16,56] The photocatalytic performance of g-C_3N_4 can be improved by changing the synthesis temperature,[113] and through composition modifications, such as metal doping, non-metal doping, co-doping, and composite formation with other semiconductors.[114,115] These modifications aim to increase surface area, enhance visible-light absorption, alter the band energy locations, vary the abundance and type of catalytically relevant structural defects, and improve charge separation and transfer efficiency, which are the properties anticipated to increase photocatalytic activity.[46,53,115,116] Despite these efforts, there are conflicting accounts of g-C_3N_4 structure and composition that influence antibacterial efficacy, and this constrains *a priori* design of g-C_3N_4 materials for enhanced performance towards a given target (see **Table A.1** in Appendix A with compiled results on property-antibacterial activity relationships from studies of g-C_3N_4 used for photocatalytic bacterial inactivation in solution under visible-light irradiation).

Tailoring g-C_3N_4 chemical structure by carbon-doping (C-doping) has been explored for enhancing photocatalytic performance in chemical degradation and hydrogen production applications,[60,69-83,117-119] yet no study to date has investigated the effects of C-doping on

photocatalytic bacterial inactivation. Identifying the governing photocatalytic properties of C-doped g-C_3N_4 for antibacterial applications will uncover the possibility of translating the current knowledge of C-doped g-C_3N_4 photocatalytic activity across applications or add insight into how this approach influences antibacterial activity.

When a photocatalyst absorbs a photon of an energy greater than the band gap, it forms electron (e^-) and hole (h^+) pairs. Under irradiation, these photogenerated electrons and holes can migrate to the surface of the photocatalyst and react with surface bound species.[120] Through reactions with adsorbed water or oxygen, the h^+/e^- can form reactive oxygen species (ROS), including: hydroxyl radical (•OH), superoxide radical ($•O_2^-$), hydrogen peroxide (H_2O_2), and singlet oxygen ($^1O_2$). These ROS, h^+ (combined denominated RS), and e^- can inactivate bacteria through reactions with molecular components at its membrane surface as well as those internal to the bacterial cell (e.g., by lipid peroxidation, protein inhibition, DNA damage, and/or alteration in metabolism).[26-28,121] The ability to change g-C_3N_4 RS and e^- generation by manipulating its chemical composition (e.g., by C-doping)[62] suggests the potential to leverage this approach to gain control over properties that govern antimicrobial activity. While mechanisms of RS-driven g-C_3N_4 antimicrobial activity have been proposed,[15,36,39,66] less is known about the connection between the antimicrobial activity and the g-C_3N_4 material manipulations by C-doping. Discovering the relationships between g-C_3N_4 material properties that govern the mechanisms of photocatalytic antimicrobial performance and how those properties can be manipulated with the chemical composition will enable the rational design of this emerging, sustainable, photocatalytic material.

In this work, we investigate how changes in g-C_3N_4 chemical composition by C-doping alter the physical and chemical properties that affect RS production and consequently, the efficacy of inactivating bacteria. This was addressed by synthesizing six different g-C_3N_4 samples at

increased levels of C-doping and pyrolysis temperature. The properties important to photocatalytic activity were characterized, including band gap, intermediate defect states, dispersed surface area, absorbance in suspension, and charge separation. The antibacterial activity was examined by using *Escherichia coli* (*E. coli*) K12 as the model bacterium for all six samples, and the most reactive sample was further tested against clinically- and environmentally-relevant strains, methicillin-resistant *Staphylococcus aureus* (MRSA) and vancomycin-resistant *Enterococcus faecalis* (VRE). The systematic approach to modulating g-C_3N_4 chemical composition employed herein enables us to probe the properties important for enhancing the photocatalytic performance of g-C_3N_4.

2.2 Materials and Methods

2.2.1 Synthesis of Systematically Modified g-C_3N_4

g-C_3N_4 samples were synthesized by preassembly of triazine precursors, based on previously described methods.[60,75,122,123] The base sample, herein denoted as CN-550, was synthesized by thermal condensation of melamine (1 g) and cyanuric acid (in a 1:1 molar ratio) in a tube furnace (Thermo Scientific Lindberg/Blue M TF55035A-1). The precursors were dispersed into 40 mL of ethanol and the mixture was stirred at room temperature for 3 h. After stirring, the suspension was bath sonicated (VWR Scientific Aquasonic 150HT, sonic power of 135 W) at room temperature for 1 h and then dried at 70 °C on a hot plate in air until only a solid material remained. The solid was ground using an agate mortar and pestle to form a fine powder. Finally, the powder was transferred to a quartz crucible and placed into a tube furnace at 550 °C (4 h, 2.3 °C/min heating rate, under helium gas flow). C-doped samples (labeled C-CN) were synthesized with the same thermal treatment at 550 °C using precursors melamine, cyanuric acid, and

barbituric acid with different molar ratios, i.e., 1 (melamine) : x (barbituric acid) : 1-x (cyanuric acid), x = 5%, 15%, 20% , and 50%. To further investigate how increasing the carbon content in the chemical composition of g-C_3N_4 affects antibacterial activity, an additional sample (CN-600) was synthesized by changing the pyrolysis temperature. While C-doping increases C:N ratio in the g-C_3N_4 molecular structure by substituting nitrogen atoms by carbon atoms, elevating pyrolysis temperature generates nitrogen vacancies. For CN-600 preparation, the same approach as CN-550 was applied, but the temperature in the tube furnace was modified to 600 °C.

2.2.2 Characterization of g-C_3N_4

Powdered X-ray diffraction (XRD) data were collected with a Bruker D8 Discover instrument (Cu K_α radiation, 40 kV, 40 mA). Transmission electron microscopy (TEM) imaging was conducted on a JEOL JEM-2100F TEM operated at 200 kV. Surface chemical composition of all g-C_3N_4 samples were determined by X-ray photoelectron spectroscopy (XPS) using an ESCALAB 250Xi (Thermo Scientific) instrument with a monochromatic Al Kα X-ray source (1486.7 eV, spot size 650 µm). Methylene blue (MB) adsorption determined by loss in absorbance at 663 nm was used to determine the dispersed surface area of samples in solution. UV-Visible diffuse reflectance spectra were collected with a LAMBA-750 UV-Vis-NIR spectrophotometer (Perkin Elmer L750) equipped with a 60 mm integrating sphere using barium sulfate as the standard reference. Steady-state photoluminescence (ss-PL) spectra were obtained on a FluoroMax-3 spectrometer (Jobin Yvon Horiba) with excitation at a wavelength of 330 nm. Zeta potential was determined on a Litesizer 500 Particle Analyzer instrument (Anton Paar). Detailed methodological procedures of these characterization techniques are presented in the Appendix A.

2.2.3 Photocatalytic Activity

Details of light sources, irradiance measurements, photon flux, and photon fluence calculations are included in the Appendix A and **Figure A.1–A.3**.

2.2.3.1 Total Reactive Species Production

The photo-induced RS generated by the photocatalysts under visible-light irradiation were measured using carboxy-H_2DFFDA (ThermoFisher Scientific), which is a nonfluorescent molecule that is converted to a green-fluorescent form when the acetate groups are removed and it is oxidized by RS. Amongst the derivatives of reduced fluorescein used as indicators for total RS, the fluorinated analog carboxy-H_2DFFDA was chosen in this study because it exhibits improved photostability compared to the chlorinated fluorescein derivatives (DCF, DCFDA).[124] Although designed for intracellular assays, fluorescein derivatives have been used to measure extracellular total RS generated by photocatalysts, including g-C_3N_4.[23,63,64,125] To confirm the validity of this assay for the extracellular measurements needed in this study, a positive control was performed using hydrogen peroxide (**Figure A.4**). To measure total RS production of the g-C_3N_4 samples, a mixture of carboxy-H_2DFFDA dye (60 mM) and g-C_3N_4 materials (19 mg L^{-1}; bath sonicated for 1 h) dispersed in PBS (1 mM, pH 7.4) was added to a 96-well microplate with opaque black bottoms (Thermo Scientific 237105). The produced RS were quantified by measuring the dye fluorescence intensity with a Synergy HTX (Biotek) microplate reader before and after 5 minutes of visible-light irradiation. RS production was expressed as percent production:

$$\%\ RS\ production = \frac{(I - I_0)}{I_0} \times 100 \tag{2.1}$$

where I_0 and I are the dye fluorecence intensity (a.u.) before and after 5 minutes irradiation, respectively. The percent production was normalized by the photon fluence (photon cm^{-2}, calculation details in SI) to account for differences in absorbance of each g-C_3N_4 sample based on the respective optical band gap:

$$RS\ production = \frac{\frac{(I - I_0)}{I_0} \times 100}{Photon\ fluence} \quad (2.2)$$

Thus, the final units presented for RS production are % cm^2 $photon^{-1}$.

2.2.3.2 Bacterial Inactivation

E. coli K12 MG1655 (CGSC #7740) obtained from Yale Coli Genetic Stock Center (New Haven, CT, USA) was used as a model gram-negative bacterium to evaluate antimicrobial activity of the g-C_3N_4 samples. Overnight cultures were reinoculated in lysogeny broth (LB), incubated at 37 °C, and harvested at mid-exponential log phase. To remove residual growth-medium constituents from cell cultures, the mid-log phase cultures grown in LB were washed three times (centrifuged at 13,226 × g for 1 minute to pellet bacterial cells) and re-suspended in saline solution (0.9% NaCl). The g-C_3N_4 samples (400 mg L^{-1}) dispersed in saline solution were bath sonicated for 1 h before being exposed to the bacteria. Because saline solution is isotonic in nature and maintains the osmotic pressure of the cells, it was used for the suspensions and dilutions containing bacteria to preserve their integrity and viability.

For the photocatalytic disinfection experiments, light from a 300 W Xenon light source (Sciencetech SLB300B) equipped with a bandpass filter (Sciencetech HPF-BP-VIS-FT-3) was focused onto a beaker containing 10 mL of g-C_3N_4 (400 mg L^{-1}) mixed with 100 µL of bacterial solution (final concentration of ~10^7 colony forming units (CFU) mL^{-1}) for 2 h at room temperature

(~22 °C) under constant stirring at 200 rpm using a magnetic stirrer. Dark control experiments were conducted in the absence of light, and light control experiments were conducted using visible-light irradiation without the photocatalyst, both under otherwise identical conditions. The suspensions were sampled at times of 0, 0.5, 1, 1.5 and 2 h, and the number of viable cells was determined by using the CFU counting method. Briefly, 100 µL of serial dilutions of the bacterial suspension were spread on LB agar plates and incubated for 17–20 h at 37 °C for CFU enumeration. *E. coli* concentration at each time point was expressed as $\log_{10}(N/N_0)$ vs. the photon fluence, where N is the bacterial concentration in CFU mL^{-1} at the sampling times, and N_0 is the bacterial concentration in CFU mL^{-1} before exposure to visible light. *E. coli* was considered inactivated when the theoretical limit of quantification (LOQ, 200 CFU mL^{-1})[126] was reached, and this value was assumed for bacterial observations below the LOQ for data analysis. All treatments were performed at least three times. Saline solution was used for serial dilutions. All materials and chemicals used for antimicrobial activity experiments were sterile.

Methicillin-resistant *Staphylococcus aureus* USA300[127] and vancomycin-resistant *Enterococcus faecalis* V583 (ATCC 700802)[128] were used as clinically- and environmentally-relevant antibiotic-resistant gram-positive bacteria. These photocatalytic bacterial disinfection experiments were performed with the following modifications. MRSA experiments were carried out by re-inoculating overnight cultures into LB and monitoring growth until the cultures reached an OD_{600nm} of ~0.600–2.3. VRE experiments were carried out with cultures grown overnight to an OD_{600nm} ~0.600. Cultures were centrifuged at 17,000 × g for 1 minute to pellet cells, the supernatants were removed, and the cell pellets resuspended in 1 mL of 0.9% NaCl to normalize to an OD_{600nm} of 1.0. Photocatalytic activity was monitored every 10 minutes for a total of 30 minutes (VRE) or 40 minutes (MRSA). The number of viable cells was determined by spotting 10

μL spots of serial dilutions from each time point. Bacteria were considered inactivated when no colonies were observed.

2.2.3.3 Methylene Blue (MB) Degradation

The irradiation setup was the same as that used for *E. coli* inactivation. For the photocatalyzed MB degradation reaction, 7.5 mL of g-C_3N_4 (final concentration 400 mg L^{-1}, dispersed in saline solution, bath sonicated for 1 h) was mixed in a beaker with 7.5 mL of MB solution (final concentration 20 mg L^{-1}, dissolved in saline solution). Before light irradiation, the suspensions were stirred in the dark for 2 h to allow for MB adsorption equilibrium to be reached (2 h was determined by monitoring absorbance over time and receiving two consecutive readings with no change in absorbance), during which constant magnetic stirring was maintained at 200 rpm. At each sampling time, an aliquot of the solution was added to centrifuge tubes and centrifuged twice for 5 minutes at 13,226 × g to remove the solid particles. The supernatant was used to monitor the changes in MB concentration by measuring its light absorbance at 663 nm using a UV-Vis spectrophotometer (Thermo Scientific Evolution 201). MB degradation was expressed as $\ln(C/C_0)$ vs. the photon fluence of each photocatalyst, in which C is the concentration of the MB solution at the sampling time, and C_0 is the MB concentration before light irradiation. The light control was conducted under visible-light irradiation without photocatalyst.

2.2.3.4 Data Analysis

GraphPad Prism version 8.3 (La Jolla, California, USA) was used to assess the difference in the photocatalytic activity between the g-C_3N_4 samples. One-way ANOVA with Tukey's multiple comparison test was used to compare more than two treatments. The significance level used was 95% (i.e., $P < 0.05$ was considered statistically significant). Moreover, linear regression

models were obtained for bacterial inactivation and MB degradation (**Table A.2–A.4**). Bacterial inactivation and MB degradation first-order rate constants were obtained from the slope of the linear regression of $\ln(N/N_0)$ and $\ln(C/C_0)$ vs. time plots, respectively (**Table A.2–A.4**). The reaction rate constants were reported with respect to the photon flux, in units of cm^2 $photon^{-1}$ (i.e., the first-order rate constant, in s^{-1}, divided by the photon flux associated with each photocatalyst, in photon s^{-1} cm^{-2}) since the reaction rate depends on exposure time.

Additional methodological details can be found in the Appendix A, including materials and chemicals, characterization of g-C_3N_4 (XRD, TEM, XPS, dispersed surface area determination, g-C_3N_4 absorbance in solution, band gap and Urbach energy determination, zeta potential), and photocatalytic experimental and calculation details.

2.3 Results and Discussion

2.3.1 Characterization of g-C_3N_4 with Varying Chemical Composition

g-C_3N_4 is composed of two-dimensional (2D) sheets of tri-*s*-triazine interconnected by tertiary amines,[57,58] and it presents two main nitrogen configurations, denoted N_{2C} and N_{3C},[113,129,130] which refer to nitrogen atoms bonded to two carbon atoms in the aromatic ring and to nitrogen atoms bonded with three carbon atoms, respectively, as depicted in **Figure A.5**. The structure of g-C_3N_4 was manipulated in this research by C-doping and thermal treatment, and these materials were comprehensively characterized to study their physicochemical properties and their relative performance for inactivating bacteria.

The XRD patterns of 15% C-CN, CN-600 and CN-550 (**Figure A.6**) indicate that C-doping and thermal treatment do not influence the crystallinity. All three samples show one distinct broad peak around 26°, which is associated with (002) interplanar stacking of the conjugated aromatic system to generate a sheet-like structure.[131,132] The commonly observed (100) diffraction peak at 13°, corresponding to the in-plane ordering of tris-s-triazine units,[113,133] is not evident in the data. This fact indicates that the prepared samples are disordered, presumably because of defects generated in the growth of g-C_3N_4 with the addition of cyanuric acid and barbituric acid.[60] Further morphological characterization of CN-550 by TEM (**Figure A.7**) shows its sheet structure with visible pores embedded in the nanosheets, in agreement with literature reports.[60,123]

The chemical composition of g-C_3N_4 samples was studied by XPS and the findings are summarized in **Table 2.1**. Changes in C:N ratio confirm the successful manipulation of chemical composition through differing sample syntheses. There is a progressive increase in C:N ratio with an increasing extent of C-doping. Further, the 600 °C pyrolysis temperature alters the C:N ratio, confirming it is a successful alternative approach to manipulating g-C_3N_4 chemical composition. N1s spectral deconvolution (**Figure A.8**) reveals two dominant N-types, the divalent N atom (N_{2C} of the C–N=C in the aromatic ring, ~398.7 eV) and the trivalent N atom (N_{3C}, tertiary nitrogen N–(C_3) groups, ~400.4 eV).[60,134,135] For C-doped samples, the XPS data indicate that carbon atoms were more likely to be incorporated into the g-C_3N_4 structure through replacement of N_{2C} nitrogen rather than N_{3C} nitrogen. Comparison of the CN-550 and CN-600 data (**Table 2.1**) reveals that the N_{2C}:N_{3C} and N_{2C}:C (N_{2C} intensity) atomic ratios decrease with increased pyrolysis temperature, as has been noted by others,[55,116] suggesting that the increase in C:N ratio is caused by N vacancies generated at N_{2C} sites.

Table 2.1. X-ray photoelectron spectroscopy (XPS) data for four carbon-doped g-C_3N_4 samples and two g-C_3N_4 samples prepared under different pyrolysis temperatures (550 and 600 °C). Surface atom ratios determined from quantitative analyses are provided.

Sample	C:N	% C–N=C (N_{2C})	% N–(C_3) (N_{3C})	N_{2C}:N_{3C}	N_{2C}:C
CN-550	0.69±0.03	70.56±0.07	24.49±0.12	2.88±0.02	1.73
5% C-CN	0.75±0.01	70.54±0.29	24.63±0.24	2.86±0.04	1.65
15% C-CN	0.83±0.01	70.41±0.13	24.59±0.16	2.86±0.02	1.56
20% C-CN	1.02±0.02	69.82±0.21	25.85±0.03	2.70±0.01	1.38
50% C-CN	1.15±0.03	67.84±0.30	27.11±0.13	2.50±0.02	1.27
CN-600	0.73±0.00	68.90±0.14	27.08±0.14	2.54±0.02	1.64

CN = carbon nitride, CN-### indicates the pyrolysis temperature with melamine and cyanuric acid as the precursors, #% indicates the molar percent of barbituric acid over melamine (modified from g-C_3N_4 synthesized at 550°C).

2.3.2 Changes in Chemical Composition Alter g-C_3N_4 Photocatalytic Properties

Surface area is an important metric for photocatalytic efficacy as it affects the number of available active sites for ROS generation and the likelihood that electron-hole pairs generated can migrate to the surface active sites.[37,65] Given that the g-C_3N_4 interacts with bacteria in solution, we quantified the dispersed surface area using an MB adsorption assay. The results indicate that dispersed surface area differences are not a major factor affecting the photocatalytic activity variation of the g-C_3N_4 samples studied herein (**Figure A.9**).

Optical absorption and band gap of the g-C_3N_4 samples were determined (**Table 2.2**). Kubelka-Munk absorption *F(R)* plots for all samples (**Figure 2.1a**) show absorption bands centered at wavelengths of ~260 and ~360 nm. Using the Tauc plot method,[136,137] the indirect band gap of all samples was determined (**Figure 2.1b, Table 2.2**). The optical band gap of CN-550 was

determined to be 2.76 eV and is in accord with similarly prepared g-C_3N_4 materials reported elsewhere.[60,122] Increasing the level of C-doping and the pyrolysis temperature decreased the optical band gap, as has been reported by others.[52,53,59] The combined data indicate that an increase in C:N ratio decreases the band gap of g-C_3N_4. The band gap agrees well with the color profiles of the prepared samples, i.e., they change from light yellow to dark red with decreasing band gap (**Figure A.10**).

Table 2.2. Optical band gap, maximum wavelength of absorption, and Urbach energy of the prepared g-C_3N_4 samples.

Sample	Band gap (eV)	Maximum wavelength of absorption (nm)	Urbach energy (eV)
CN-550	2.76	449	0.10
5% C-CN	2.59	479	0.22
15% C-CN	2.11	588	0.21
20% C-CN	1.73	715	0.21
50% C-CN	1.67	742	0.19
CN-600	2.55	486	0.26

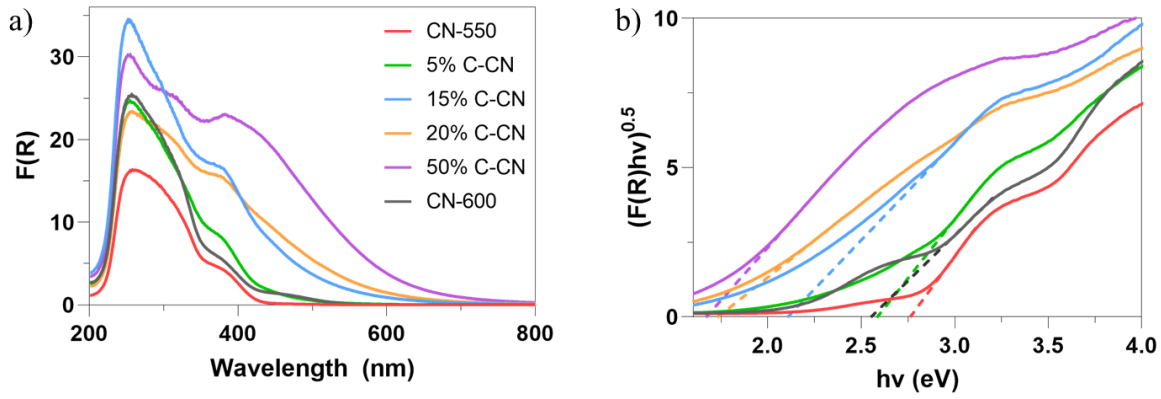

Figure 2.1. (a) Optical absorbance spectra of the g-C_3N_4 samples (obtained from UV-Vis DRS reflectance and modified by Kubelka-Munk function) showing higher absorbance in the visible region upon increasing C:N in the chemical structure of the nanomaterial. (b) Optical band gap of the g-C_3N_4 samples obtained by Tauc plots. The legend applies for both (a) and (b).

To further investigate the optical properties of the g-C_3N_4 materials, the Urbach energy (E_u) was determined (**Table 2**). E_u is associated with the Urbach absorption tail below the optical band gap of the samples and emerges from intermediate defect states (i.e., electronic states existing within the band gap that can accommodate photoexcited electrons from the valence band).[138,139] These intermediate defect states are formed by structural defects in the material (e.g., uncondensed NH/NH_2, nitrogen vacancies).[116] Higher band-tail absorption is observed for g-C_3N_4 with increased pyrolysis temperature, indicating the presence of more intermediate defect states that are mostly nitrogen-related, and levels of C-doping, as previously reported.[60,116] E_u increases upon C-doping, but it remains fairly consistent (slight decrease from 0.22 to 0.19 eV) with increased percent C-doping. This consistency may occur because C atoms substitute N_{2C} atoms during C-doping with no significant change in nitrogen defects. Increasing the number of intermediate defect states could improve the photocatalytic activity as long as these trap sites are located near the surface and remain active for ROS generation. Note that the photocatalytic activity depends on the type of defect formed (e.g., cyanamide defects may improve photocatalytic activity,[46] whereas amino/imino group defects act as recombination centers and may inhibit photocatalytic activity[140]) and the abundance of defects (e.g., there might be an optimum level of nitrogen deficiency to obtain high photocatalytic performance).[55] Moreover, the amount and type of catalytically relevant defects present in the g-C_3N_4 material vary with synthesis conditions.[46,55] While we observe a change in E_u for our samples indicating the relative presence of intermediate defect states, further characterization (e.g., Positron annihilation spectroscopy (PAS),[116] Raman spectroscopy, Fourier transform infrared spectroscopy (FTIR)[46,133,140]) is needed to determine the vacancy-type defects and catalytically relevant functional groups.

Charge separation efficiency is an important metric for photocatalytic activity because the separated charge carriers (e^- and h^+) are necessary for RS generation.[46] The ss-PL spectra arises from radiative electron-hole pair recombination (i.e., photon emitting), with a lower peak intensity indicating higher nonradiative (i.e., charge carrier trapping and nonradiative recombination) decay rates. The ss-PL peak intensity decreases with increasing C-doping from 5% to 50% and increasing pyrolysis temperature from 550 to 600 °C (**Figure 2.2**). Assuming that 100% of the excitation photons (at a wavelength of 330 nm) are absorbed for each photocatalyst, these results indicate that the replacement of N_{2C} with C and introduction of N_{2C} defects in the g-C_3N_4 structure reduces the radiative recombination. The negligible photoluminescent intensity of 50% C-CN is assumed to result from the lack of light absorbance in solution (spectra are compiled in **Figure A.11**) rather than signaling low recombination. For the C-doped samples, the redshift in the peak is presumably due to the intermediate defect states formed from doping that allow a lower energy photon transition. As indicated by the Tauc plot analysis (**Figure 2.1b**), these photocatalysts have an indirect band gap. The majority of recombination in an indirect band gap photocatalyst (e.g., TiO_2) occurs via a nonradiative pathway (i.e., phonon transitions that release heat).[141] Further, because this is a steady-state analysis, it does not capture the lifetime of the charge carriers. This is a critical feature when considering the transfer of the charge carriers to the photocatalyst surface for subsequent interaction with reactants.[108,116]

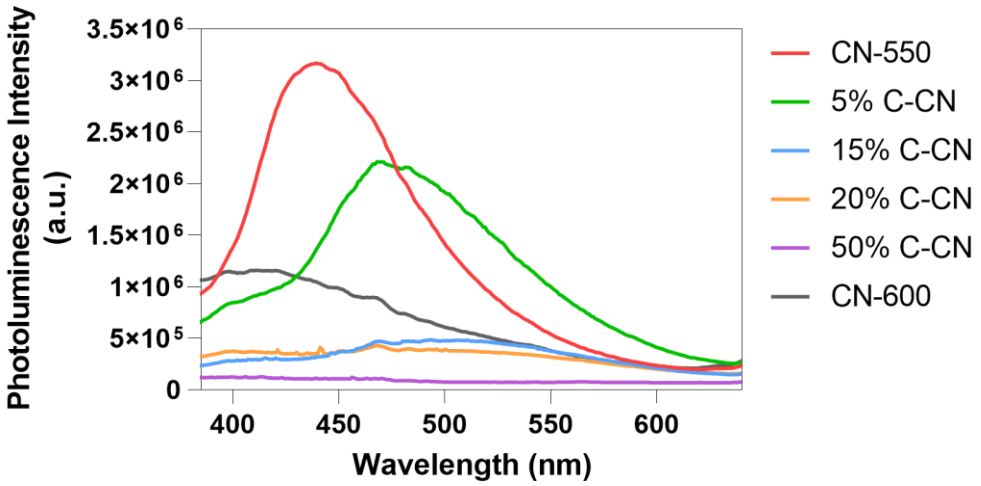

Figure 2.2. Steady-state photoluminescence (ss-PL) emission spectra of g-C_3N_4 samples (19 mg L^{-1}) in suspension at excitation wavelength of 330 nm.

2.3.3 Changes in g-C_3N_4 Physicochemical Properties Affect Reactive Species (RS) Production

In photocatalysis, the reduction of O_2 at the e^- sites and oxidation of H_2O at h^+ sites occur concurrently on the photocatalyst surface according to the stepwise reduction of O_2 generating $\bullet O_2^-$, H_2O_2, and $\bullet OH$, and the stepwise oxidation of H_2O forming $\bullet OH$, H_2O_2, $\bullet O_2^-$, and $^1O_2$.[142] We assess the total RS generated by the g-C_3N_4 samples under visible-light irradiation using carboxy-H_2DFFDA as a probe molecule. Carboxy-H_2DFFDA becomes fluorescent when oxidized thus, the measured total RS includes ROS and h^+, which have demonstrated direct interaction with bacteria.[143,144] Excited e^- are not accounted for in this assay. The results (fluorescence intensity) are normalized by photon fluence (**Figure 2.3;** non-normalized plot in **Figure A.12**) to present a comparison of RS production efficiency respective to the sample light absorbance capacity.

Total RS production (% cm^2 $photon^{-1}$) decreases by 85% with C-doping (i.e., for 50% C-CN) and 35% upon increasing the pyrolysis temperature. Thus, even though the samples with a smaller band gap absorb more photons than those with larger band gaps under visible-light irradiation (as observed in the absorbance measurements, **Figure 2.1a**), they produce fewer RS. The decrease in RS production with a decrease in band gap indicates a lower charge transfer efficiency to the aqueous reactant or charge carrier trapping in states without the redox potential needed to generate RS. In addition, the RS yield displays a positive correlation with the ss-PL emission spectra, in which higher ss-PL intensity indicates more electron-hole pair recombination, but CN-550 produces the most RS while having the highest ss-PL intensity. This phenomena has been observed in others' studies where C-doped g-C_3N_4 had higher ss-PL intensity and greater photocatalytic performance towards contaminant degradation compared to the reference sample.[60,140] The positive correlation with ss-PL intensity indicates that the lifetime of the photogenerated carriers is important for the RS generation. That is, reducing intrinsic nonradiative decay pathways in the g-C_3N_4 material results in a higher population of charge carriers at energies that can promote RS generation. Given the relative time scales of recombination (femto- to nano-seconds)[141] and ss-PL data collection (>100 ms), our results do not directly address whether e^-/h^+ trapping occurs before a RS-producing reaction occurs. For example, increasing C-doping may reduce the overall radiative recombination, but the introduction of intermediate defect states may also decrease the charge carrier lifetime. Though steady-state radiative recombination is not a comprehensive characterization for determining RS production for g-C_3N_4, it highlights the importance of considering nonradiative recombination as a key characteristic.

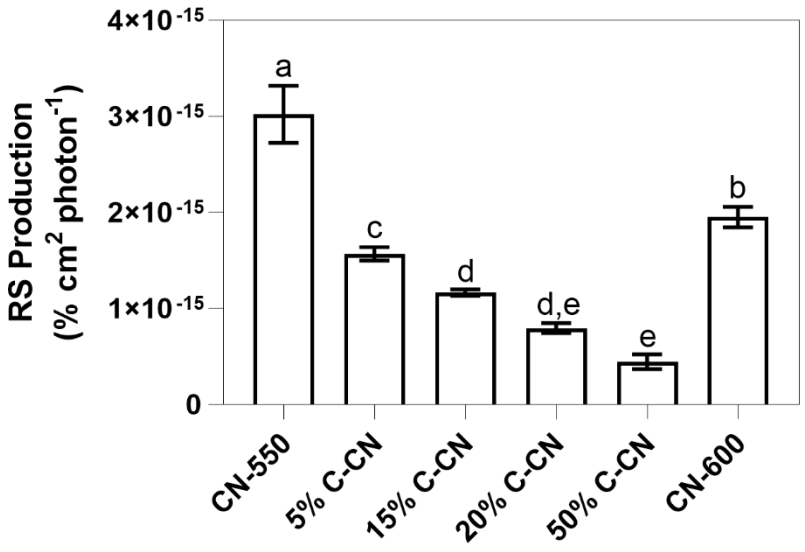

Figure 2.3. Reactive species (RS) production by the g-C_3N_4 samples after 5 minutes of visible-light irradiation normalized by the photon fluence associated with each sample. Means suffixed with different letters (a–e) are significantly different from each other ($P < 0.05$). Error bars indicate standard deviation (n=3).

The thermodynamic ability of photocatalysts to produce ROS depends on the position of the valence band (VB) and conduction band (CB) relative to the redox potentials of the surface reactions.[60] For example, a given surface oxidation reaction will occur if the oxidation potential is more negative than the VB maxima. Similarly, it is only possible for reduction to be achieved if the surface reaction reduction potential is more positive than the CB minima.[16] For the C-doped samples, a previous DFT study showed that VB and CB locations can change and depend on the substituted nitrogen site (i.e., N_{2C} or N_{3C}).[60] Additionally, previous reports suggest that the VB position is not affected by the introduction of nitrogen defects into g-C_3N_4,[55,145] which indicates that the redshift in the CN-600 band gap arises from shallow trap states near the CB band edge (mobility edge). This suggests that both synthesis modifications could suppress $\bullet O_2^-$ production

via the one-electron reduction of O_2 when the CB is more negative than the redox potential of $O_2/\bullet O_2^-$,[60] decreasing the total RS production.

2.3.4 Linking Photocatalytic RS Production to Bacterial Inactivation

Bacterial inactivation by the g-C_3N_4 samples confirms that photocatalytic antimicrobial activity varies across samples with different chemical composition (**Figure 2.4**, and vs. time in **Figure A.13**). The insignificant inactivation observed in the dark and light controls demonstrate the biocompatibility of the photocatalysts in the dark and negligible inactivation from visible light alone over the experiment duration. The trends of *E. coli* K12 inactivation rate constants normalized and non-normalized by photon flux (**Figure A.14**) indicate the relative number of photons and time required to achieve bacterial log reduction, respectively. The non-normalized data (**Figure A.14b**, h^{-1}) may distort the material's efficacy because it assumes that all samples receive the same photon flux, misleading one to conclude that the antibacterial performance of some g-C_3N_4 samples are higher than they actually are (e.g., 5% C-CN performs better than 15% C-CN for the data normalized by photon flux, but not for the non-normalized). The inactivation rate constant normalized by photon flux (**Figure A.14a**, cm^2 $photon^{-1}$) demonstrates that CN-550 has the best antibacterial photocatalytic activity followed by 5% C-CN (69% slower than CN-550) and 15% C-CN (84% slower than CN-550). 20% C-CN, 50% C-CN and CN-600 induce no bacterial inactivation (i.e., are not significantly different from the light control).

RS production has been determined to be the main pathway for photocatalytic disinfection,[19,146] therefore, the activity toward a target microorganism should correlate with the amount of RS produced (**Figure A.15**). For the C-doped samples, the trend for *E. coli* K12 inactivation rate constant is in accordance with the trend observed in total RS production;

decreased RS production correlates with decreased inactivation. CN-600 does not follow the same trend; this sample has lower log inactivation than expected from the RS production results. This outcome suggests that chemical composition, here the carbon-to-nitrogen ratio, alone is not responsible for the differing photocatalytic performance. While we are unable to fully resolve this discrepancy, possible explanations are the (i) type of defect present (N vacancy for CN-600 vs. C replacing N for C-doping) that results from different modification approaches, (ii) type of ROS produced by g-C_3N_4, and (iii) charge separation and transport phenomena. In addition to the total amount of RS, g-C_3N_4 samples can produce different ROS types[60] (e.g., based on the energy bands location, pH of the system). Different ROS possess different potency towards bacterial inactivation (e.g., hydroxyl radical is believed to be the most potent[147] yet is very short lived compared to other species, a tradeoff that should be considered with future work to uncover the type of RS produced). Quantifying the relative amount of specific type of RS produced by different g-C_3N_4 samples is a topic of our ongoing research and may explain the unexpectedly low CN-600 inactivation. Finally, assuming that the mechanism of inactivation is the same for each sample, the results provide evidence that the charge recombination rate increases with increasing C-doping and pyrolysis temperature, and that the time it takes to inactivate *E. coli* K12 is longer than the charge recombination rates of the 20% and 50% C-CN samples. Overall, radiative recombination may be decreasing with increased C-doping and pyrolysis temperature of g-C_3N_4, but this may be concomitant with increased rates of charge recombination, precluding charge transport to the surface.

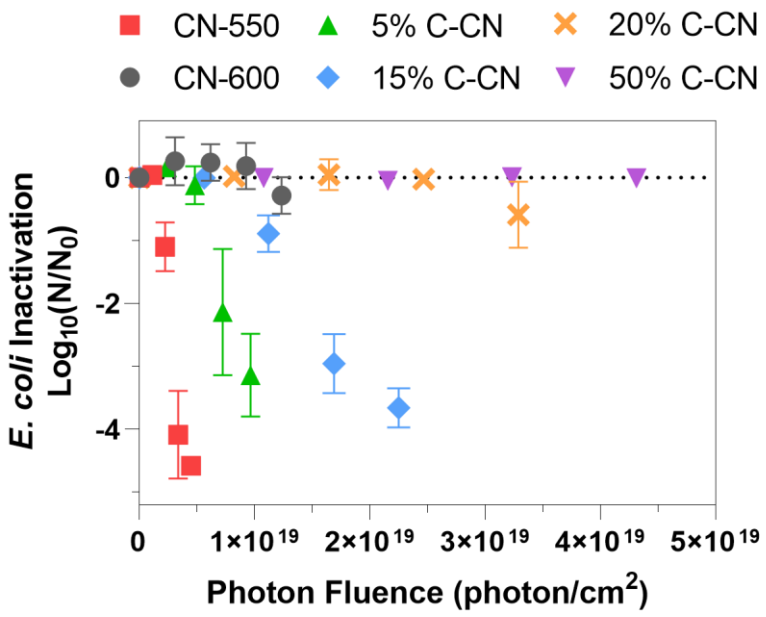

Figure 2.4. Photocatalytic inactivation efficiency against *E. coli* K12 (~10^7 CFU mL^{-1}, 10 mL) in the presence of different g-C_3N_4 samples (400 mg L-1) under visible-light irradiation (400 < λ < 700 nm) in terms of the photon fluence associated with each sample. Error bars represent standard deviations (for CN-550 n=4, for others n=3).

To determine if the low performance of CN-600 is unique to bacterial inactivation, we investigated the relative performance of the g-C_3N_4 samples in a chemical reaction pathway that is well-studied in photocatalysis – the photocatalytic oxidation of MB[65] (vs. photon fluence in **Figure A.16,** vs. time in **Figure A.17**). The MB degradation photon fluence normalized for CN-600 aligns more closely with what is expected based on total RS production in that appreciable oxidation of MB is observed. Yet, the relative magnitude of MB degradation for CN-600 compared to 5% C-CN remains lower than expected based on their relative RS production (CN-600 produces significantly greater total RS than 5% C-CN, **Figure A.15**). The discrepancy between bacterial inactivation and MB degradation could result from different interactions of MB and *E. coli* K12 with CN-600 since photocatalytic activity can be improved by more efficient adsorption between

the bacteria (negative surface charge) or MB (cationic dye molecule) and photocatalyst. However, the surface charges of all our g-C_3N_4 samples are negative with similar magnitude (-25.15 to -31.25 mV), as indicated by their zeta potential (**Table A.5**) tested under the experimental conditions (aqueous solutions, pH 5–6). Thus, we would not expect to see a difference in relative magnitude of bacterial inactivation and MB degradation for CN-600 performance in these two systems.[148,149] Instead, the results indicate that structural defects introduced to the CN-600 sample by the thermal treatment process somehow inhibit antibacterial activity rather than promote it – further research is required to resolve this observation. These results suggest that the approach to modifying chemical composition (C-doping vs. pyrolysis temperature), rather than chemical composition alone (e.g., as C:N), influence the photocatalytic performance. Increasing carbon content directly correlates with decreasing the band gap, but the effect of chemical composition on RS production, bacterial inactivation, and MB degradation involves a more complex system of mechanisms, which could be related to the types and amount of defects in the g-C_3N_4 framework. Together, the results reveal that C-doping is an effective avenue to expand the visible light range of absorption while inducing variable levels of bacterial inactivation.

While material properties that improve photocatalytic activity are known, predicting the structure and compositions that generate those properties represents a grand challenge, and often optimal performance can require a balance between properties. The differences observed in the samples' properties, RS production, *E. coli* K12 inactivation, and MB degradation, underscore these challenges and highlight the complexity of g-C_3N_4 photocatalytic performance. This is most notably observed in our study by the superior *E. coli* inactivation and MB degradation performance of CN-550, which possesses the largest band gap (does not increase light harvesting), lowest E_u (does not provide a high density of intermediate defect states), and highest radiative charge

recombination. These findings for our set of samples are demonstrated in **Table 2.3**, which compares properties of the best and one of the lowest performing materials, CN-550 and 20% C-CN, respectively. Even though 20% C-CN possesses properties that should theoretically promote higher photocatalytic activity, its performance includes 74% less RS production, 99% lower *E. coli* inactivation, and 84% lower MB degradation than CN-550.

Table 2.3. Property and performance comparison of CN-550 (highest performing sample) and 20% C-CN (lower performing sample), within the context of the full sample set. Highest/lowest indicate the sample with respect to all six g-C_3N_4 samples. Higher/lower indicate the comparison between CN-550 and 20% C-CN.

Property	Expected level for highest performance	CN-550	20% C-CN
Band gap	Low	Highest	Lower
Urbach energy	High	Lowest	Higher
Charge recombination (ss-PL)	Low	Highest	Lower
Dispersed surface area[a]	High	No Sig. Difference[b]	Highest
Absorbance in suspension	High	Lower	Higher
Performance			
RS production	High	Highest	Lower
E. coli inactivation	High	Highest	Lower
MB degradation	High	Highest	Lower

[a] 20% C-CN dispersed surface area is statistically greater than the other five samples. The greatest difference is between 20% and 50% C-CN, which is 0.026 g of MB/g of g-C_3N_4.

[b] CN-550 does not have a significantly different dispersed surface area compared with the other four samples (5% C-CN, 15% C-CN, 50% C-CN and CN-600).

Collectively, the results reveal that (i) C-doping is an effective approach to modulating g-C_3N_4 properties, (ii) the inherent material properties influence the photocatalytic performance, and (iii) features of the chemical mechanisms (e.g., redox driving force) must be considered in the design.

2.3.5 Expanding Antibacterial Performance Evaluation of g-C_3N_4 to Environmentally- and Clinically-Relevant Strains

The best performing sample, CN-550, was tested on two additional bacterial strains: VRE and MRSA (**Figure 2.5**). The inactivation rate constant normalized by photon flux for *E. coli* K12, VRE, and MRSA are $-3.43\times10^{-11} \pm 3.34\times10^{-12}$, $-3.24\times10^{-12} \pm 9.54\times10^{-13}$, and $-3.13\times10^{-12} \pm 3.33\times10^{-13}$ (cm^2 $photon^{-1}$), respectively (non-normalized in **Table A.4**). The inactivation rates of MRSA and VRE are not significantly different from each other; however, they are significantly smaller than that for *E. coli* K12. These data indicate that gram-positive bacteria – MRSA and VRE – are more resistant to g-C_3N_4 antimicrobial activity than the gram-negative *E. coli* K12. The high variability of the MRSA replicates may be associated with the emergence of small-colony-variants, which are subpopulations resistant to oxidative stress.[150] Similar to other disinfectants, these results demonstrate that susceptibility to inactivation is dependent upon the microorganism. Future work is necessary to draw firm conclusions about the improved g-C_3N_4 inactivation performance for gram-negative over gram-positive microorganisms and to demonstrate sufficient inactivation ranges of environmental- and clinically-relevant targets and water matrices.

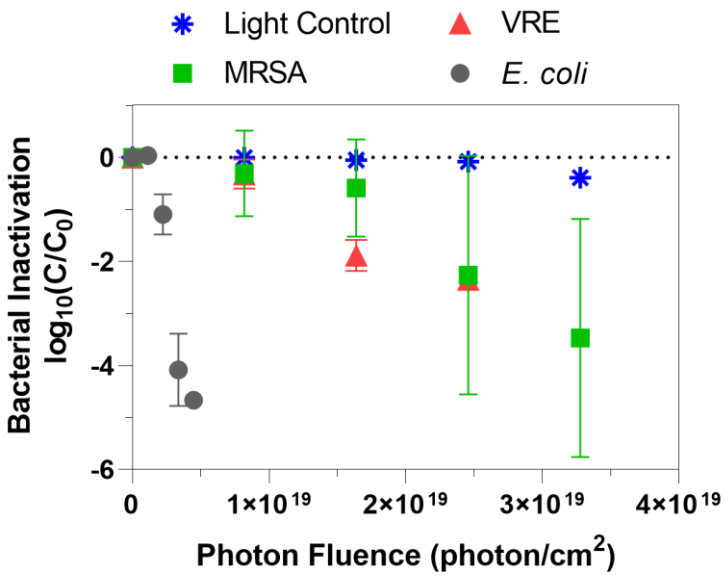

Figure 2.5. Photocatalytic inactivation of *E. coli*, MRSA and VRE by CN-550 sample irradiated with visible light ($400 < \lambda < 700$ nm) vs. the photon fluence associated with each experiment. Reaction mixture contains bacterial solution and g-C_3N_4 dispersed in saline solution (400 mg L^{-1}). Light control contains bacterial solution and saline solution without photocatalyst. Error bars indicate standard deviation (for *E. coli* n=4, for others n=3).

2.4 Conclusion

While g-C_3N_4 has emerged as a promising photocatalyst for inactivating microorganisms, there remains an opportunity to uncover how to tune physicochemical properties for enhancing performance in disinfection applications. This work used C-doping to extend g-C_3N_4 absorbance to longer wavelengths and evaluated its photooxidative properties and antibacterial efficacy. A systematically modified set of C-doped g-C_3N_4 samples was successfully synthesized by thermal polycondensation of melamine, cyanuric acid, and barbituric acid. Results herein demonstrate that, although C-doping of g-C_3N_4 samples does not promote higher *E. coli* inactivation compared to the base sample (CN-550), C-doping up to 15% still induces disinfection while extending the range

of visible-light absorption. This finding highlights C-doping as a possible synthesis route for leveraging lower energy, economically favorable light sources, although further investigation is necessary to confirm the efficiency of such systems (e.g., testing C-doped g-C_3N_4 antibacterial activity using low energy light sources). Additionally, our results indicate that g-C_3N_4 surface chemistry modulation by C-doping influences antibacterial performance differently from what has been reported for chemical degradation and hydrogen production (i.e., C-doping improved the photocatalytic activity of g-C_3N_4 for chemical degradation and hydrogen production but not for bacterial inactivation).[60,72-74,82,118] This finding can inform future research focusing on chemical modification of g-C_3N_4 for disinfection applications. Moreover, the results establish the efficacy of CN-550 for inactivating model gram-negative *E. coli* and representative environmentally- and clinically-relevant gram-positive MRSA and VRE under visible light only, despite the tradeoff of having the largest optical band gap. Interestingly, photocatalytic performance measured as RS production, bacterial inactivation, and MB degradation does not trend as expected with anticipated properties previously identified to improve g-C_3N_4 photocatalytic activity. This suggests that the correlation between visible-light-driven photocatalysis, RS production, and bacterial inactivation by g-C_3N_4 is complex. Further research (e.g., additional chemical composition manipulation approaches and advanced characterization techniques) is needed to establish structure-property-function relationships and resolve mechanisms of inactivation, further informing rational design of g-C_3N_4. This study is the first to evaluate C-doped g-C_3N_4 for antibacterial applications, and our findings inform future work aiming to optimize disinfection by g-C_3N_4. For example, analysis of low energy light sources (e.g., LED) and sunlight as well as optimizing photocatalyst concentration and reaction time.

3.0 Comparative Life Cycle Assessment of Graphitic Carbon Nitride Synthesis Routes

This Chapter has been submitted to the Journal of Industrial Ecology:

Aquino de Carvalho, N.; Gilbertson, L. M. Comparative. Submitted to the *Journal of Industrial Ecology*.

Graphitic carbon nitride (g-C_3N_4) has gained great interest as a visible-light-activated photocatalyst. As an emerging nanomaterial for environmental applications, its competitive performance and environmentally responsible synthesis are critical to its success. A powerful tool for informing material development with reduced environmental impacts is life cycle assessment (LCA). In this study, LCA is used to evaluate the environmental impacts of g-C_3N_4 nanosheet produced via eight existing synthesis routes. The results reveal electricity as the main contributor to the cumulative impacts of all eight g-C_3N_4 syntheses. There are opportunities to reduce energy demand, and consequently the synthesis impacts, by revising synthesis procedures (i.e., removing or reducing time of use of an equipment), optimizing the calcination step (i.e., faster heating rate, lower heating time, lower temperature), and moving to cleaner electricity sources. Further, benchmarking the environmental impacts of g-C_3N_4 nanosheets to a well-established metal-based photocatalyst, titanium dioxide nanoparticles (nano-TiO_2), reveals mixed comparative results. The synthesis method and the assumptions made to enable equivalent functional unit comparison both substantially influence the comparative impacts. Considering use-phase benefits of activating g-C_3N_4 with visible wavelength light emitting diodes compared to ultraviolet (UV) wavelengths for

nano-TiO_2 results in a 52% energy demand reduction (in kWh). Performance of g-C_3N_4 compared to a high-energy disinfection approach (i.e., conventional UV) reveals an inability to meet drinking water disinfection standards for viral load reduction (4-log reduction) with any mass of g-C_3N_4, given its high embodied resource footprint. This work establishes a foundation to inform and direct g-C_3N_4 nanosheets towards improved sustainable development.

3.1 Introduction

The global market for photocatalyst-based products is expected to reach US$ 5.07 billion by 2026, expanding at a compound annual growth rate of 10.5% since 2020, with most sales attributed to construction (89% share of the 2020 total market) and consumer products (7.7% of the 2020 total market) sectors.[151] While the global photocatalyst industry is dominated by titanium dioxide (97.8% of the 2020 global revenues, US$ 2.81 billion),[151] several alternatives are emerging in the search for higher photocatalytic efficiency, particularly under visible-light irradiation. Graphitic carbon nitride (g-C_3N_4) is one of these promising alternatives. g-C_3N_4 is a visible-light-responsive photocatalyst that is demonstrated for a wide range of applications, including photocatalytic water splitting, carbon dioxide photoreduction, degradation of chemical pollutants, and viral and bacterial inactivation.[44,48,152]

g-C_3N_4 has been proposed as a sustainable photocatalyst due to numerous attractive properties, including its synthesis from metal-free precursors, responsiveness to visible light, resistance to photo-corrosion and air oxidation, high chemical stability in most solvents, reusability, and low human toxicity.[20,49,153] g-C_3N_4 can be synthesized with different morphologies. Bulk g-C_3N_4 is readily prepared with nitrogen-rich precursors such as melamine,[74]

urea,[154] cyanamide,[37] dicyandiamide,[81] and thiourea[155] by a one-step, thermal process. It is composed of micron-thick particles having multiple stacked layers,[156] and its properties (poor visible-light absorptivity, low specific surface area, and fast charge recombination rate[16,21]) limit photocatalytic performance. With growing interest in g-C_3N_4, efforts have been made to tailor its physicochemical and optical properties to improve photocatalytic efficiency.[21,157] Synthesis modifications of the bulk form enable attainment of nanosheets,[158] quantum dots,[159] hollow nanospheres,[122] microtubes,[160] and microrods.[156] Two-dimensional nanosheets are the most commonly used form of g-C_3N_4 reported in the literature and are therefore, chosen as the focus of this study. The properties and photocatalytic performance of g-C_3N_4 can be altered by changing precursors (e.g., melamine, urea) and the synthesis approach (e.g., exfoliation, and non-metal doping). These process modifications result in production of nanosheets with different surface area, optical band gap, band energy locations, charge separation efficiency, abundance and type of catalytically-relevant structural defects.[115,158,161]

While g-C_3N_4 is proposed as a sustainable photocatalyst,[36,64,89,90] no study to date has quantitatively supported these claims. The goal of this seminal sustainability assessment of g-C_3N_4 is to establish a foundation to inform and direct its sustainable development. Life cycle assessment (LCA) is used to evaluate the environmental impacts of existing, predominant g-C_3N_4 synthesis processes. LCA studies of engineered nanomaterials and nanomaterial-enabled consumer products highlight the significant, and sometimes dominant, contributions of nanomaterial synthesis to the cumulative impacts due to extraction of raw materials to generate precursors and synthesis energy demand.[162-165] The high synthesis contributions emphasizes the value of integrating LCA early, concomitant with design and development of emerging materials, to direct decision-making that minimize impacts (e.g., precursor selection, solvent choice, synthesis approach). Results from such

analyses enable the identification of high impact components of the material production, synthesis route tradeoffs, material impact-performance tradeoffs, and opportunities to reduce the environmental footprint prior to scaling production.[166-169] This proactive approach enables competitive and environmentally responsible development of novel synthesis routes for manufacturing new materials.

Herein, we assess the life cycle impacts of synthesizing g-C_3N_4 nanosheets via eight distinct routes. The syntheses were chosen based on their prevalence in the literature, reported sustainability claims, and/or having the necessary information available to model the process. The contributions of our study include: (1) providing the life cycle inventory (LCI) data of eight g-C_3N_4 nanosheets synthesis routes, (2) their mass-based environmental impact profiles, (3) identifying the major impact contributions to pinpoint opportunities for reducing the environmental footprint, (4) analyzing how the assessment will evolve with transitions to renewable electricity sources, (5) benchmarking the environmental impacts of g-C_3N_4 nanosheets syntheses to nano-TiO_2 syntheses, including comparing their respective precursor impacts and the potential energy savings associated with using visible light versus ultraviolet (UV) light sources, and (6) establishing g-C_3N_4 performance targets for water disinfection by benchmarking to UV disinfection. The data and results generated in this study offer concrete design opportunities that inform the reduction of synthesis impacts and identify the potential of g-C_3N_4 nanosheets to replace or augment existing disinfection alternatives.

3.2 Methods

3.2.1 Scope and System Boundary

The life cycle environmental impacts of eight g-C_3N_4 nanosheet synthesis routes were assessed. A mass-based functional unit of one gram of g-C_3N_4 nanosheets was chosen due to the focus on synthesis as well as the wide range of applications of g-C_3N_4 (i.e., a performance-based functional unit would be limited to a specific use). The cradle-to-gate system boundary (**Figure 1**) considers environmental impacts associated with upstream resource extraction and energy for the syntheses of precursors and reagents, as well as impacts of energy generation and direct emissions for g-C_3N_4 nanosheet syntheses.

Life cycle impact assessment was performed using SimaPro 9.1 (PRé Consultants). The United States Life Cycle Inventory (USLCI) and US-EI databases were chosen when available; otherwise Ecoinvent 3 was selected.[170-172] The US-EI database is a combination of USLCI and Ecoinvent data, adjusted to be representative of United States operations. Environmental impacts were modeled using the United States Environmental Protection Agency's Tool for the Reduction and Assessment of Chemical and Other Environmental Impacts (TRACI) 2.1 assessment method.[173] Environmental impact categories include ozone depletion (OD, in kg CFC-11 equivalents, or eq), global warming potential (GWP, in kg CO_2 eq), photochemical smog formation (PS, in kg O_3 eq), acidification (AC, kg SO_2 eq), eutrophication (EU, kg N eq), human health impacts from toxic carcinogenic (HHC) and noncarcinogenic (HHNC) substances (in comparative toxic units for human toxicity impacts, or CTUh), respiratory effects (RE, in kg $PM_{2.5}$ eq), ecotoxicity (EC, in comparative toxic units for aquatic ecotoxicity impacts, or CTUe), and fossil fuel depletion (FF, in MJ surplus).

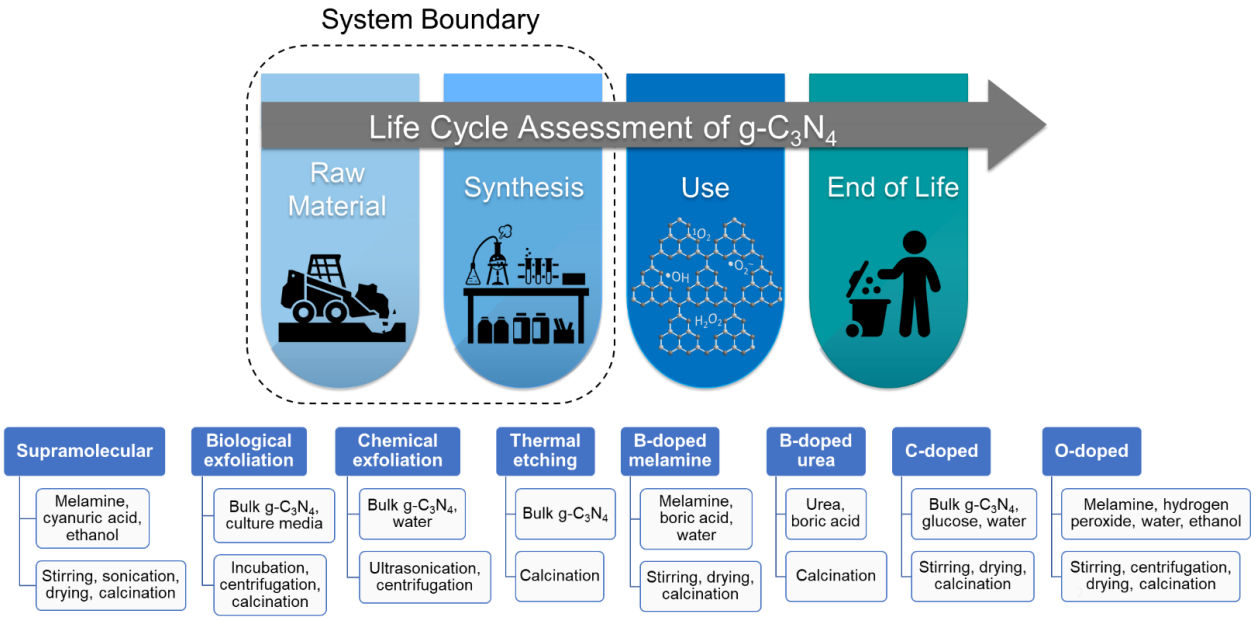

Figure 3.1. g-C_3N_4 nanosheet life cycle stages with the system boundary (cradle-to-gate) highlighted by the dashed lines. The eight synthesis routes are listed with their respective material inputs and energy-intensive processing steps identified.

3.2.2 Synthesis Routes

Eight synthesis routes were chosen to represent g-C_3N_4 nanosheets manufacturing processes: supramolecular, biological exfoliation, chemical exfoliation, thermal etching, B-doped melamine, B-doped urea, C-doped, and O-doped. Detailed information for each synthesis procedure and their respective LCIs are in the Supplemental Information (Appendix B, **Sections B.1.1–B.1.9** and **Tables B.1–B.9**). The g-C_3N_4 syntheses LCI were established based on published laboratory- scale investigations because information at the industrial scale is currently unavailable. The following criteria were considered for the selection of papers to represent each synthesis: the final product is g-C_3N_4 nanosheets and the synthesis is widely used (supramolecular[60,75,122,123,153]), has been suggested to be sustainable (biological exfoliation,[64] chemical exfoliation,[89,90] thermal

etching[36]), or involves non-metal dopants (e.g., boron,[174,175] carbon,[72] oxygen[176]). Further refinement of the literature revolved around availability of details necessary to model the processes. Bulk g-C_3N_4 serves as the precursor for the chemical exfoliation, biological exfoliation, thermal etching, and C-doped syntheses, and this process was built in SimaPro by the authors (based on References[36,64,72,89]) because it is not available in the databases.

Synthesis yields were not reported in the referenced papers. Therefore, the theoretical yields were calculated based on the reaction stoichiometry to allow for the comparison of environmental impacts across syntheses.

3.2.3 Uncertainty Analysis

Uncertainty analysis was performed using Monte Carlo simulation (1,000 runs, SimaPro 9.1) to assess the uncertainty of the cumulative unit process LCI data associated with each synthesis route. For unit processes available in the selected databases (i.e., US-EI, USLCI, Ecoinvent), the default lognormal distributions were used. For unit processes created by the authors, the uncertainty factors are calculated for each input and output data considering a lognormal distribution and utilizing the Pedigree matrix approach (details in **Tables B.1–B.9**).

3.3 Results and Discussion

3.3.1 Environmental Impact Assessment of Eight g-C_3N_4 Synthesis Routes Reveals Electricity as the Main Contributor to the Cumulative Impacts

Analysis of process contributions associated with producing 1 g of g-C_3N_4 nanosheets via the eight chosen syntheses reveals overwhelming contributions of electricity (**Figure 2b–i**) in all

ten mid-point impact categories (OD, GWP, PS, AC, EU, HHC, HHNC, RE, EC, and FF). The process contributions for the synthesis of bulk g-C_3N_4 are detailed separately because it serves as the precursor for four of the syntheses (**Figure 2a)**. Since bulk g-C_3N_4 is the precursor for biological exfoliation, chemical exfoliation, thermal etching, and C-doped routes, the substantial precursor contributions to their total impacts (represented by the red contribution in **Figure 2c–e, and h**) are predominantly from electricity for producing bulk g-C_3N_4 (over 89% of the impact in all categories).

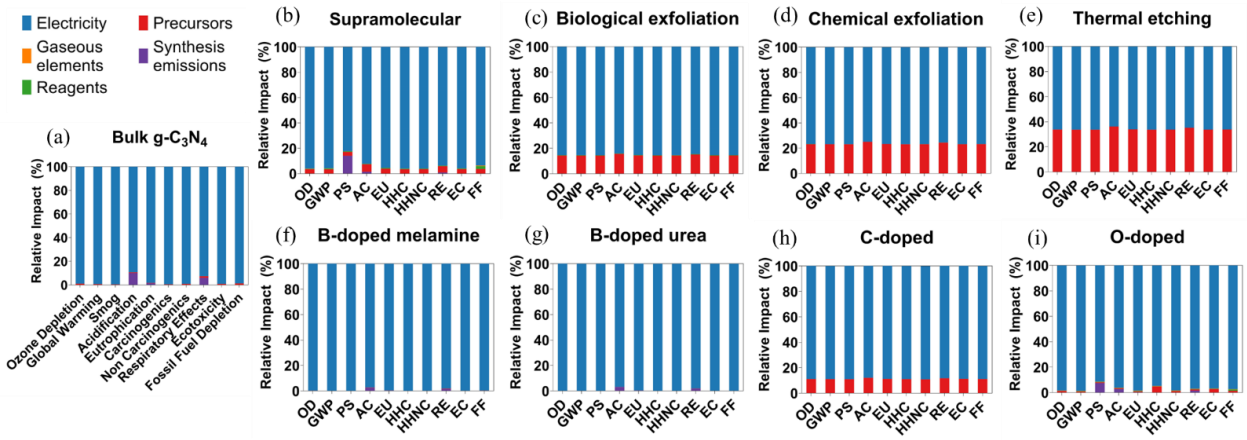

Figure 3.2. Process contributions associated with ten TRACI impact categories to produce 1 g of bulk g-C_3N_4 and 1 g of g-C_3N_4 nanosheets by eight synthesis routes. The abbreviated impact categories (x-axis) in (b) – (i) are equivalent to those in (a). Bulk g-C_3N_4 is the precursor for biological exfoliation, chemical exfoliation, thermal etching, and C-doped syntheses. The data are normalized to the highest value in each category to generate a relative impact.

The electricity input is a 2018 country mix from SimaPro, which is the most recent data available, and reflects electricity generation in the United States considering diverse energy sources (i.e., hard coal, oil, natural gas, nuclear, hydropower, wood, wind power, photovoltaic, geothermal, petroleum coke). When analyzing GWP, the main processes in electricity generation

that contribute to the environmental impacts are derived from natural gas and hard coal burned at the power plant. Since fossil fuels remain the largest U.S. electricity generation sources (natural gas generating about 40% and coal 19% of the US electricity in 2020[177]), the source of electricity (e.g., a more renewable electricity grid) will influence the synthesis environmental footprint.

3.3.2 Mass-Based Comparison of Eight g-C_3N_4 Nanosheet Syntheses

Since the trends in environmental impacts across all impact categories are the same, GWP (in CO_2 eq) is used as a representative category (**Figure 3**) to demonstrate the trend in impacts and identify the influencing synthesis parameters. Relative impacts for all categories can be found in **Figure B.1** and the associated absolute values in **Table B.10**. Uncertainty analysis results (associated with input parameters of the unit processes) are presented in **Figure B.2**.

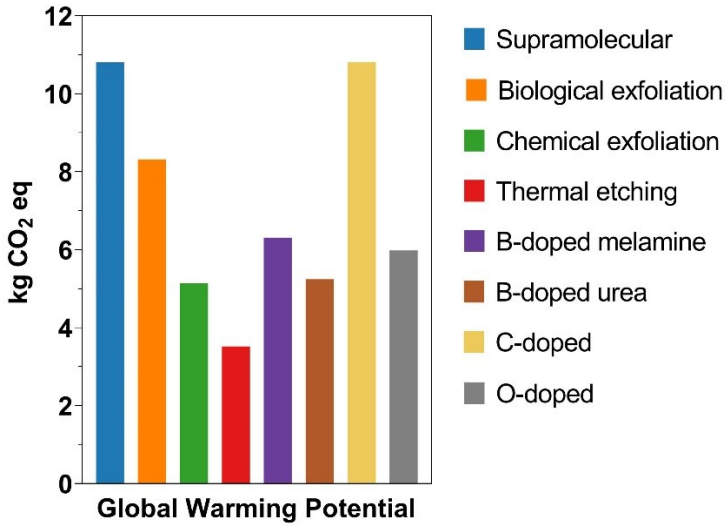

Figure 3.3. Absolute impacts associated with global warming potential (in kg CO_2 equivalents) of eight g-C_3N_4 synthesis routes when producing 1 g of g-C_3N_4 nanosheets.

Comparing the eight syntheses (**Figure 3**) indicates that manufacturing g-C_3N_4 nanosheets by the supramolecular and C-doped routes produce the highest environmental impacts followed by biological exfoliation, B-doped melamine, O-doped, chemical exfoliation and B-doped urea, and thermal etching. Electricity required during synthesis is the dominant contributor to the trend in relative impacts across the eight syntheses. The primary differences in electricity requirements for synthesizing g-C_3N_4 nanosheets by the highest impact routes include long drying time (16 h) for supramolecular and the long stirring and drying times (12 h each) for C-doped, resulting in over 4 times more total electricity demand than thermal etching (16.9 and 15.7 kWh versus 3.8 kWh, respectively).

3.3.3 Towards More Sustainable Syntheses: Approaches to Reduce Electricity Demand

Since electricity is identified as the major contributor to the g-C_3N_4 nanosheet syntheses impacts, opportunities to reduce electricity demand per gram of g-C_3N_4 nanosheets are pursued. Drying and stirring times are parameters during synthesis exploration that are chosen based on observation, past experience, and/or convenience (i.e., they are not comprehensively optimized). Identifying if drying and stirring steps are requisite and then optimizing (i.e., minimizing the total time) is a straightforward approach to reducing synthesis energy demand. For example, a 30% decrease in stirring and drying times (8.4 h vs. 12 h) for the C-doped synthesis reduces the total GWP impacts by 22% (10.8 vs. 8.42 kg CO_2 eq, respectively). Additionally, increasing the furnace heating rate and decreasing calcination heating time and temperature (for bulk g-C_3N_4 and the nanosheets synthesis processing) will reduce the furnace electricity consumption. Ranges of 2.3 °C/min to 15 °C/min,[89,108,119,178] 2 h to 4 h,[74,122,159] and 520 to 600 °C[36,73,159] have been reported for heating rate, heating time, and calcination temperature for bulk g-C_3N_4, respectively. The

associated impacts for the combinations of conditions range from 1.25 to 2.77 kg CO_2 eq, resulting in a difference of 1.52 kg CO_2 eq or 2.8% of the average per capita daily GHG emission in the US (20 metric tons CO_2 eq per person in the year 2019[179,180]). The variation in environmental impacts associated with electricity when modifying these calcination parameters are presented in **Table B.11** for all impact categories.

Given the intimate link between electricity and synthesis impacts, the U.S. electricity grid mix will also influence the combined resource footprint. As the electricity grid mix transitions to cleaner energy sources, the environmental impacts of synthesizing g-C_3N_4 nanosheets will decrease. Considering a large U.S. provider that offers a basic plan for a diverse electricity mix composed of biomass, geothermal, hydroelectric, solar, wind, natural gas, and nuclear, as an example,[181]there is a 77-78% reduction in GWP impacts for all syntheses when using this cleaner electricity mix compared to the current U.S. country mix (absolute values are presented in **Table B.12**, and % reduction for all impact categories in **Table B.13**).

When it comes to making decisions about g-C_3N_4 synthesis parameters for the suggested electricity modifications, any potential performance tradeoffs that arise from the influence on the final material properties must be considered. Insofar as there is no difference in material performance (or even an increase in performance) the decision is easy, choose the path that results in a lower resource footprint (e.g., less time of equipment use, faster heating rate, lower heating time, and lower calcination temperature). When modification of synthesis parameters influences material properties in a way that compromise performance, considering a more comprehensive system boundary (one that includes use-phase performance of the material in an application) and tradeoff analysis (e.g., performance for intended use, environmental impact, and economics) is required to inform decisions towards impact minimization.

Finally, further resolution of g-C_3N_4 synthesis mechanisms is needed to inform *a priori* design intended to direct how g-C_3N_4 materials are constructed for a desired outcome and use. For example, further insight into how different precursors affect the location and extent of non-metal doping, the role of temperature in atomic arrangement and morphology (e.g., g-C_3N_4 shape, dimensions), and the role of the solvent in supporting the polymerization process will all inform synthesis parameters that we identify herein as critically influencing the overall g-C_3N_4 resource footprint. Without this information, we are left to rely on a trial-and-error approach rather than an intentional, bottom-up approach to g-C_3N_4 synthesis. Given the number of parameters for each synthesis, the LCA results of this work identify parameters that have the greatest potential to reduce the impacts (i.e., which the results are most sensitive to) and thus, can aid in prioritizing resolution of the synthesis mechanism components.

3.3.4 Are g-C_3N_4 Nanosheets More Sustainable?: Benchmarking Synthesis Impacts to Nano-TiO_2

3.3.4.1 Mass-Based Environmental Impact Comparison of g-C_3N_4 Nanosheets and Nano-TiO_2 Syntheses

Determining whether a new material is sustainable requires meeting established targets (e.g., by industry, governing bodies, or regulations) or benchmarking impacts to existing alternatives. To evaluate the sustainability of g-C_3N_4 nanosheet syntheses, the environmental footprints of the eight syntheses considered in this study are compared to two nano-TiO_2 syntheses. Nano-TiO_2 is chosen because it is a well-established and commercially available photocatalyst. Further, a low (i.e., sol-gel) and a high (i.e., radio frequency thermal plasma) impact synthesis

were chosen to represent a range in nano-TiO_2 synthesis impacts based on an LCA by Wu *et al*.[87] Since the functional unit of the previous analysis[87] is 1 kg of nano-TiO_2 and the study herein is performed for a functional unit of 1 g of g-C_3N_4 nanosheets, the former unit processes were converted to reflect the production of 1 g of nano-TiO_2 for comparison. For this conversion, we assumed the worst-case scenario for impact generation by maintaining the electricity input (i.e., same amount to produce 1 kg and 1 g of nano-TiO_2) and any materials necessary for the equipment functioning (e.g., gases). Refinement of these parameters can be made in the future with additional information on the equipment capacity and time of use for synthesizing nano-TiO_2. Additionally, precursors and reagents were linearly scaled for producing 1 g of nano-TiO_2 (i.e., divided by 1000).

As an alternative to scaling down the nano-TiO_2 unit processes, we also scaled our unit processes to produce 1 kg of g-C_3N_4 nanosheets (details in Appendix B **section B.2.1)**. Since the size of the furnace for producing 1 g of g-C_3N_4 nanosheets does not have the capacity for 1 kg, we consider a higher capacity muffle furnace while keeping all other equipment the same (i.e., the power consumption is only modified for the calcination step). Precursors, reagents, and emissions are scaled linearly to produce 1 kg of g-C_3N_4 nanosheets (i.e., multiplied by 1000).

In the scale down scenario (i.e., nano-TiO_2 from kg to g; data in **Table B.14**), all eight g-C_3N_4 nanosheet syntheses generate higher GWP impacts (in kg CO_2 eq) than the nano-TiO_2 sol-gel method, and substantially lower GWP impacts than the radio frequency thermal plasma method (**Figure 4a** for GWP impact category; relative impacts for all categories are in **Figure B.3**). In the scale up scenario (i.e., g-C_3N_4 from g to kg; data in **Table B.15**), the GWP impacts for the radio frequency thermal plasma synthesis of nano-TiO_2 are lower than the C-doped g-C_3N_4. The sol-gel synthesis of nano-TiO_2 presents similar or higher impacts compared to chemical exfoliation, B-doped melamine, and B-doped urea syntheses of g-C_3N_4 (**Figure 4b** for GWP impact category;

relative impacts for all categories in **Figure B.4**). Additionally, the relative trend in g-C_3N_4 nanosheet syntheses impacts shifts in the scale down versus scale up approach. In the scale down approach, supramolecular and C-doped g-C_3N_4 nanosheet syntheses result in the highest impacts, and thermal etching results in the lowest impacts. In the scale up approach, C-doped remains the highest impact g-C_3N_4 synthesis, and B-doped urea has the lowest impact profile. The shift in outcomes and associated conclusions that can be drawn by taking a scale up versus scale down approach highlights the challenges in comparing between different LCA studies having different mass-based functional units as well as the critical influence of scaling unit processes, particularly when limited information of the synthesis details are available at scale. Since these two approaches arrive at different conclusions, combined they enable a more comprehensive comparison between g-C_3N_4 nanosheet and nano-TiO_2 syntheses.

A broader implication of these two scaling approaches for enabling comparison of g-C_3N_4 to nano-TiO_2 is that determining whether g-C_3N_4 is a more sustainable alternative is not straightforward. It depends on how g-C_3N_4 and nano-TiO_2 are synthesized and the underlying assumptions that enable equivalent functional unit comparison. Further, establishing standard benchmark material comparisons are essential to substantiating material sustainability claims.

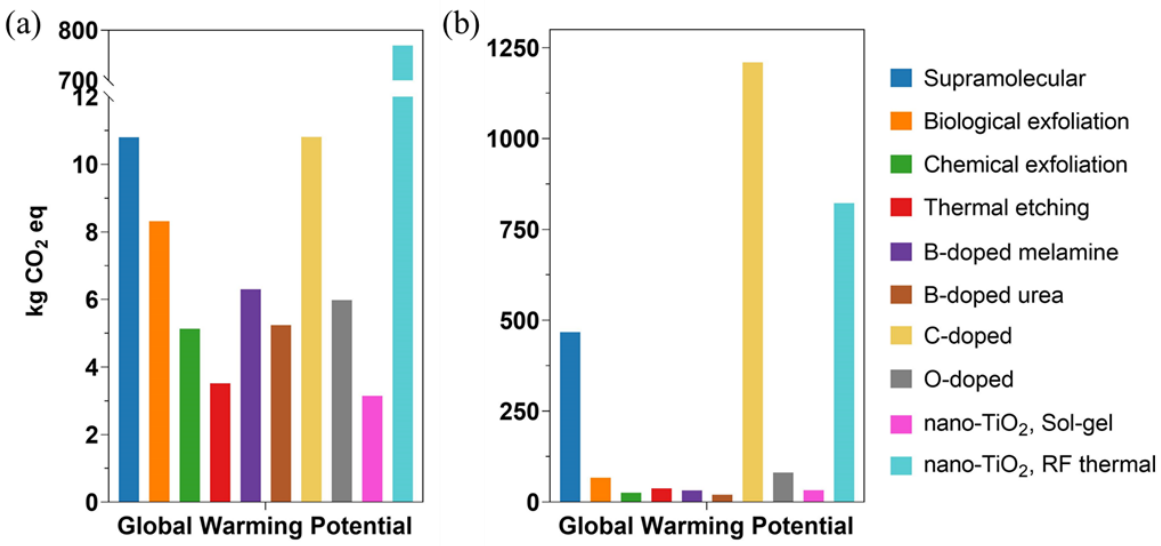

Figure 3.4. Global warming potential impacts (in kg CO_2 eq) for producing (a) 1 g and (b) 1 kg of g-C_3N_4 nanosheets and nano-TiO_2 by different synthesis routes. The impact values for nano-TiO_2 syntheses were obtained from the life cycle inventory reported by Wu *et al.*,[87] assuming the same electricity input and materials necessary for the equipment functioning when scaling down the functional unit from kg to g. The g-C_3N_4 nanosheet syntheses were scaled up from g to kg assuming a higher capacity muffle furnace while all other equipment remained the same. Precursors, reagents, and emissions were scaled linearly (i.e., divided by 1000 for scaling down or multiplied by 1000 for scaling up). RF thermal = radio frequency thermal plasma

3.3.4.2 Comparing Environmental Impacts of Precursors

A predominant positive characteristic of g-C_3N_4 compared with alternative photocatalysts is its synthesis from non-metal precursors. The underlying assumption is that metal mining and refining carries large environmental impacts. For this reason, we compare the environmental impact of producing 1 kg of commonly used g-C_3N_4 precursors (i.e., melamine, urea, and cyanamide) to the precursors of the two selected nano-TiO_2 syntheses (i.e., titanium isopropoxide (TTIP) for sol-gel, and titanium tetrabutoxide (TTBO) for radio frequency thermal plasma)

(relative impacts, normalized to the highest value in each category, are presented in **Figure 5**, and absolute values are in **Table B.16**). Urea generates substantially lower impacts than the titanium precursors in all impact categories. Compared to the nano-TiO_2 syntheses precursors, melamine generates <20% difference in impacts in the AC, HHNC, RE categories, and its impacts are >20% lower in the OD, GWP, PS, EU, HHC, EC, FF categories. Cyanamide consistently induces the greatest impacts of all precursors across the categories, which is attributed to the calcium cyanamide precursor and methanol used in its synthesis (details of process contributions are presented in **Figure B.5**). Urea, a precursor to calcium cyanamide, is the predominant contributor to its impacts. The high impacts of urea derive from the energy demand and emissions associated with its precursor, ammonia, produced by the Haber-Bosch process. Finally, the difference in cyanamide's relative impact could, in part, be due to the fact that the authors established this process based on Reference [182] (LCI details in **Table B.17**), while the other precursors are established in the available databases.

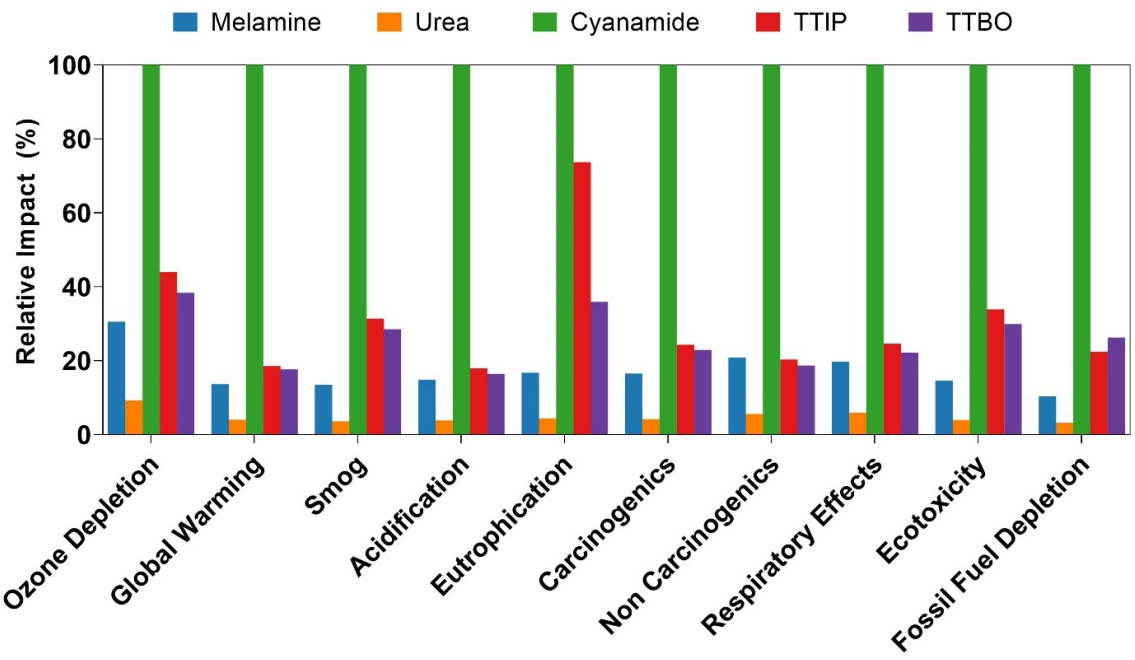

Figure 3.5. Relative environmental impacts for producing 1 kg of melamine, urea, and cyanamide, precursors for g-C_3N_4, and 1 kg of titanium isopropoxide (TTIP), and titanium tetrabutoxide (TTBO), precursors for nano-TiO_2 by sol-gel and radio frequency thermal plasma, respectively. Relative impacts are normalized to the highest value in each category.

3.3.4.3 Use-Stage Considerations

In addition to the environmental impacts from the production phase of the g-C_3N_4 nanosheets, the material intrinsic characteristics (e.g., band gap determining the maximum wavelength of light absorption) offer opportunities for sustainability benefits in the use-stage. Since g-C_3N_4 can harvest visible-light, there is less energy demand for its activation compared to nano-TiO_2, which requires higher energy, UV wavelengths. As such, determining the energy demand savings associated with using visible light versus UV light sources are relevant in evaluating the prospect of g-C_3N_4 as a sustainable photocatalyst alternative. Moreover, as g-C_3N_4

photocatalytic performance (e.g., antimicrobial efficacy) can be tuned by chemical composition modifications during synthesis, a performance tradeoff analysis is included herein to evaluate the feasibility of g-C_3N_4 to meet the established UV disinfection performance.

3.3.4.3.1 Quantifying Energy Demand Savings Associated with Using Visible Light Versus UV Light Sources

So far, we describe the environmental impact footprint of synthesizing g-C_3N_4 nanosheets and potential avenues towards impact reduction. A primary advantage of g-C_3N_4 is the ability to harness visible light for activation, rather than high energy UV light, which is realized during the material use. The visible light source can be from sunlight or artificial lighting. Given recent advances in energy-efficient technology light emitting diodes (LEDs),[183,184] we compare the energy demand of g-C_3N_4 activated by various visible wavelengths to UV wavelengths necessary to activate nano-TiO_2. Since the g-C_3N_4 maximum activation wavelength varies with its chemistry and morphology (i.e., how it is synthesized),[153] there is a range of accessible visible wavelengths. Here, we analyze the energy demand of 415 and 470 nm visible LEDs compared with 385 and 365 nm UV LEDs,[185] (based on reported maximum absorption wavelengths[153,186,187]) and assume the photocatalysts are activated for the same amount of time (i.e., run the light source for one hour). Thus, this exercise simply compares the energy demand of LED light sources necessary for these different photocatalytic materials.

Activating g-C_3N_4 with visible wavelength LEDs requires 29% lower average energy demand (in kWh) than the UV wavelengths for nano-TiO_2 (4,790 compared to 6,715 kWh) (**Figure 6**). There is potential to further reduce the energy demand to 52% if 470 nm wavelength is successful in activating g-C_3N_4 compared to 365 nm for nano-TiO_2. Considering a light source

that includes all the visible range of the light spectrum (i.e., 400 – 700 nm) is also relevant since modifications to the g-C_3N_4 chemical composition result in optical band gap variations (i.e., change in the maximum wavelength of absorption for the photocatalytic process to occur) and because there are numerous light sources that contain the full visible spectrum. As such, a white LED (visible wavelength range 400 – 700 nm) is considered, and results in 36% lower energy demand compared to the average for UV LEDs (4,290 versus 6,715 kWh).

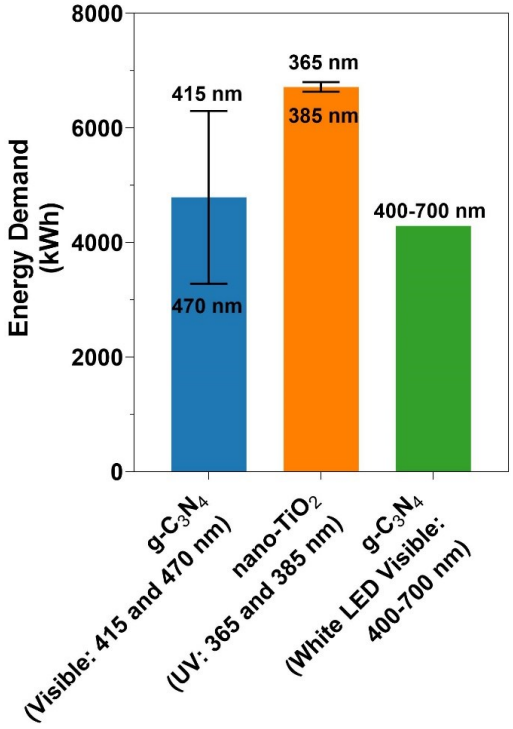

Figure 3.6. Energy demand (in kWh) required to irradiate the photocatalysts with light emitting diodes (LED) with visible light and ultraviolet (UV) wavelengths. Note that the y-axis values are determined for one hour irradiation.

These use-stage potential energy gains highlight the positive impact (i.e., impact reduction) that visible light activation offers over UV-activated photocatalysts. The actual influence of these energy gains on the total environmental impacts of g-C_3N_4 considering the expanded system

boundary – raw materials, synthesis, and use phases – will depend on the working setup for a given application (e.g., the infrastructure and irradiation time to achieve the same performance).

3.3.4.3.1 Identifying Performance Break-Even Points: UV Light Disinfection Comparison

Determining the mass of g-C_3N_4 nanosheets with equivalent embodied environmental impact to a conventional alternative (UV light) for achieving a desired level of water disinfection (that is, the break-even point) guides future efforts of synthesizing g-C_3N_4 as an attractive sustainable disinfection alternative. The environmental impact of using the US EPA regulated[188] UV dose of 186 mJ/cm^2 to achieve 4-log virus inactivation in drinking water was calculated considering one UV lamp and 83 Wh of electricity per m^3 of treated water (**Table B.18**).[189] The break-even point (i.e., equivalent g-C_3N_4 nanosheets mass) is investigated for both the highest and lowest impact g-C_3N_4 nanosheet syntheses (supramolecular and thermal etching). The GWP electricity impacts of these syntheses alone surpass that of the UV disinfection scenario considered here, suggesting that any mass of g-C_3N_4 used for viral disinfection would result in greater impacts than that of UV disinfection. There are a few midpoint impact categories in which this is not the case (collectively: HHC, HHNC, RE, and EC) (see **Tables B.18 and B.19**) suggesting the potential for further tradeoff analysis could be advantageous depending on the specific context and priority categories.

Given electricity is the major contributor to the environmental impacts of g-C_3N_4 synthesis, and the associated energy impacts have the potential to be reduced via further resolution of synthesis mechanisms and with increased scale (*vide supra*), we assessed an alternative approach to achieving a break-even point. We considered the necessary reduction in electricity input for synthesizing 1 g of g-C_3N_4 nanosheets to be equivalent to impacts of UV disinfection. For the GWP impact category, the break-even point is achieved with a 94% energy reduction for the

highest impact, supramolecular synthesis (i.e., a total electricity demand of 0.93 kWh). For the lowest impact route, thermal etching, removing all synthesis associated electricity will not offset the GWP impacts of UV disinfection (Note: the same is true for AC, EU, and FF categories) (see **Tables B.18 and B.20**).

While both approaches to identifying break-even points return unfavorable results to support the use of g-C_3N_4 as a sustainable alternative for viral disinfection of drinking water, further investigation of its performance, under actual disinfection use conditions, will further illuminate its potential feasibility. Further, comparing to other performance metrics (e.g., bacterial disinfection, non-disinfection performance metrics) could illuminate very different outcomes, in favor of g-C_3N_4. In this way, further research is needed to uncover optimal system conditions, photocatalyst loading, and reuse cycles to fully realize the potential for g-C_3N_4 to result in a net benefit (i.e., net negative embodied environmental impacts of synthesis) compared with performance of identified alternatives.

3.4 Supporting Sustainable Development of g-C_3N_4

This cradle-to-gate LCA is the first to evaluate the environmental impacts of g-C_3N_4 nanosheet synthesis. Eight established synthesis routes to produce g-C_3N_4 nanosheet are considered, and electricity is identified as the major contributor to the cumulative impacts. There are opportunities for reducing the environmental footprint of these synthesis routes by decreasing energy demand through synthesis modifications (i.e., removing or reducing high energy demand equipment use time), optimizing the calcination step (i.e., faster heating rate, lower heating time, lower temperature), and with shifts to lower-impact electricity sources. Determining the sustainability of g-C_3N_4 as a photocatalyst requires benchmarking with a competitive alternative.

Comparing the environmental impacts of g-C_3N_4 nanosheets to nano-TiO_2 reveals mixed comparative results depending on the synthesis method and the assumptions underlying the equivalent functional unit comparison. Nevertheless, 52% energy demand reduction (in kWh) can be reached in the use-phase when activating g-C_3N_4 with visible wavelength LEDs instead of UV wavelengths for nano-TiO_2. Finally, g-C_3N_4 performance for water disinfection was compared to conventional UV disinfection method. Results of this analysis reveal the inability of g-C_3N_4 nanosheet to meet drinking water disinfection standards for viral load reduction (4-log reduction) with a lower impact footprint for any mass of g-C_3N_4. These results are the first to benchmark performance and further development of this tradeoff analysis (e.g., with additional use-phase information, different syntheses, within different contexts and priority impact categories) could return advantageous results.

As research on g-C_3N_4 evolves and more information becomes available, improved resolution of synthesis inventory data and more comprehensive use-phase considerations can be incorporated into the sustainability assessment. An important consideration as research develops is the reporting of synthesis parameters and detailed conditions of use-phase performance assessment, which will enable comparison across studies and reduce assumptions required in establishing the inventory and conducting impact assessment. Measured performance across universal metrics will inform a functional unit that incorporates the target function (e.g., antimicrobial efficacy). Incorporation of performance considerations has been shown to shift the rank order preference among synthesis methods compared to a mass-based analysis.[87,88] Synthesis parameter limitations identified in the present work include assuming theoretical synthesis yield values due to the lack of experimental yields reported in the g-C_3N_4 synthesis references. Given yield has been previously shown to drive environmental impacts,[88] reporting this synthesis

parameter is critical. Other critical synthesis details include the step-by-step procedure, equipment used and their operation time, temperature and stirring/centrifugation speed when applicable, precursors and reagents use (mass, volume, and concentration), and flow or mass of gases used. Combined with the findings of this LCA, these future considerations enable movement towards more sustainable development of g-C_3N_4 nanosheets.

4.0 Major Findings and Research Recommendations

4.1 Major Findings

This research was motivated by the need for development of sustainable and effective antimicrobial agents. A literature review on g-C_3N_4 as an antimicrobial revealed knowledge gaps regarding: (i) the effect of modifying g-C_3N_4 chemical composition by C-doping on photocatalytic antibacterial efficacy, and (ii) the assessment of g-C_3N_4 sustainability. g-C_3N_4 is studied herein with the overall objective of guiding the development of an effective and sustainable antimicrobial agent based on rational design.

The ability to control physicochemical properties of g-C_3N_4 through manipulating its chemical composition opens new avenues for the future of antimicrobial agents. Successfully accomplishing this goal requires connecting synthesis parameters to antimicrobial activity to inform rational design. A literature review on tailoring g-C_3N_4 chemical composition highlighted C-doping as an efficient metal-free approach to enhancing photocatalytic performance for applications in chemical degradation and hydrogen production (**Table 1.1**). My research, detailed in Chapter 2, is the first to investigate C-doping as an avenue to control g-C_3N_4 antibacterial activity. A sample set of systematically modified C-doped g-C_3N_4 was prepared with different carbon:nitrogen ratios to demonstrate how modifications in chemical composition change g-C_3N_4 physicochemical properties, including band gap, intermediate defect states, dispersed surface area, absorbance in suspension, and charge separation efficiency. The effect of these changing properties on RS production and, consequently, the antibacterial activity (represented by *E. coli*

inactivation) was pursued to inform design guidelines. C-doping is shown as an effective approach to tuning g-C_3N_4 properties and results in a range of bacterial inactivation from zero to five log reduction. C-doping is effective at extending the range of visible-light absorption from 449 nm to 588 nm while inducing various levels of bacterial inactivation, suggesting this approach has potential to leverage low-energy, economically favorable light sources (e.g., visible versus UV). Contrary to the previously reported effect of C-doping in chemical degradation and hydrogen production (where increased C:N ratio boosted photocatalytic performance),[60,72-74,82,118] increased C-doping was found to decrease *E. coli* inactivation efficiency. Further, the results suggest that the approach to modifying chemical composition (C-doping versus changing the pyrolysis temperature) influences the photocatalytic performance via the type of defects introduced (e.g., N vacancies versus N replacement with C). Finally, the efficacy of g-C_3N_4 visible-light photocatalytic inactivation towards environmentally and clinically relevant antibiotic-resistant pathogens, methicillin-resistant *Staphylococcus aureus* (MRSA) and vancomycin-resistant *Enterococcus faecalis* (VRE) is demonstrated.

g-C_3N_4 has been reported as a sustainable photocatalyst, but this claim has yet to be concretely supported. Chapter 3 presents the first study to assess the sustainability of g-C_3N_4 synthesis using life cycle assessment and benchmarking impacts to the well-established photocatalyst nano-TiO_2. This study provides life cycle inventory data for synthesizing bulk g-C_3N_4 and g-C_3N_4 nanosheets by eight different synthesis routes. Energy demand during synthesis is identified as the major process contributing to the impacts for all syntheses in ten mid-point impact categories representative of environmental and human health impacts. Opportunities to reduce the environmental footprint of the syntheses are determined and include decreasing energy demand by removing or reducing the use time of high energy demand equipment use, increasing

heating rate and decreasing heating time at the calcination step, and with shifts to lower-impact electricity sources. Impact comparison between g-C_3N_4 and nano-TiO_2 syntheses reveals that the sustainability claim determination depends on the synthesis method considered for benchmarking and the assumptions associated with the equivalent functional unit comparison. Thus, claiming g-C_3N_4 as a sustainable photocatalyst may be considered an empty statement without a defined standard for comparison. Considering the use-phase, g-C_3N_4 activated with visible wavelength LEDs requires approximately half (52% less) the energy demand compared with UV wavelengths for nano-TiO_2. Yet, these benefits do not translate to the use phase when the equivalent mass of g-C_3N_4 required for a disinfection endpoint is considered. The embodied energy of any mass of g-C_3N_4 (i.e. > 0) is greater than the energy of UV light required to meet water disinfection standards for viral inactivation when considering six of the ten midpoint impact categories, including global warming potential.

Taken together, the research presented in this dissertation offers important insights into developing g-C_3N_4 as an effective and sustainable nanomaterial for antibacterial applications.

4.2 Research Recommendations

The work presented in Chapter 2 of this dissertation probes the potential of using C-doping as a way to modulate the chemical structure of g-C_3N_4 and thus, the properties governing photocatalytic antibacterial activity. The research demonstrated in Chapter 3 guides the synthesis of g-C_3N_4 nanosheets towards sustainability. Future research directions anticipated to have a

positive impact on the design of g-C_3N_4 as a sustainable and highly effective antimicrobial agent are presented below.

4.2.1 Optimizing the Photocatalytic Process Setup (Light Source, g-C_3N_4 Concentration and Reaction Time) for drinking water applications with reduced environmental impacts

As presented in chapter 2, C-doping below 20% was shown to induce bacterial inactivation while extending the range of visible-light absorption. This finding highlights C-doping as a possible synthesis route for leveraging lower-energy, economically favorable light sources, such as visible LEDs. Since our experiments simulated a solar light source, including the visible range only, further investigation is necessary to confirm the efficiency of these alternative light sources. Additionally, optimizing the g-C_3N_4 concentration and reaction time to achieve desired antibacterial performance would inform the feasibility of application in real water treatment scenarios.

4.2.2 Uncovering How Higher Total RS Produced by g-C_3N_4 Synthesized with Different Pyrolysis Temperatures Result in Lower Bacterial Inactivation

It has been demonstrated in Chapter 2 that enhancing the carbon:nitrogen ratio by increasing pyrolysis temperature from 550 to 600°C resulted in unexpected antibacterial activity when coupled with results of total RS produced (i.e., higher RS production did not translate to higher antibacterial activity). Further investigation is necessary to uncover the causes of this unexpected finding. Results of higher RS production with lower bacterial inactivation could be related to the type of RS produced, which has been shown to play different roles in bacterial

inactivation. Additional chemical composition manipulation approaches (e.g., larger sample set of g-C_3N_4 synthesized by varying pyrolysis temperatures) and further characterization techniques (e.g., to quantify the relative amount of specific types of RS produced by distinct g-C_3N_4 samples) are needed to determine the underlying cause of increased RS production independent from bacterial inactivation efficacy.

4.2.3 Expanding g-C_3N_4 Efficacy Evaluation to Relevant Water Pathogens

g-C_3N_4 photocatalytic activity was successfully demonstrated in Chapter 2 to be effective at inactivating clinically and environmentally relevant antibiotic-resistant pathogens, methicillin-resistant *Staphylococcus aureus* (MRSA) and vancomycin-resistant *Enterococcus faecalis* (VRE), and the results highlight that susceptibility to inactivation depends on the microorganism. While g-C_3N_4-based photocatalysts have been found to inactivate a wide range of microorganisms (i.e., *Escherichia coli*, *Staphylococcus aureus*, *Enterococcus faecalis, Salmonella*, *Pseudomonas aeruginosa, Bacillus subtilis, Bacillus anthracis* endospore*s*, ampicillin-resistant *Escherichia coli*, ampicillin-resistant *Staphylococcus epidermidis,* multidrug-resistant *Bacillus subtilis, Staphylococcus aureus* biofilms, Human adenovirus type 2*, MS2* bacteriophage*, Microcystis aeruginosa* algae, and *Candida albicans* yeast),[41,67,68,146] evaluating its antimicrobial efficacy to additional relevant water pathogens, such as *Legionella pneumophila*, *Giardia, and Cryptosporidium*,[190] would further steer the potential use of g-C_3N_4 in water treatment applications.

4.2.4 Rational Design of g-C_3N_4 for Improved Viricidal Performance

Photocatalysis has been identified to promote microbial inactivation by producing RS, which can react with and damage components of viruses and bacteria.[191,192] Microorganisms respond differently to the photocatalytic process depending on their physiology, chemical composition, and metabolism,[28,66,193,194] which widely vary across viruses and bacteria as well as types within each class. Viruses are anticipated to be more resistant to photocatalysis compared to bacteria,[195,196] owing to bacteria's fragile cell membranes and key metabolic systems (e.g., respiration), which can be easily compromised by failure in the defense mechanism against environmental stress. Further, viruses possess a more robust external structure (i.e., rigid capsid).[28] RS has been shown to inactivate bacteria by cell envelope rupture and cytoplasmic components leakage,[26] and initiates virus decomposition due to viral shapes distortion and surface protein (mainly replicase and maturation proteins) damage.[15] As g-C_3N_4-based photocatalysis has been proposed to be distinct between viruses and bacteria,[28,41,197] it is hypothesized that mechanisms of g-C_3N_4 photocatalytic antimicrobial activity will not directly translate from bacterial to viral inactivation.

Photocatalytic viral inactivation by visible-light-driven g-C_3N_4 was first studied in 2016,[15] and this application is still under-explored, with only three studies investigating g-C_3N_4-based photocatalysts for inactivating the bacteriophage MS2,[15,28,198] one targeting human adenovirus type 2,[199] and one having the bacteriophage f2 as the model virus.[200] The ability to tune g-C_3N_4 for improved viricidal performance based on material synthesis modification by C-doping or modifying pyrolysis temperature has not been explored to date. It is anticipated that g-C_3N_4 with modified chemical composition will promote distinct viricidal activity by facilitating the

generation of different types and amounts of RS, and that the performance trends for a set of g-C_3N_4 samples with different carbon:nitrogen ratios will be unique from those identified in Chapter 2. It is important to identify the governing RS for viral inactivation using a systematically modified and comprehensively characterized g-C_3N_4 sample set and establish the correlation between RS role, viral disinfection, and material properties.

4.2.5 Expand the g-C_3N_4 Sustainability Assessment by Incorporating a Performance-Based Functional Unit to the LCA

In Chapter 3, the environmental impacts of predominant g-C_3N_4 synthesis routes are evaluated for the first time using the LCA approach. Given the focus of the presented work being on the synthesis of this developing nanomaterial that has a wide range of applications, a mass-based functional unit was chosen to not limit the results and conclusions to a specific use, as in the case of selecting a performance-based functional unit.

g-C_3N_4 photocatalytic activity depends on optical, electronic, and chemical properties of the material, which can be tuned by synthesis.[16,46,47] Future LCA studies of g-C_3N_4 incorporating a performance-based functional unit (e.g., antimicrobial efficacy, chemical degradation, H_2 production) are relevant because the impacts of g-C_3N_4 synthesis may not be accurately estimated when considering g-C_3N_4 mass alone, since a baseline endpoint may require different masses of g-C_3N_4 synthesized by different methods. Moreover, incorporation of performance considerations have been shown to shift the rank order preference among synthesis methods compared to a mass-based analysis.[87,88] This recommended research further assesses and directs the sustainability of g-C_3N_4.

Appendix A Supporting Information for Chapter 2

A.1 Materials and Chemicals

Melamine (99%, ACROS Organics AC125350050), sodium chloride (NaCl, 99.6%), Bacto agar, lysogeny broth Lennox (LB), sodium oxalate (99.7%), and tempol (Tocris Bioscience) were obtained from Fisher Scientific (Pittsburgh, PA, USA). Cyanuric acid (98%, 185809), barbituric acid (99%), and methylene blue (MB) were purchased from Sigma-Aldrich (St. Louis, MO, USA). Carboxy-H_2DFFDA, and phosphate buffered saline (PBS, pH 7.4) were acquired from ThermoFisher Scientific (Waltham, MA, USA). Ethanol (190 Proof) was obtained from Decon Labs (King of Prussia, PA, USA). Deionized (DI) water was produced by Millipore Synergy UV Water Purification System and used as solvent for all chemicals, unless otherwise specified.

A.2 Characterization of g-C_3N_4 Samples

A.2.1 X-Ray Diffraction (XRD). XRD patterns were collected on a Bruker D8 Discover instrument using Cu K_α radiation at a generator voltage of 40 kV and a generator current of 40 mA. The scan speed was 0.40 second/step, the step size was 0.02°, and the angle range was 10-60°.

A.2.2 Transmission Electron Microscopy (TEM). Electron microscopy imaging was obtained using a JEOL JEM-2100F transmission electron microscope operated at 200 kV. The TEM specimen was prepared by applying 10-20 μL suspensions of the g-C_3N_4 sample (100 μg mL^{-1}) in ethanol onto holey carbon films supported on Cu TEM grids.

A.2.3 X-ray Photoelectron Spectroscopy (XPS). Surface elemental composition of the g-C_3N_4 samples were evaluated by XPS. A Thermo Scientific ESCALAB 250Xi instrument (monochromatic Al Kα X-ray source, 1486.7 eV, spot size 650 μm) was employed to analyze the samples that were prepared by placing approximately 2 mg of powder g-C_3N_4 onto the sample holder covered with double-sided copper tape. A pass energy of 150 eV with a step size of 1.0 eV was used to obtain the survey spectra, and a pass energy of 50 eV with a step size of 0.1 eV was used to collect high-resolution C1s and N1s spectra. For each sample, at least three measurements in different locations were carried out. The software Thermo Scientific Avantage was used to process the spectra in order to calculate the atomic percentage of elements, and to determine the distribution of N species by peak deconvolution. For component-fitting of the N1s region, each spectrum was subtracted with a modified Shirley background and the C1s peak at 284.8 eV was used for energy scale correction. Poly(3,5 pyridine) was used as the reference standard to obtain the peak fitting constraint for the binding energy of C–N=C (398.7 eV). The peak fitting constraint for the binding energy of N–(C_3) used the value reported in the literature (~400.4 eV).[60,134,135] π-π* excitation (centered at ~404 eV) was assigned to the remaining tail region toward high binding energy. Peak positions were constrained to shift within ±0.3 eV from the assigned binding energies, and values of full width at half maximum (FWHM) for all three components were kept at the same level between components with ±0.2 eV deviation and at least as large as the value measured for Poly(3,5 pyridine).

A.2.4 Surface Area in Suspension Measured by MB Adsorption. MB dye adsorption is a standard method for measuring surface area of graphitic materials in suspension.[201,202] The method used herein was adopted from our previous study.[203] The g-C_3N_4 samples were dispersed in saline solution by 1 h bath sonication and then mixed with a MB solution in a 1:1 volume ratio (final

concentrations of 50 mg L^{-1} and 25 mg L^{-1}, respectively). Three replicates of each g-C_3N_4 material mixed with MB were continuously shaken for 24 h in a rotator at room temperature to achieve the adsorption equilibrium. At time 24 h, the free MB was isolated from the solution by two centrifugation cycles of 13,226 × g for 5 minutes, with transferring the supernatant to a clean tube in between cycles, and its concentration determined by measuring its light absorbance at 663 nm wavelength on a UV-Vis spectrophotometer (Thermo Scientific Evolution 201). Finally, the mass loss of MB (i.e., MB adsorbed to the material) was determined by:

$$MB\ mass\ loss = MB_{24h\ control} - MB_{24h\ CN} \quad (A.1)$$

Where $MB_{24h\ control}$ is the mass of MB (MB concentration times reaction volume) after 24 h without g-C_3N_4, and $MB_{24h\ CN}$ is the mass of MB after 24 h reaction with g-C_3N_4. This step rules out MB oxidation as a confounding factor for MB adsorption.

Since no literature value was found relating area of g-C_3N_4 surface covered per mg of MB adsorbed, the dispersed surface area of the samples is indirectly represented by the mass of MB adsorbed divided by the mass of the g-C_3N_4 (g/g). The experiment was repeated twice in different occasions.

A.2.5 Absorbance of g-C_3N_4 in Solution. UV-vis spectra of g-C_3N_4 suspensions (19 mg L^{-1}) were obtained on an Evolution 201 Thermo Scientific Spectrophotometer in the wavelength region of 290 to 700 nm. g-C_3N_4 suspensions were dispersed in PBS (1 mM, pH 7.4) using a bath sonicator (VWR Aquasonic 150T) for 1 h and a polymethyl methacrylate (PMMA) cuvette was used for all measurements (4.5 mL, Fisher Scientific, 285 to 750 nm).

A.2.6 Band Gap and Urbach Energy Determination. UV-Vis diffuse reflectance measurements were performed using the LAMBA-750 UV-Vis-NIR spectrophotometer (Perkin Elmer L750) equipped with a 60 mm integrating sphere. Measurements were collected over the

wavelength range of 200 to 800 nm. The angle of incidence of the light beam on the sample was set to 0 degrees in order to exclude the specular reflectance contribution to the intended measurement of diffuse reflectance only. The reflectance data (*R*) obtained express the relative reflectance of the sample compared to a barium sulfate ($BaSO_4$) standard. The spectra in percent reflectance were converted using the Kubelka-Munk function *F(R)*. For the measurements, g-C_3N_4 or $BaSO_4$ powder was loaded to a powder holder (Perkin Elmer 52123164) until the quartz window was completely covered. Indirect optical band gap values were obtained from the Tauc plot approach, as well documented in the literature.[39,136,137] Urbach energy was determined from the reciprocal of the slope of the linear fitting of ln(*F(R)*) vs. *hv,* where *h* is Planck's constant (4.136×10^{-15} eV s), and *v* is the frequency of photons – speed of light (2.998×10^{8} m s^{-1}) divided by λ (nm), the photon's wavelength.[116]

A.2.7 Steady-state Photoluminescence (ss-PL). The ss- PL of g-C_3N_4 in solution were obtained by using FluoroMax-3 (Jobin Yvon Horiba). g-C_3N_4 powder was dispersed in PBS (1 mM, pH 7.4) at a concentration of 19 mg L^{-1}, and bath sonicated (VWR Aquasonic 150T) for 1 h. For ss-PL measurements, the emission spectra ranging from 345 to 640 nm wavelength was obtained at an excitation wavelength of 330 nm in a UV cuvette (4.5 mL, Fisher Scientific) under constant magnetic stirring. Since ss-PL depends on light absorbance of the photocatalysts, absorbance of g-C_3N_4 in solution was measured from the same aliquots used for ss-PL.

A.2.8 Zeta Potential. Zeta potential of prepared g-C_3N_4 aqueous suspension (19 mg L^{-1}, dispersed in saline solution by 1 h bath sonication) was determined using Omega cuvettes (Anton Paar) on a Litesizer 500 Particle Analyzer instrument (Anton Paar). The temperature was maintained at 25 °C.

A.3 Photocatalytic Experiments

A.3.1 Light Sources and Irradiance Measurements

Photocatalysis experiments (RS production, MB degradation, and *E. coli* inactivation) were carried out by irradiating the samples with a 300 W Xenon light source (Sciencetech SLB300B; spectral irradiance in **Figure A.1**) equipped with a bandpass filter (Sciencetech HPF-BP-VIS-FT-3) that blocks the UV and near infrared (NIR) radiation while transmitting visible light (400 nm < λ < 700 nm) with 25 cm working distance. The spectral irradiance measurements were performed by Sciencetech using a BLACK-Comet-SR spectrometer (Steller Net).

For the experiments with MRSA and VRE, the light source used was a 300 W Xenon arc lamp (Newport 6259) in an arc lamp housing (Newport 66921) with a full reflective beam turner (Newport 66245) and equipped with a bandpass filter (Omega Optical 775HSP; spectral irradiance in **Figure A.2**). The full-spectrum lamp irradiance was measured using a UV-Vis fiber optic spectrometer (Avantes AvaSpec-2048) adapted with a cosine corrector at the same working distance used in the photocatalytic experiments.

A.3.2 Photon Flux and Photon Fluence Determination

In order to compare efficacy across different systems (e.g., reactor designs, photocatalysts) and inform future economic feasibility assessment, the photocatalytic activity (RS production, MB degradation, and bacterial inactivation) of g-C_3N_4 materials was reported as a function of photon fluence (photon cm^{-2}). This parameter means that when one cm^2 of the photocatalyst surface is irradiated, it receives a certain number of photons. In our calculations, 100% of the absorbable

incident photons were assumed to generate an electron-hole pair. Additionally, only photons with energy equal or greater than the band gap were used for calculating photon fluence for each g-C_3N_4 sample. Reporting photocatalytic activity in relation to photon fluence is critical when using polychromatic light sources and enables accounting for different intensities across the light source spectrum. The photon fluence of each sample was calculated based on a previous study[204] and detailed below.

i) Estimate band gap (E_g, in eV) for each photocatalyst from the Tauc plot (**Figure 2.1**).

ii) Calculate the maximum wavelength of absorption (λ_{Max}, in nm) for each photocatalyst:

$$\lambda_{\mathrm{Max}}\ (\mathrm{nm}) = \frac{hc}{E_g} = \frac{1239.8\ (\mathrm{eV{\cdot}nm})}{E_g\ (\mathrm{eV})} \qquad (A.2)$$

h = Planck's constant = 4.136×10^{-15} eV s^{-1}.

c = speed of light = 2.998×10^{8} m s^{-1}.

Values of E_g and λ_{Max} for all photocatalysts are displayed on **Table 2.2**.

iii) Calculate the energy of a photon (E_p, in J) for wavelengths ranging from 400 nm to 700 nm:

iv)

$$E_p\ (\mathrm{J}) = \frac{hc\ (\mathrm{J{\cdot}nm})}{\lambda\ (\mathrm{nm})} \qquad (A.3)$$

h = Planck's constant = 6.626×10^{-34} m^2 kg s^{-1}.

v) Determine the energy flux distribution (F_e, in W m^{-2}) by multiplying the average of the spectral irradiance (specific to a light source) measured at one step intervals of wavelength (e.g., 400.1, 400.2, etc. from 400 nm to 700 nm):

$$F_e\ (\mathrm{W\cdot m^{-2}}) = \left(\frac{y_1+y_2}{2}\right) \times (\lambda_1 - \lambda_2) \qquad (A.4)$$

where y_1 and y_2 are the spectral irradiance (W m^{-2} nm^{-1}) measured at wavelengths λ_1 and λ_2 (nm), respectively.

vi) Calculate the absorption correction ($AbsC$) by normalizing the absorbance spectra *F(R)* obtained from UV-Vis DRS to the maximum absorbance value (Abs_{Max}) in the range of 400 to 700 nm:

$$AbsC = \left(\frac{Abs}{Abs_{Max}}\right) \quad \text{(A.5)}$$

$AbsC$ = absorbance correction at a certain wavelength.

Abs = absorbance (a.u) at a certain wavelength.

Abs_{Max} = maximum absorbance value (a.u.) in the wavelength range of 400 to 700 nm.

vii) Considering that the photocatalysts have different absorbance profiles (see $AbsC$ spectra in **Figure A.3**), correct the energy flux distribution by multiplying F_e (W m^{-2}) by the absorption correction.

$$F_{eC}\ (\mathrm{W \cdot m^{-2}}) = F_e \times AbsC \quad \text{(A.6)}$$

F_{eC} = energy flux corrected by absorbance.

viii) Determine photon flux distribution (F_p, in photon s^{-1} m^{-2}) by converting the energy into photons associated with each wavelength:

$$F_p\ (\mathrm{photon \cdot s^{-1} \cdot m^{-2}}) = \frac{F_{eC}\ (\mathrm{W \cdot m^{-2}})}{E_p\ (\mathrm{J})} \quad \text{(A.7)}$$

ix) Determine the total photon flux (F_{pf}, in photon s^{-1} m^{-2}) available to the photocatalyst by adding the photon flux associated with each wavelength across the range of absorbable wavelengths:

$$F_{pf}(\mathrm{photon \cdot s^{-1} \cdot m^{-2}}) = \int_{400}^{MWA} y d\lambda \quad \text{(A.8),}$$

where *y= f(λ)* is the photon flux at the specified wavelength (photon s^{-1} m^{-2}).

x) Convert F_{pf} to photon s^{-1} cm^{-2}.

Summary of photon flux results:

Sample	F_{pf} (photon s^{-1} cm^{-2})
CN-550	6.2313E+14
5% C-CN	1.3399E+15
15% C-CN	3.1244E+15
20% C-CN	4.5692E+15
50% C-CN	5.9917E+15
CN-600	1.7158E+15

Then, photon fluence (photon cm^{-2}) can be determined by multiplying F_{pf} (photon s^{-1} cm^{-2}) by the time of exposure of the sample (s).

In this study, even though the maximum wavelength of absorption for 20% C-CN and 50% C-CN are higher than 700 nm, their maximum wavelength of absorption was set to 700 nm for the photon fluence calculations because of the bandpass filter used in the experiments.

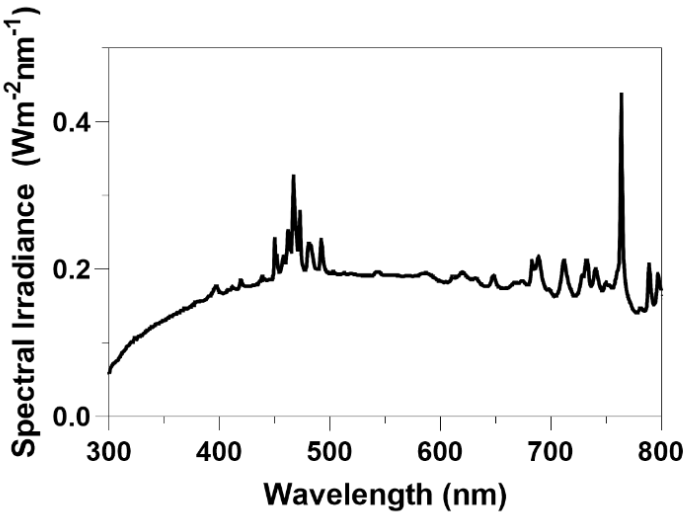

Figure A.1. Spectral irradiance of 300 W Xenon lamp (Sciencetech SLB300B). Additionally, a bandpass filter was added to allow only visible light to pass ($400 < \lambda < 700$ nm). Data provided by Sciencetech Inc., and obtained using Black Comet Spectrometer (StellarNet). This light source was used for photocatalytic activity experiments of RS production, *E. coli* inactivation and MB degradation.

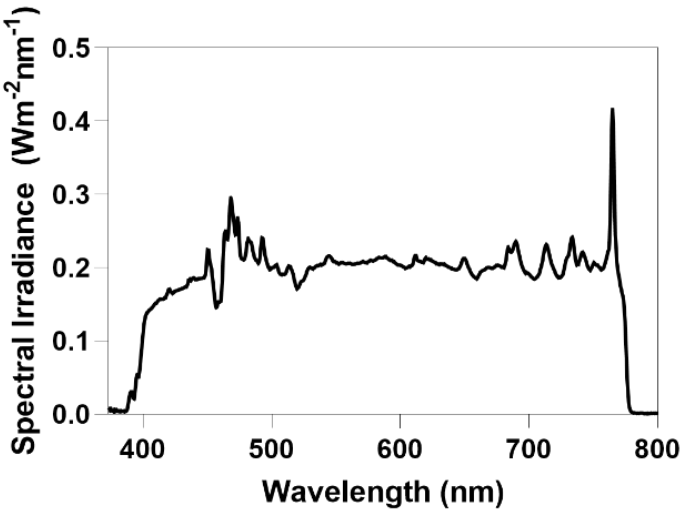

Figure A.2. Spectral irradiance of the 300 W Xenon arc lamp (Newport 6259) equipped with a bandpass filter ($400 < \lambda < 700$ nm) used in the photocatalytic activity experiments of gram-positive bacteria MRSA and VRE.

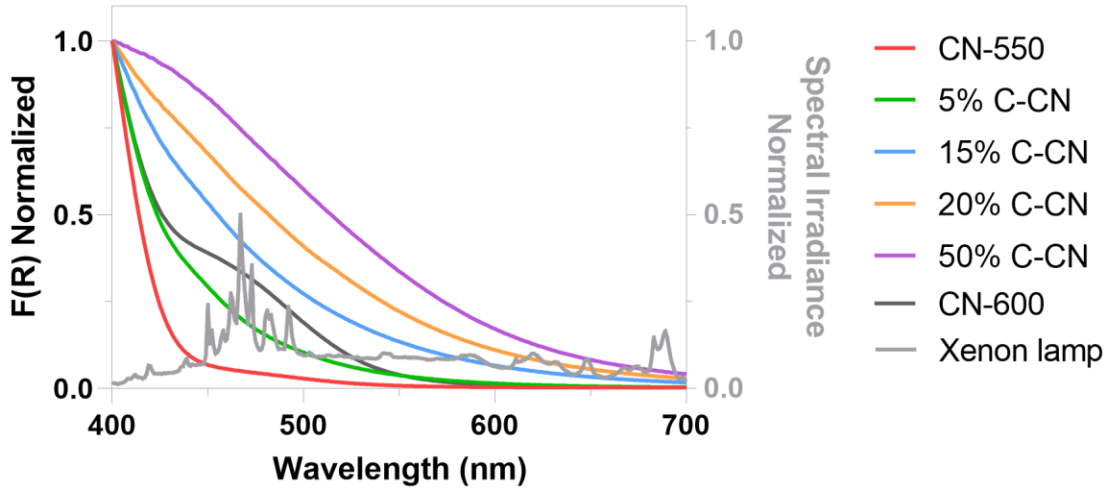

Figure A.3. Absorbance of powder g-C_3N_4 samples measured with a UV-Vis-NIR spectrophotometer, and spectral irradiance of 300 W Xenon lamp (Sciencetech SLB300B). Each spectrum was normalized to its maximum absorption in the wavelength range of 400 to 700 nm.

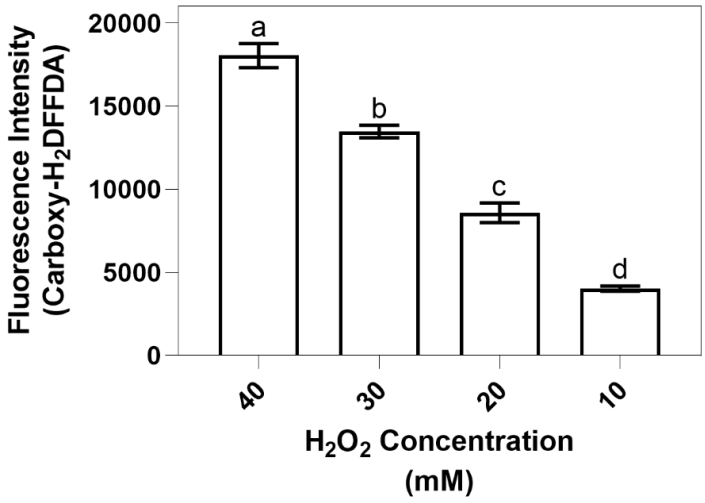

Figure A.4. Carboxy-H_2DFFDA as an indicator for reactive species (RS) production. Fluorescence intensity progressively increases with increasing hydrogen peroxide (H_2O_2, diluted in PBS) concentration, suggesting that the intensity of the selected dye correlates well with RS production. Means suffixed with different letters (a–d) are significantly different from each other ($P < 0.05$). Error bars represent standard deviation (n=4).

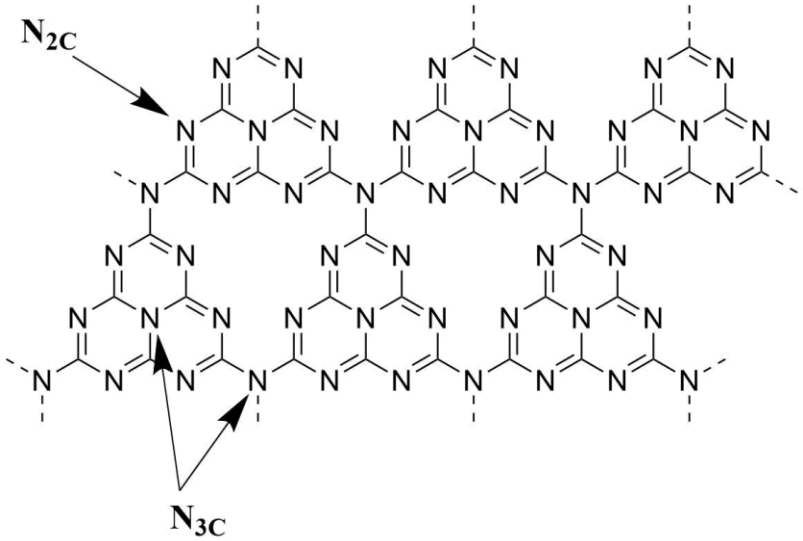

Figure A.5. Schematic structure of g-C_3N_4 containing two nitrogen configurations.

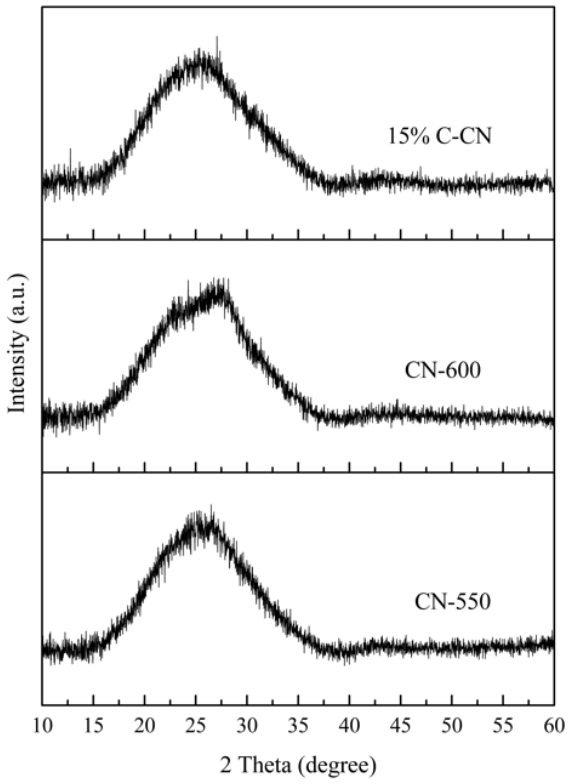

Figure A.6. XRD patterns of g-C_3N_4 samples 15% C-CN (C-doping method), CN-660 (different pyrolysis temperature method), and CN-550 (base).

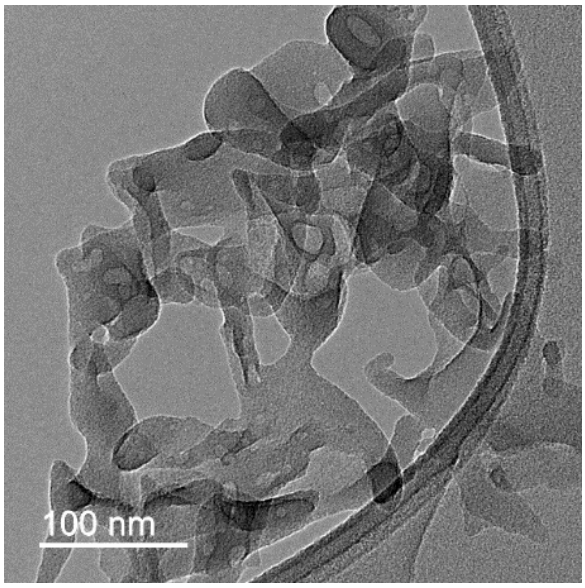

Figure A.7. TEM image showing the morphology of sample CN-550.

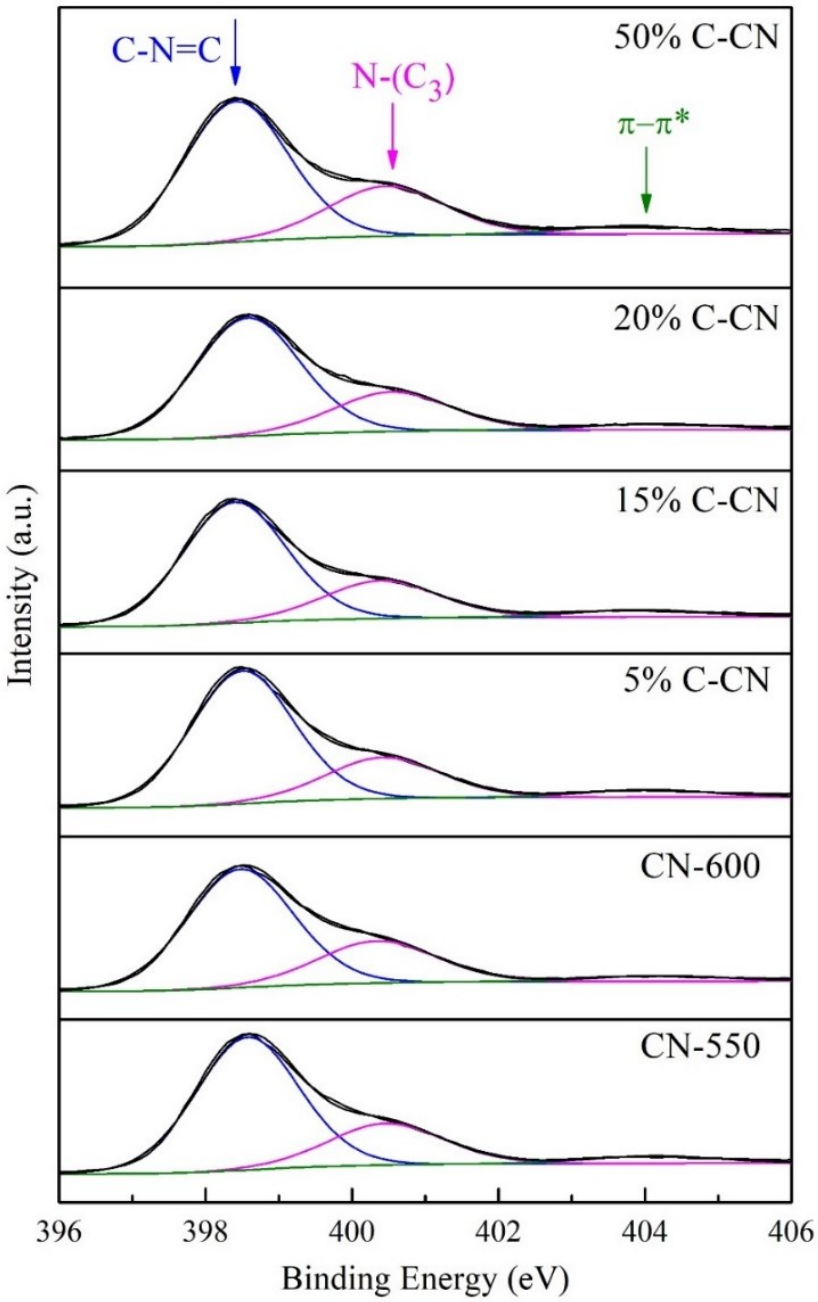

Figure A.8. XPS high-resolution N 1s spectra of g-C_3N_4 samples. For each sample, three N 1s spectra were collected at different locations. Peak deconvolution was performed for each N 1s spectrum, and the average values for N_{2C} and N_{3C} components were compiled in Table 2.1.

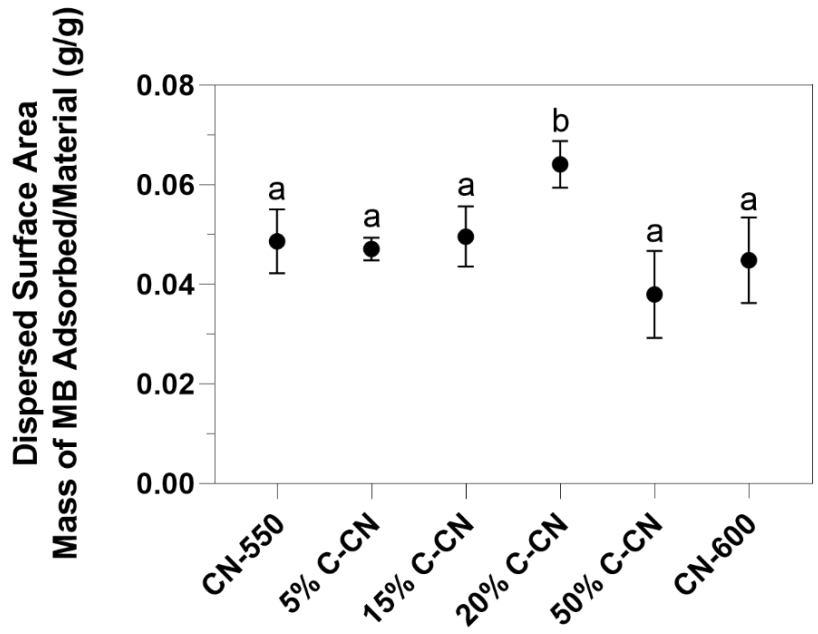

Figure A.9. Dispersed surface area by methylene blue (MB) method in saline solution determined by the mass of MB adsorbed over mass of the g-C_3N_4 material. Means suffixed with different letters (a–b) are significantly different from each other ($P < 0.05$). Error bars indicate standard deviation (n=6). The dispersed surface area is not significantly different between the prepared samples, except for sample 20% C-CN, which shows a slight increase in available surface area compared to the others (0.064 vs ~0.048 g MB/g g-C_3N_4).

Figure A.10. Prepared g-C_3N_4 samples. From left to right: CN-600, CN-550, 5% C-doped CN, 15% C-doped CN, 20% C-doped CN, 50% C-doped CN.

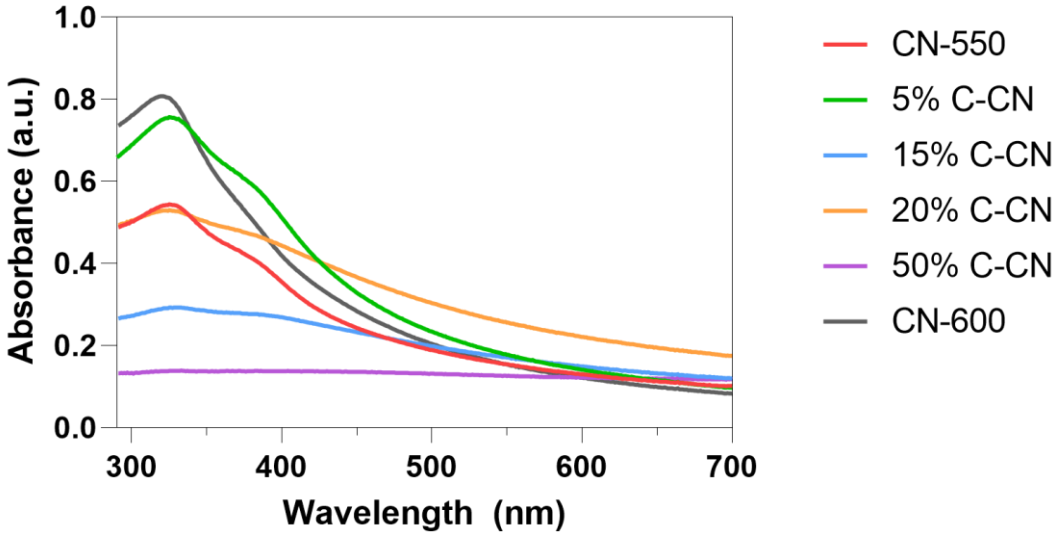

Figure A.11. Optical absorbance of g-C_3N_4 samples in suspension by UV-Vis spectroscopy. All g-C_3N_4 materials were dispersed in PBS (1 mM, pH 7.4) at the same concentration (19 mg L^{-1}).

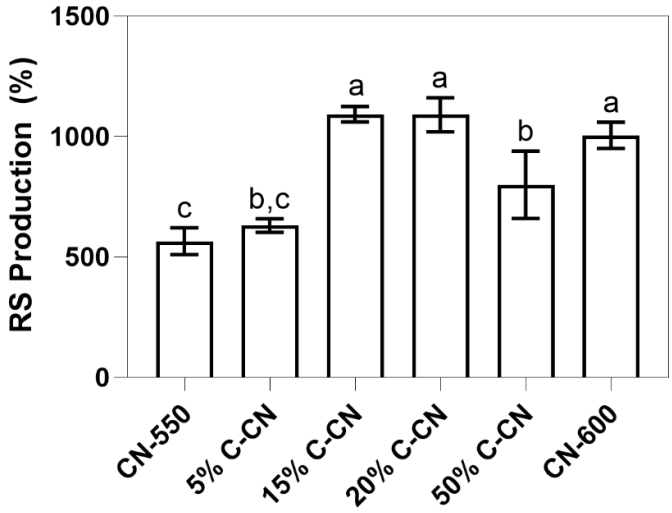

Figure A.12. Percent reactive species (RS) production by the g-C_3N_4 samples after 5 minutes of visible-light irradiation. Means suffixed with different letters (a–c) are significantly different from each other ($P < 0.05$). Error bars indicate standard deviation (n=3).

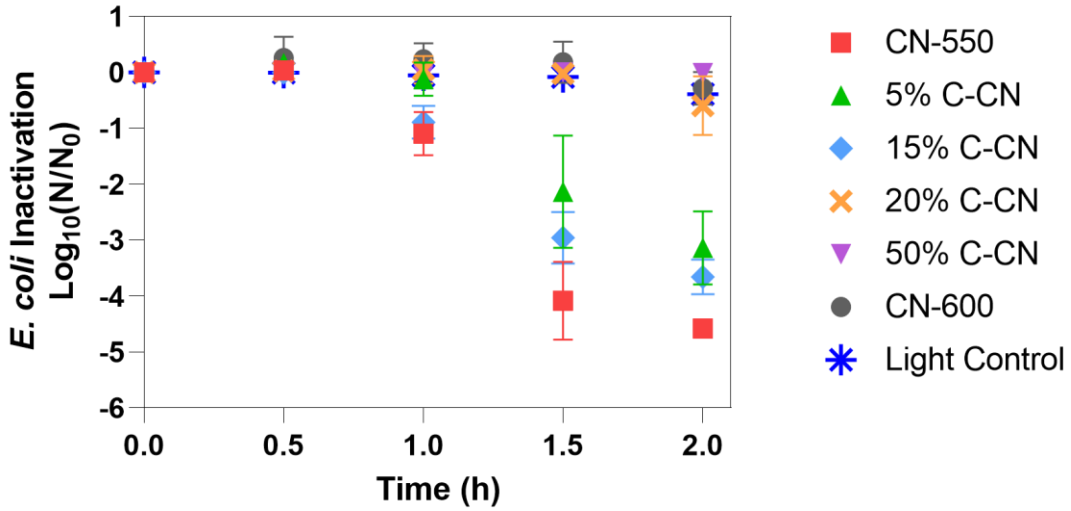

Figure A.13. Photocatalytic inactivation of *E. coli* by g-C_3N_4 materials irradiated with visible light (400 < λ < 700 nm). Reaction mixture contains bacterial solution and g-C_3N_4 dispersed in saline solution (400 mg L-1). Light control contains bacterial solution and saline solution without photocatalyst. Error bars indicate standard deviation (for CN-550 n=4, for others n=3).

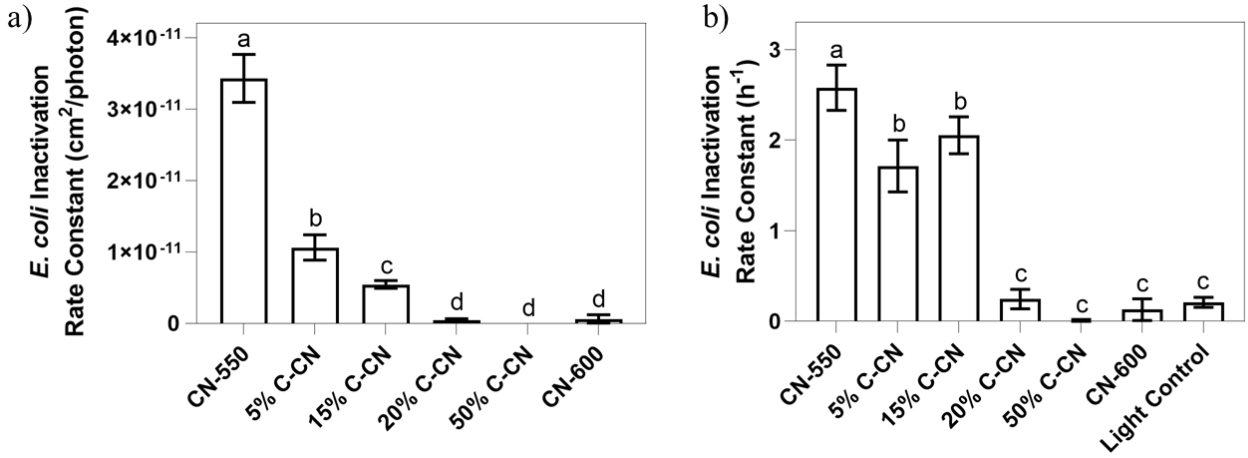

Figure A.14. *E. coli* inactivation rate constants normalized (a) and non-normalized (b) by photon flux. Means suffixed with different letters (a–d) are significantly different from each other (P < 0.05). Error bars indicate standard deviation.

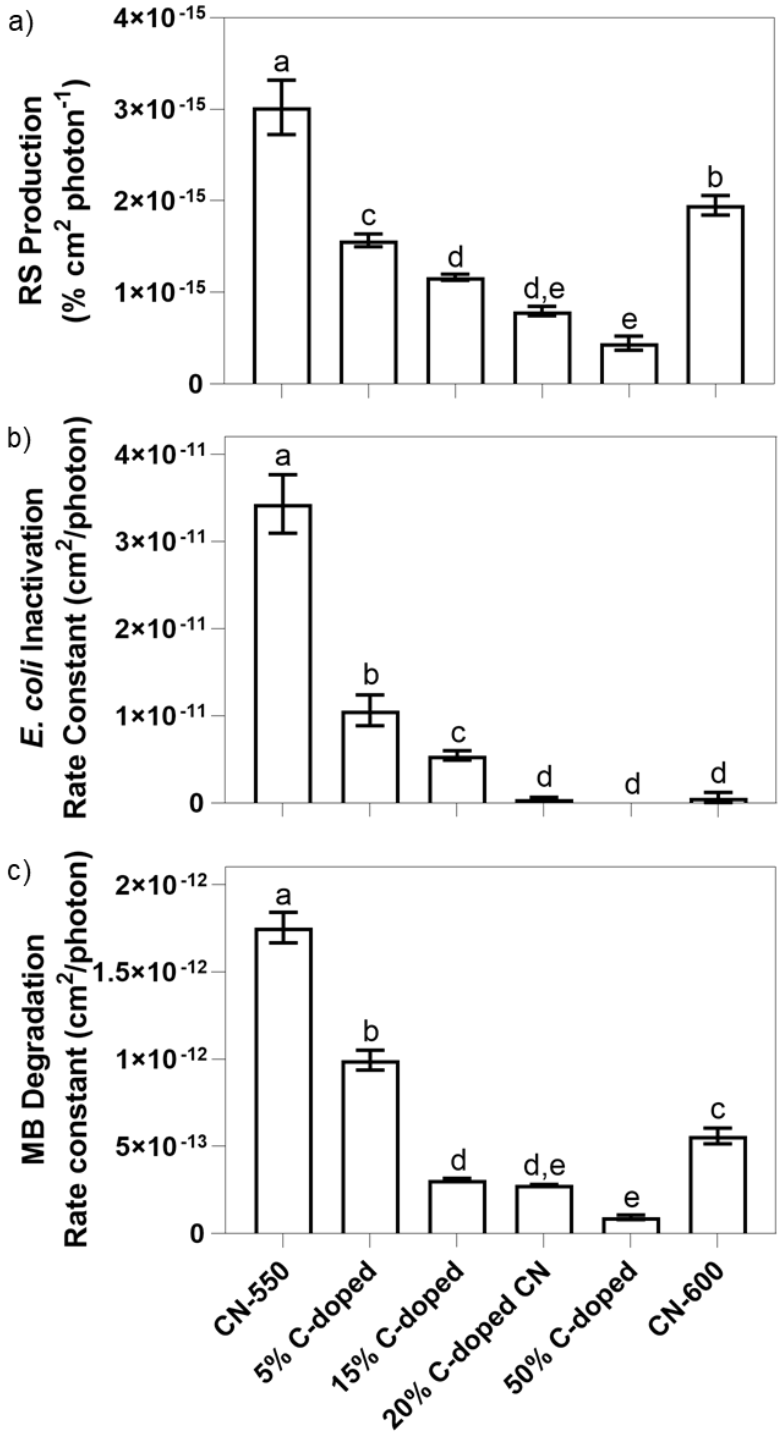

Figure A.15. RS production photon fluence normalized (a), rate constants photon flux normalized for *E. coli* inactivation (b) and MB degradation (c). Means suffixed with different letters (a–e) are significantly different from each other ($P < 0.05$). Error bars indicate standard deviation.

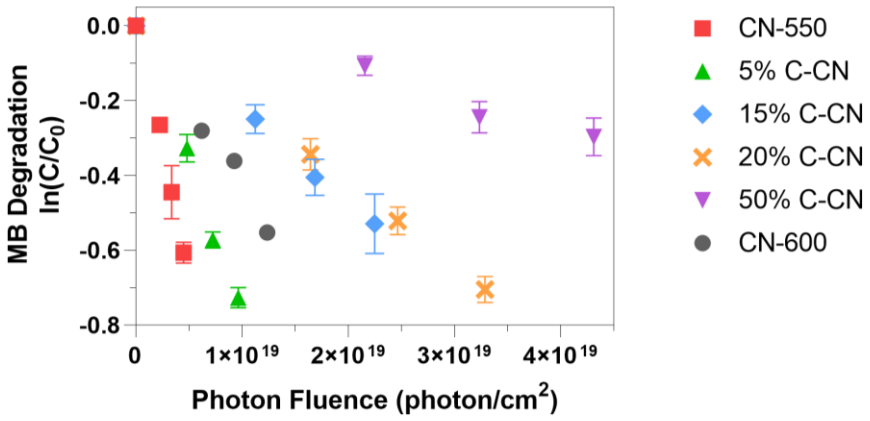

Figure A.16. Photocatalytic degradation of methylene blue (MB) by g-C_3N_4 materials irradiated with visible light (400 < λ < 700 nm) vs. the photon fluence associated with each sample. Reaction mixture contains MB in saline solution mixed with g-C_3N_4. Light control contains MB in saline solution without photocatalyst. Error bars indicate standard deviation (n=2).

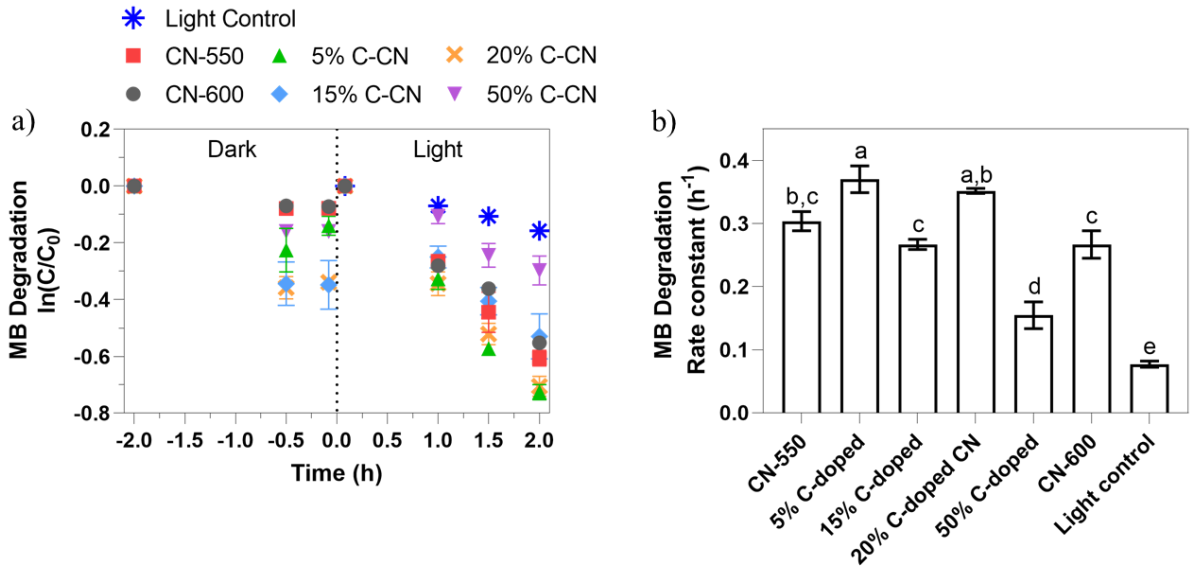

Figure A.17. Photocatalytic degradation (a), and degradation rate constants (b) of methylene blue (MB) by g-C_3N_4 irradiated with visible light (400 < λ < 700 nm). Reaction mixture contains MB in saline solution mixed with g-C3N4. Light control contains MB in saline solution without photocatalyst. Means suffixed with different letters (a–e) are significantly different from each other (P < 0.05). Error bars indicate standard deviation (n=2).

Table A.1. Compiled results on property-antibacterial activity relationships from studies of g-C_3N_4 (pristine and C-doped) used for photocatalytic bacterial inactivation in solution under visible-light irradiation.

g-C_3N_4 material (Nº. unique samples)	Synthesis and modification approach	Target bacterium	Properties Characterized	Identified governing physicochemical properties for improved photocatalytic activity [a]	Takeaways and limitations	Ref
Ultrathin g-C_3N_4 nanosheets (5)	Bulk: thermal condensation of melamine at 550 °C (g-C_3N_4) One control sample without the freezing step (MW-CN). Nanosheets: rapid microwave-assisted alternated cooling and heating treatment method. Two samples with different microwave power (ACHT-CN-500, ACHT-CN-1000). One control sample without the microwaving step (FF-CN).	*Escherichia coli (E. coli)* K12	- Morphology: Transmission electron microscopy (TEM), Atomic force microscopy (AFM) - Brunauer-Emmett-Teller (BET) Surface area and Pore volume: Nitrogen adsorption-desorption isotherms. - Crystal structure: X-ray diffraction (XRD) - Crystal structure and functional groups: Fourier transform infrared (FTIR) - Elemental composition: X-ray photoelectron spectroscopy (XPS) - Band gap: UV-Visible diffuse reflection spectroscopy (DRS)/Tauc plot - Electron transport ability: Steady-state photoluminescence (ss-PL), Electrochemical impedance spectroscopy (EIS), Transient photocurrent	The synergistic effects of: - High crystallinity - Large surface area - Narrow bandgap - High electron transport ability	The identified governing properties correlate well with *E. coli* inactivation and reactive species (RS) production. Transient photocurrent was only measured for bulk g-C_3N_4 and ACHT-CN-1000.	63
Atomic single layer g-C_3N_4 (3)	Bulk: thermal condensation of melamine at 520 °C (bulk g-C_3N_4) Nanosheets: thermal etching of bulk g-C_3N_4 (g-C_3N_4 NS) Single layers: ultrasonic exfoliation of g- C_3N_4 NS (SL g-C_3N_4)	*E. coli* [c]	- Morphology: field emission scanning electron microscope (FE-SEM), TEM, AFM - Crystal structure: XRD - Chemical structure: FTIR - Charge transfer resistance: EIS - Charge separation: Photocurrent	- Ultrathin sheet thickness - Low charge-transport resistance - Efficient charge separation	Only two samples (bulk g-C_3N_4 and SL g-C_3N_4) were characterized for charge separation and transport. For those two samples, the governing properties correlate well with *E. coli* inactivation.	36

Table A.1 (continued)

Bacteria-treated porous g-C^3N_4 nanosheets (4)	Bulk: thermal condensation of melamine at 550 °C (g-C_3N_4) Nanosheets: bio-exfoliation with bacterial culture times of 4 h, 2 d and 5 d (BT-CN-4h, BT-CN-2d, BT-CN-5d) One control sample without the addition of bacteria (UN-CN)	*E. coli* K12	- Morphology: TEM, AFM - Surface area: BET - Pore size distribution: Barrett−Joyner−Halenda (BJH) - Crystal structure: XRD - Chemical groups: FTIR - Surface chemical composition: XPS - Band gap: UV-Vis DRS/Tauc plot - Unpaired electrons: Electron paramagnetic resonance (EPR) - Charge separation and transport ability: EIS, Transient photocurrent	- Large surface area - Narrow band gap - Enriched unpaired electrons - Higher electron transport ability	All identified governing properties correlate well with *E. coli* inactivation and RS production, except for band gap. Band gap was the same for all nanosheets samples, and those were smaller than bulk g-C_3N_4. EPR and transient photocurrent were only measured for g-C_3N_4 and BT-CN-2d.[b]	64
g-C_3N_4 quantum dots (3)	Bulk: thermal condensation of melamine at 600 °C (bulk g-CN) Mesoporous: bulk g-CN with H_2SO_4 (mpg-CN) Quantum dots: thermal polymerization using melamine and EDTA (g-CN QDs)	*E. coli* (ATCC 25922) and *Staphylococcus aureus (S. aureus*, ATCC 23235*)*	- Crystal structure: XRD - Morphology: TEM, AFM - Surface structure: FTIR - Surface chemical composition: XPS - Surface area: BET - Pore size distribution: BJH - Pore volume: N_2 adsorbed at $p/p_0 \sim 0.9$ - Band gap: UV-Vis DRS/Tauc plot - VB and CB positions: equation - Charge recombination: ss-PL - Zeta potential	- Larger surface area, increasing active sites - Optical absorption in UV and visible region	*E. coli* and *S. aureus* inactivation correlate well with surface area and ss-PL, but not with band gap.[b] g-CN QDs inactivate Gram-negative *E. coli* faster than gram-positive *S. aureus.*	159

Table A.1 (continued)

Porous g-C_3N_4 nanosheet (3)	Bulk: thermal condensation of melamine at 550 °C (BCN) g-C_3N_4 with nanopores: hydrothermal treatment of BCN (PCN) Mesoporous nanosheets: thermal etching of PCN (PCNS)	*E. coli* K12	- Adsorptivity: Adsorption of Methylene blue (MB) in solution - Morphology: TEM, AFM - Surface area: BET - Pore volume - Crystal structure: XRD - Chemical structure: FTIR - Band gap: DRS - Chemical states and composition: XPS - Charge transfer and separation: ss-PL, Time-resolved (tr-PL), Photocurrent, EIS - Superoxide radicals quantification: Electron spin resonance (ESR)	- High surface area, producing more surface reactive sites - Improved sorption for the probe pollutants can accelerate the rate of photocatalytic reaction - Expanded band gap - Increased amounts of superoxide radicals and holes dominating the photocatalytic reaction - Decreased thickness and well-developed porosity - Improved efficiency of charge transfer and separation	*E. coli* inactivation and MB degradation do not correlate well with band gap and ss-PL, but they correlate well with surface area, adsorptivity, ESR, AFM, pore volume, tr-PL, photocurrent, and EIS.[b] Band gap was the same for PCN and BCN, and those were smaller than BCN.	108
Mesoporous g-C_3N_4 (3)	Bulk g-C_3N_4: thermal condensation of cyanamide at 550 °C (CN12) Mesoporous: the self-condensation of cyanamide in the presence of different amount of a silica template (CN128, CN230)	*E. coli* K12	- Surface area: BET - Pore volume: BJH - Crystal structure: XRD - Chemical structure: FTIR - Band gap: DRS	- The large surface area provides more active sites to generate holes for the reaction and hence results in high activity	The identified governing property of surface area correlates well with *E. coli* inactivation.	37

Table A.1 (continued)

Porous defective g-C_3N_4 ultrathin nanosheets – nitrogen defects (5)	Bulk g-C_3N_4: thermal condensation of urea at 550 °C (CN) Porous nanosheets: thermal polymerization of freeze-dried HCl-pretreated urea. Modified by changing the pH (CN-2, CN-4, CN-6 and CN-8)	*E. coli* K12 and *S. aureus* [c]	- Crystal structure and phase purity: XRD - Structure variation: FTIR - Elemental composition: XPS - Nitrogen vacancies: magic angle spinning nuclear magnetic resonance (MAS NMR) - Unpaired electrons: EPR - Morphology and element analysis: Field emission scanning electron microscopy (FESEM), TEM, AFM - BET surface area and pore size distribution: N_2 adsorption-desorption - Surface protonation degree and hydrophilicity: Zeta potential and Contact angle - Band gap: UV-Vis DRS/Tauc plot - VB and CB positions: VB-XPS and Mott-Schottky plots - Charge separation and transport: ss-PL, tr-PL, Photocurrent, EIS	The synergistic effects of: - Enhanced light absorption ability - More active sites exposed - Accelerated mass diffusion and transfer - Increased separation and inhibited recombination efficiency of electrons and holes	*E. coli* and *S. aureus* inactivation correlate well with ss-PL, tr-PL, and EIS. The trends for band gap, surface area, pore volume, and photocurrent are not directly correlated to bacterial inactivation.[b]	154
Porous g-C_3N_4 nanosheets (6)	Bulk g-C_3N_4: thermal polymerization of urea at 550 °C (BCN) Nanosheets: one-step chemical exfoliation. Modified by changing exfoliation time (PCNS2, PCNS3, PCNS4, PCNS5, PCNS6)	*E. coli* K12	- Crystal structure: XRD, FTIR - Morphology: TEM, AFM - Composition and chemical states: XPS - Surface area: BET - band gap: UV-Vis DRS - Band positions: VBXPS - Charge transfer and separation: ss-PL, Photocurrent, EIS	- Efficient charge separation	*E. coli* inactivation correlates with ss-PL and EIS, except for sample PCNS4. It does not correlate well with transient photocurrent.[b]	205

[a] Performance includes bacterial inactivation, MB degradation and/or RS production.

[b] Lack of correlation between the identified governing properties and the antibacterial activity indicates that these properties are important, but not conclusive factors in improving photocatalytic bactericidal performance.

[c] Strain not indicated in study.

Table A.2. Linear regression models and first-order rate constants for *E. coli* inactivation by g-C_3N_4 samples.

Sample	Linear regression model [A]	First order decay rate constant k (h^{-1}) (avg ± SD)
Light control	Y = -0.397*X + 0.152	-0.397 ± 0.098
CN-550	Y = -5.936*X + 1.478	-5.936 ± 0.578
5% C-doped CN	Y = -3.949 *X + 1.536	-3.949 ± 0.657
15% C-doped CN	Y = -4.724*X + 1.265	-4.724 ± 0.470
20% C-doped CN	Y = -0.568*X + 0.313	-0.568 ± 0.247
50% C-doped CN	Y = -0.008*X - 0.026	-0.008 ± 0.041
CN-600	Y = -0.298*X + 0.476	-0.298 ± 0.275

[A] $Y = \ln(N/N_0)$; X = time in hours. Standard deviation (SD) includes 4 replicates for CN-550 and 3 replicates for other samples.

Table A.3. Linear regression models and first-order rate constants for *E. coli*, MRSA and VRE inactivation by CN-550.

Sample	Linear regression model[A]	First order decay rate constant k (h^{-1}) (avg ± SD)
E. coli	Y = -5.936*X + 1.478	-5.936 ± 0.578
MRSA	Y = -12.290*X + 1.041	-12.290 ± 3.623
VRE	Y = -11.890*X + 0.350	-11.890 ± 1.264

[A] $Y = \ln(N/N_0)$; X = time in hours. Standard deviation (SD) includes 4 replicates for *E. coli* and 3 replicates for MRSA and VRE.

Table A.4. Linear regression models and first-order rate constants for MB degradation by g-C_3N_4 samples.

Sample	Linear regression model[A]	First order decay rate constant k (h^{-1}) (avg ± SD)
Light control	Y = -0.077*X + 0.003	-0.077 ± 0.005
CN-550	Y = -0.304*X + 0.013	-0.304 ± 0.015
5% C-doped CN	Y = -0.370*X + 0.010	-0.370 ± 0.021
15% C-doped CN	Y = -0.267*X + 0.004	-0.267 ± 0.008
20% C-doped CN	Y = -0.352*X + 0.003	-0.352 ± 0.004
50% C-doped CN	Y = -0.155*X + 0.012	-0.155 ± 0.021
CN-600	Y = -0.267*X + 0.002	-0.267 ± 0.022

[A] $Y = \ln(C/C_0)$; X = time in hours. Standard deviation (SD) includes 2 replicates.

Table A.5. Zeta potential of the g-C_3N_4 samples in saline solution (pH 5–6).

Sample	Zeta potential (mV)
CN-550	-31.25
5% C-doped	-27.90
15% C-doped	-27.85
20% C-doped	-28.90
50% C-doped	-29.45
CN-600	-25.15

Appendix B Supporting Information for Chapter 3

B.1 Synthesis Methods and Life Cycle Inventory Details

B.1.1 Synthesis of Bulk g-C_3N_4

B.1.1.1 Synthesis Procedure: Bulk g-C_3N_4 is used as the precursor to four g-C_3N_4 nanosheets syntheses considered in this study. The synthesis details of bulk g-C_3N_4 varies within these four studies as presented below:

- In bioexfoliation[64]: melamine was encapsulated in a covered ceramic crucible at 550 °C for 4 h using a muffle furnace; the heating speed is 5 °C min^{-1}
- In chemical exfoliation[89]: melamine was heated at 600 ℃ for 2 h under air condition with a ramp rate of about 3 ℃ min^{-1} for both of the heating and cooling processes
- In thermal etching[36]: 5 g of melamine was calcined at 520 ℃ for 4 h with the heating rate of 5 ℃ min^{-1}
- In C-doped[72]: 10 g of melamine was put into an alumina crucible with a cover, and then heated at 550 °C at the rate of 5 ℃ min^{-1} in a tube furnace for 4 h in air

The synthesis details that could affect the environmental impacts of producing bulk g-C_3N_4 include the mass of melamine (5 or 10 g), the heating temperature (520, 550 or 600 ℃), the heating rate (3 or 5 °C min^{-1}), the heating time (2 or 4 h), and the type of furnace used (muffle furnace or tube furnace).

Further, complete information needed to build the LCI for the synthesis of bulk g-C_3N_4 is not universally available. Therefore, we used a combination of details from the four references to establish a conservative (i.e., lowest energy) synthesis configuration: 10 g of melamine heated at 520 ℃ at the heating rate of 5 ℃ min^{-1} in a tube furnace for 2 h in air.

B.1.1.2 Synthesis Yield: The synthesis yield was not reported in the referenced papers. Thus, 100% yield was assumed with melamine as the limiting reagent.

B.1.1.3 LCI Details:

LCI Inputs

i. 10 g of melamine

ii. Electricity (calcination): Calculated for a heating temperature of 520 °C for 2 h using a tube furnace, when the heating rate is 5 °C min^{-1}. The total electricity used for calcination is 2.92 kWh (details below)

- Assuming the Thermo Scientific Lindberg/Blue M TF55035A-1 tube furnace with power consumption of 800 W

Electricity input calculations:

Total time of tube furnace turned on for heating:

Start temperature = 25 °C (room temperature)

Annealing temperature = 520 °C

Time to reach annealing temperature = (520 °C – 25 °C) / (5 °C/min) = 99 min

Total time of furnace turned on = 99 min + 2 h = 3.65 h

Electricity consumed = Device power consumption (W) × time of use (h)

Total = 800 W × 3.65 h = 2.92 kWh

LCI Emissions to Air

i. 0.37 g of Ammonia

Table B.1. Life cycle inventory to produce bulk g-C_3N_4 from melamine, including the Pedigree matrix for unit the processes (all distributions assumed to be lognormal).

	Section	Material	Amount	Unit	LCI Database	Pedigree matrix SD^2	Comments
7.3 g of bulk g-C_3N_4	Input	Melamine	10	g	Melamine, at plant/US- US-EI U US-EI	1,4,2,1,1,na 1.12	The mass of melamine was calculated considering 100% synthesis yield when producing g-C_3N_4 based on [206,207] $C_3H_6N_6 \rightarrow$ g-C_3N_4 + 2 NH_3
Yield 100% Based on [206]		Electricity	2.92	kWh	Electricity mix 2018/US U US-EI	4,4,1,1,1,na 1.24	Used for calcination
	Emission to air	Ammonia	2.16	g		2,4,5,1,1,na 1.53	Approximately 1.6 NH_3 liberated by melamine pyrolysis at 520 °C for 2 h (mole/mole melamine). Based on [206]

B.1.2 Supramolecular Synthesis of g-C_3N_4 Nanosheets

B.1.2.1 Synthesis Procedure: The supramolecular-based g-C_3N_4 nanosheets synthesis is based on our previous work.[153] Melamine (1 g) and cyanuric acid (1.02 g, in a molar ratio 1:1) were dispersed into 40 mL of ethanol and the mixture was stirred at room temperature for 3 h. After stirring, the suspension was bath sonicated at room temperature for 1 h and then dried at 70 °C on a hot plate in air until only a solid material remained (16 hours). The solid was ground using an agate mortar and pestle to form a fine powder. Finally, the powder was transferred to a quartz crucible with cover, heated at a rate of 2.3 °C min^{-1}, under gas helium flow, maintained at 550 °C for 4 h, and cooled down naturally.

B.1.2.2 Synthesis Yield: 100% yield was assumed to enable comparison with other methods. Melamine was considered the limiting reagent.

B.1.2.3 LCI Details:

LCI Inputs

i. 1 g melamine

ii. 1.02 g of cyanuric acid

- The synthesis of cyanuric acid was created based on the procedures reported by She *et al.*[208] In detail, 20 g of urea was added to 40 mL of kerosene as solvent. The mixture was stirred at 150 °C, placed under vacuum, and then heated at 190 °C until the reaction was complete. The reaction mixture was cooled to 80 °C, put into 15 mL of water, and stirred for 1 hour to precipitate the product. The obtained dry solid was heated to 150 °C for 2 hours to remove the crystallization water and afford pure cyanuric acid. The synthesis yield is 89%.

Electricity calculations using the Thermo Scientific™ SP88854100 stirring hot plate with power consumption of 540 W:

i. Stirring: Assumed 3 h. 540 W × 3 h = 1.62 kWh

ii. Heating: Assumed 4 h. 540 W × 4 h = 2.16 kWh

iii. Stirring: 1 h. 540 W × 1 h = 0.54 kWh

iv. Drying: 2 h. 540 W × 2 h = 1.08 kWh

Total = (1.62 + 2.16 + 0.54 + 1.08) = 5.4 kWh

iii. 40 mL of ethanol, which is equal 31.56 g of ethanol (density of 0.789 g/mL)

iv. Helium gas: assuming flow of 100 mL/min, and temperature of 21 ℃

- 100 mL/min × 7.8 h = 46.8 L of He. Mass = 46.8 L × 0.16 kg/m^3 × 1 m^3/1000 L = 0.00749 kg = 7.49 g

v. Electricity (stirring): 3 h duration

- Considering the Thermo Scientific™ SP88854100 stirring hot plate with power consumption of 540 W

Electricity (sonication): 1 h duration

- Using the Aquasonic 150 HT bath sonicator with power consumption of 400 W

Electricity (drying): 16 h duration

- Assuming the Thermo Scientific™ SP88854100 stirring hot plate with power consumption of 540 W

Electricity (calcination): Calculated for a heating temperature of 550 °C for 4 h using a tube furnace, when the heating speed is 2.3 °C min^{-1}

- Assuming the Thermo Scientific Lindberg/Blue M TF55035A-1 tube furnace with power consumption of 800 W

Electricity input calculations:

Total time of tube furnace turned on for heating:

Start temperature = 25 °C (room temperature)

Annealing temperature = 550 °C

Heating rate = 2.3 °C/min

Time to reach annealing temperature = (550 °C – 25 °C) / (2.3 °C/min) = 228 min = 3.8 h

Total time of furnace turned on = 3.8 h + 4 h = 7.8 h

Electricity consumed = Device power consumption (W) × time of use (h)

- Stirring = 540 W × 3 h = 1.62 kWh
- Bath sonication = 400 W × 1 h = 0.4 kWh
- Drying (hot plate) = 540 W × 16 h = 8.64 kWh
- Calcination (tube furnace) = 800 W × 7.8 h = 6.24 kWh

Total = (1.62 + 0.4 + 8.64 + 6.24) kWh = 16.9 kWh

LCI Emissions to Air

i. 0.27 g of Ammonia

ii. 1.02 g of Cyanic acid

iii. 31.56 g Ethanol

iv. 7.49 g of Helium

Table B.2. Life Cycle Inventory to produce g-C_3N_4 nanosheets by supramolecular route, including the Pedigree matrix for the unit processes (all distributions assumed to be lognormal).

	Section	Material	Amount	Unit	LCI Database	Pedigree matrix SD^2	Comments
1 g of g-C_3N_4 nanosheets	Input	Melamine	1.38	g	Melamine, at plant/US- US-EI U US-EI	1,4,1,1,1,na 1.11	
Yield 100%		Cyanuric Acid	1.41	g	Created	1,4,1,1,1,na 1.11	Based on [208]
		Ethanol	43.55	g	Ethanol from ethylene, at plant/US- US-EI U US-EI	1,4,1,1,1,na 1.11	
		Helium	7.49	g	Helium, at plant/GLO US-EI U US-EI	2,4,1,1,1,na 1.12	Calcination inert gas
		Electricity	16.9	kWh	Electricity mix 2018/US U US-EI	4,4,1,1,1,na 1.24	Used for stirring, sonication, drying, and calcination
	Emission to air	Ammonia	0.37	g		2,4,5,1,1,na 1.53	Approximately 2 NH_3 liberated by melamine pyrolysis at 550 °C for 4h (mole/mole melamine). Based on [206,207] $C_3H_6N_6 \rightarrow$ g-C_3N_4 + 2 NH_3
		Isocyanic acid	1.41	g		2,4,5,1,1,na 1.53	All cyanuric acid is decomposed into cyanic acid at 550 °C. Based on [209,210] $(CNOH)_3$ (s) → 3 HNCO (g)

Table B.2. (continued)

		Ethanol	43.55	g		1,4,1,1,1,na 1.11	Evaporation
		Helium	7.49	g		2,4,1,1,1,na 1.12	Calcination inert gas
Cyanuric Acid (for 12.75 g)		Urea	9.2	g	Urea, as N, at regional storehouse/US- US-EI/U US-EI	1,4,4,3,1,na 1.24	This LCI refers to 1 kg of N, resp. 2.17 kg urea with a N-content of 46%. Thus, to account for the 20 g of urea needed, the amount of 9.2 g is used
Yield 89% Based on [208]		Kerosene	40	mL	Kerosene, at refinery/I/US USLCI	1,4,4,3,1,na 1.24	
		Deionized water	15	g	Water, deionised, at plant/US* US- EI U US-EI	1,4,4,3,1,na 1.24	
		Electricity	5.4	kWh	Electricity mix 2018/US U US-EI	4,4,1,1,1,na 1.24	Used for stirring, heating, drying
	Emission to air	Ammonia	5.67	g		1,4,4,3,1,na 1.24	$3\ CH_4N_2O \rightarrow (CNOH)_3 + 3\ NH_3$ Based on [208]
		Water	15	g		1,4,4,3,1,na 1.24	Evaporation

B.1.3 Biological Exfoliation Synthesis of g-C_3N_4 Nanosheets (with Bacterial Culture)

B.1.3.1 Synthesis Procedure: The synthesis of g-C_3N_4 nanosheets using the bio-exfoliation with bacterial culture approach reported by Kang *et al*.[64] was followed in this study. The g-C_3N_4 nanosheets were synthesized by moderate bacterial post treatment of bulk g-C_3N_4 (*vide supra*). 20 µL of saturated *E. coli* bacterial solution were inoculated in 200 mL of the culture medium, to which 5 g of bulk g-C_3N_4 was added. After 4 h of shock culturing in the dark at 37 °C, the bioetched g-C_3N_4 was separated by centrifugation at 10,000 rpm. Finally, the obtained yellow powder was calcinated at 550 °C for 4 h using a muffle furnace to remove the possible bacterial residue.

B.1.3.2 Synthesis Yield: The synthesis yield was not reported in the referenced paper. Thus, 100% yield was assumed to enable comparison with other methods. Bulk g-C_3N_4 was considered the limiting reagent.

B.1.3.3 LCI Details

LCI Inputs

i. 5 g bulk g-C_3N_4

ii. *E. coli* bacteria was not included in the LCI

iii. 200 mL of culture medium

- Culture medium is composed of 5 g yeast extract, 10 g peptone, 1 L deionized water, 10 g NaCl. It was autoclaved for 15 minutes, which takes about 40 minutes for the whole cycle. Assuming the Fisherbrand™ SterilElite™ STE1622004, a small autoclave (16 L), with a power consumption of 1400 W

- *Electricity consumed* = Device power consumption (W) × time of use (h) = 1400 W × 0.67 h = 0.94 kWh

iv. Electricity (incubation): At a temperature of 37 °C for 4 h

- Assuming the Fisherbrand™ Microbiological Incubator, 60 L, with power consumption of 300 W

Electricity (centrifugation): Considering 10,000 rpm for10 minutes (assumed)

- Assuming the Fisherbrand™ HORIZON™ 24 Clinical Centrifuge with power consumption of 220 W

Electricity (calcination): Calculated for a temperature of 550 °C for 4 h, when the heating speed is 5 °C min^{-1} (the heating speed and furnace were not informed; therefore, it was assumed to be the same as the one reported to produce their bulk g-C_3N_4)

- Assuming the Thermo Scientific™ BF51866C1 muffle furnace with power consumption of 1800 W

Electricity input calculations:

Total time of tube furnace turned on for heating:

Start temperature = 25 °C (room temperature)

Annealing temperature = 550 °C

Heating rate = 5 °C/min

Time to reach annealing temperature = (550 °C – 25 °C) / (5 °C/min) = 105 min

Total time of furnace turned on = 105 min + 4 h = 5.75 h

Electricity consumed = Device power consumption (W) × time of use (h)

- Incubation = 300 W × 4 h = 1.2 kWh

- Centrifugation = 220 W × 0.17 h = 0.037 kWh

- Calcination nanosheets = 1800 W × 5.75 h = 10.35 kWh

Total = (1.2 + 0.037 + 10.35) kWh = 11.59 kWh

Table B.3. Life cycle inventory to produce g-C_3N_4 nanosheets via biological exfoliation route, including the Pedigree matrix for the unit processes (all distributions assumed to be lognormal).

	Section	Material	Amount	Unit	LCI Database	Pedigree matrix SD^2	Comments
1 g of g-C_3N_4 nanosheets via biological route	Input	Bulk g-C_3N_4 from melamine	1	g	Created	1,4,2,3,1,na 1.12	Details shown in Table S1
Yield 100%		Culture medium	40	g	Created	1,4,2,3,1,na 1.12	Assuming 40 mL = 40 g. Based on [87]
		Electricity	11.59	kWh	Electricity mix 2018/US U US-EI	4,4,1,1,1,na 1.24	Used for incubation, centrifugation, and calcination
Culture medium (for 1 L or 1000 g)	Input	Yeast extract	5	g	Created		Based on [87]
		Peptone	10	g	Created		Based on [87]
		Deionized water	1000	g	Water, deionised, at plant/US* US- EI U US-EI		
		Sodium chloride	10	g	Sodium chloride, powder, at plant/US- US EI U US-EI		
		Electricity	0.94	kWh	Electricity mix 2018/US U US-EI		Autoclaving

Table B.3. (continued)

Yeast Extract (for 262.35 g)	Input	Yeast	500	g	Fodder yeast, [211], ethanol production from whey, Cut-Off, U Ecoinvent 3		
Created based on [87]		Water	2000	g	Water, deionised, at plant/US* US- EI U US-EI		
		Electricity (autoclaving)	0.89	kWh	Electricity mix 2018/US U US-EI		The reference paper used 1.9 kWh for 3000 W, which means that the time of use was 0.63 h For the 1400 W autoclave chosen herein, the adjusted electricity input is 0.89 kWh
		Electricity (centrifuging)	0.57	kWh	Electricity mix 2018/US U US-EI		The reference paper used 5.59 MJ (1.55 kWh) for 600 W, which means that the time of use was 2.59 h For the 220 W centrifuge chosen herein, the adjusted electricity input is 0.57 kWh
Peptone (for 477 g)	Input	Soybean	40	g	Soybean {US}, production, APOS, U Ecoinvent 3		
Created based on [87]		Hexane	10	g	Hexane, at plant/US-US-EI U US-EI		

Table B.3. (continued)

		Sodium hydroxide	0.8	g	Sodium hydroxide, production mix, at plant/RNA USLCI		
		Enzymes	0.5	g	Enzymes {GLO}, market for enzymes, APOS, U Ecoinvent 3		
		Water	200	g	Water, deionised, at plant/US* US-EI U US-EI		
		Electricity (heating)	0.513	MJ	Electricity mix 2018/US U US-EI		
		Electricity (centrifuge)	0.11	kWh	Electricity mix 2018/US U US-EI		The reference paper used 0.3 kWh and assumed 3 times for 10 minutes each (600 W, 0.5 h) For the 220 W centrifuge chosen herein, the electricity input is 0.11 kWh

B.1.4 Chemical Exfoliation Synthesis of g-C_3N_4 Nanosheets

B.1.4.1 Synthesis procedure: Based on the work of Zhang *et al.*[89], ultrathin g-C_3N_4 nanosheets were obtained by liquid exfoliating of bulk g-C_3N_4 in water. In detail, 100 mg of bulk g-C_3N_4 powder were dispersed in 100 mL water, and then ultrasonicated for 16 hours. The suspension was then centrifuged at 5,000 rpm for 10 minutes (assumed) to remove the residual unexfoliated g-C_3N_4 nanoparticles and large-area nanosheets.

B.1.4.2 Synthesis Yield: The synthesis yield was not reported in the referenced paper. Thus, 100% yield was assumed to enable comparison with other methods. Bulk g-C_3N_4 was considered the limiting reagent.

B.1.4.3 LCI Details

LCI Inputs

i. 0.1 g of bulk g-C_3N_4

ii. 100 mL of water

iii. Electricity (ultrasonication): 16 h duration

- Assuming the Aquasonic 150 HT bath sonicator with power consumption of 400 W

Electricity (centrifugation): Considering 5,000 rpm for 10 minutes (time assumed since not reported)

- Assuming the Fisherbrand™ HORIZON™ 24 Clinical Centrifuge with power consumption of 220 W

Electricity consumed = Device power consumption (W) × time of use (h)

- Ultrasonication = 400 W × 16 h = 6.4 kWh
- Centrifugation = 220 W × 0.17 h = 0.037 kWh

Total = (6.4 + 0.037) kWh = 6.44 kWh

Table B.4. Life cycle inventory to produce g-C_3N_4 nanosheets by chemical exfoliation route, including the Pedigree matrix for the unit processes (all distributions assumed to be lognormal).

	Section	Material	Amount	Unit	LCI Database	Pedigree matrix SD^2	Comments
1 g of g-C_3N_4 nanosheets via chemical exfoliation route	Input	Bulk g-C_3N_4 from melamine	1	g	Created	1,4,3,1,1,na 1.15	Details shown in Table S1
Yield 100%		Water	1000	g	Water, deionised, at plant/US* US- EI U US-EI	1,4,3,1,1,na 1.15	1000 mL
		Electricity	6.44	kWh	Electricity mix 2018/US U US-EI	4,4,1,1,1,na 1.24	Used for ultrasonication, and centrifugation

B.1.5 Thermal Etching Synthesis of g-C_3N_4 Nanosheets

B.1.5.1 Synthesis procedure: Based on the work of Zhao *et al.*[36], bulk g-C_3N_4 was prepared by calcinating 5 g of melamine. After calcination, the bulk g-C_3N_4 was milled into powder and heated at 550 °C for 3 h with the heating rate of 5 °C min^{-1} to prepare the g-C_3N_4 nanosheets.

B.1.5.2 Synthesis Yield: The synthesis yield was not reported in the referenced paper. Thus, 100% yield was assumed to enable comparison with other methods. Bulk g-C_3N_4 was considered the limiting reagent.

B.1.5.3 LCI Details:

LCI Inputs

i. 3.65 g of bulk g-C_3N_4

Electricity (calcination): Calculated for a temperature of 550 °C for 3 h, when the heating speed is 5 °C min^{-1} (the heating speed was not informed; therefore, it was assumed to be the same as the one reported to produce their bulk g-C_3N_4)

- Assuming the Thermo Scientific Lindberg/Blue M TF55035A-1 tube furnace with power consumption of 800 W

Electricity input calculations:

Calculating total time of tube furnace turned on for heating:

Start temperature = 25 °C (room temperature)

Annealing temperature = 550 °C

Heating rate = 5 °C/min

Time to reach annealing temperature = (550 °C – 25 °C) / (5 °C/min) = 105 min = 1.75 h

Total time of furnace turned on = 1.75 h + 3 h = 4.75 h

Electricity consumed = Device power consumption (W) × time of use (h)

Total = 800 W × 4.75 h = 3.8 kWh

Table B.5. Life Cycle Inventory to produce 1 g of g-C_3N_4 nanosheets by thermal etching synthesis route, including the Pedigree matrix for the unit processes (all distributions assumed to be lognormal).

	Section	Material	Amount	Unit	LCI Database	Pedigree matrix SD^2	Comments
1 g of g-C_3N_4 nanosheets via thermal etching route	Input	Bulk g-C_3N_4 from melamine	1	g	Created	1,4,3,3,1,na 1.16	Details shown in Table S1
Yield 100%		Electricity	3.8	kWh	Electricity mix 2018/US U US-EI	4,4,1,1,1,na 1.24	Used for calcination

B.1.6 Direct Pyrolysis Synthesis of B-doped g-C_3N_4 Nanosheets from Melamine

B.1.6.1 Synthesis Procedure: Based on the work of Peng *et al*.[175] The boron-doped carbon nitride nanosheets were prepared by direct pyrolysis of the mixture of boric acid and melamine in a semi-closed system. In a typical approach, 3 g of melamine and 1.47 g of boric acid (with a molar ratio of 3:3) were dispersed in water and mixed to form a uniform white mixture. The well mixture was dried at 60 °C and then ground into powders with an agate mortar. The obtained mixture was placed in a crucible with a cover and then heated at 550 °C in air for 4 h with a heating rate of 5 °C min^{-1}. The obtained products were further rinsed with water to neutral and dried at 60 °C.

B.1.6.2 Synthesis Yield: The synthesis yield was not reported in the referenced paper. Thus, 100% yield was assumed to enable comparison with other methods. Melamine was considered the limiting reagent.

B.1.6.3 LCI Details:

LCI Inputs

i. 3 g melamine

ii. 1.47 g of boric acid

iii. 10 mL of water (assumed)

iv. Electricity (stirring): 3 h duration (assumed)

- Considering the Thermo Scientific™ SP88854100 stirring hot plate with power consumption of 540 W

Electricity (drying): 5 h duration (assumed)

- Assuming the Thermo Scientific™ SP88854100 stirring hot plate with power consumption of 540 W

Electricity (calcination): Calculated for a heating temperature of 550 °C for 4 h using a muffle furnace, when the heating rate is 5 °C min^{-1}

- Assuming the Thermo Scientific Lindberg/Blue M TF55035A-1 tube furnace with power consumption 800 W

v. 5 mL of water (assumed)

vi. Electricity (drying): 2.5 h duration (assumed)

Electricity input calculations:

Total time of muffle furnace turned on for heating:

Start temperature = 25 °C (room temperature)

Annealing temperature = 550 °C

Heating rate = 5 °C/min

Time to reach annealing temperature = (550 °C – 25 °C) / (5 °C/min) = 105 min

Total time of furnace turned on = 105 min + 4 h = 5.75 h

Electricity consumed = Device power consumption (W) × time of use (h)

- Stirring (stirring hot plate) = 540 W × 3 h = 1.62 kWh
- Drying (stirring hot plate) = 540 W × 5 h = 2.70 kWh
- Calcination (tube furnace) = 800 W × 5.75 h = 4.60 kWh
- Drying (stirring hot plate) = 540 W × 2.5 h = 1.35 kWh

Total = (1.62 + 2.70 + 4.60 + 1.35) kWh = 10.27 kWh

LCI Emissions to Air

i. 0.81 g of Ammonia.

ii. 15 g of Water.

Table B.6. Life cycle inventory to produce B-doped g-C_3N_4 nanosheets from melamine by direct pyrolysis including the Pedigree matrix for the unit processes (all distributions assumed to be lognormal).

	Section	Material	Amount	Unit	LCI Database	Pedigree matrix SD^2	Comments
1 g of g-C_3N_4 nanosheets	Input	Melamine	1.37	g	Melamine, at plant/US-US-EI U US-EI	1,4,2,3,1,na 1.12	
Yield 100%		Boric Acid	0.67	g	Boric acid, anhydrous, powder, at plant/US-US-EI U US-EI	1,4,2,3,1,na 1.12	
		Water	15	g	Water, deionised, at plant/US* US- EI U US-EI	4,4,2,3,1,na 1.24	
		Electricity	10.27	kWh	Electricity mix 2018/US U US-EI	4,4,1,1,1,na 1.24	Used for stirring, drying, and calcination
	Emission to air	Ammonia	0.37	g		2,4,5,1,1,na 1.53	Approximately 2 NH_3 liberated by melamine pyrolysis at 550 °C for 4h (mole/mole melamine). Based on [206] $C_3H_6N_6 \rightarrow$ g-C_3N_4 + 2 NH_3
		Water	15	g		4,4,2,3,1,na 1.24	Evaporation

B.1.7 Thermal Polymerization Synthesis of B-doped g-C_3N_4 Nanosheets from Urea

B.1.7.1 Synthesis Procedure: Based on the work of Yan *et al*.[174] A facile one-pot strategy is developed to synthesize porous B-doped g-C_3N_4 nanosheets using boric acid and urea as the precursors during thermal polymerization. The B-doped g-C_3N_4 are synthesized by heating boric acid (H_3BO_3) and urea ($CO(NH_2)_2$) as fuel in a muffle furnace. 20 g of $CO(NH_2)_2$ and appropriate H_3BO_3 with the grinding bowl grinding evenly was placed in crucible with a cover. The crucible is heated to 500 ℃ and hold for 2 h, then continued to heat the crucible to 550 ℃ and hold for 1 h. Then, the samples were cooled to room temperature. The synthesized samples are collected and ground into powders.

B.1.7.2 Synthesis Yield: The synthesis yield was not reported in the referenced paper. Thus, 100% yield was assumed to enable comparison with other methods. Urea was considered the limiting reagent.

B.1.7.3 LCI Details:

LCI Inputs

i. 20 g urea

ii. 0.1 g of boric acid

iii. Electricity (calcination): Calculated for a heating temperature of 500 °C for 2 h using a muffle furnace, when the heating rate is 5 °C min^{-1} (assumed)

Electricity (calcination): Calculated for a heating temperature of 550 °C for 1 h using a muffle furnace, when the heating rate is 5 °C min^{-1} (assumed)

- Assuming the Thermo Scientific™ BF51866C1 muffle furnace with power consumption of 1800 W

Electricity input calculations:

Calculating total time of furnace turned on for heating:

Start temperature = 25 °C (room temperature)

Annealing temperature = 500 °C

Heating rate = 5 °C/min

Time to reach annealing temperature = (500 °C – 25 °C) / (5 °C/min) = 95 min = 1.58h

Start temperature = 500 °C

Annealing temperature = 550 °C

Heating rate = 5 °C/min

Time to reach annealing temperature = (550 °C – 500 °C) / (5 °C/min) = 10 min = 0.17h

Total time of muffle furnace turned on = 1.58 h + 2 h + 0.17 h + 1 h = 4.75 h

Electricity consumed = Device power consumption (W) × time of use (h)

- Calcination (muffle furnace) = 1800 W × 4.75 h = 8.55 kWh

LCI Emissions to Air

i. 3.78 g of Ammonia

ii. 6 g of Water.

Table B.7. Life cycle inventory to produce B-doped g-C_3N_4 nanosheets from urea by thermal polymerization, including the Pedigree matrix for the unit processes (all distributions assumed to be lognormal).

	Section	Material	Amount	Unit	LCI Database	Pedigree matrix SD^2	Comments
1 g of g-C_3N_4 nanosheets	Input	Urea	0.90	g	Urea, as N, at regional storehouse/US- US-EI U US-EI	1,4,2,3,1,na 1.12	This LCI refers to 1 kg of N, resp. 2.17 kg urea with a N-content of 46%. Thus, to account for the 1.96 g of urea needed, the amount of 0.90 g is used
Yield 100%		Boric Acid	0.01	g	Boric acid, anhydrous, powder, at plant/US- US-EI US-EI	2,4,2,3,1,na 1.13	
		Electricity	8.55	kWh	Electricity mix 2018/US U US-EI	4,4,1,1,1,na 1.24	Used for calcination
	Emission to air	Ammonia	0.37	g		2,4,4,3,1,na 1.24	Based on [207,212] $CH_4N_2O \rightarrow$ g-C_3N_4 + 2 NH_3 + 3 H_2O
		Water	0.59	g		2,4,4,3,1,na 1.24	Based on [207,212] $CH_4N_2O \rightarrow$ g-C_3N_4 + 2 NH_3 + 3 H_2O

B.1.8 Two-step Calcination Synthesis of C-doped g-C_3N_4 Nanosheets

B.1.8.1 Synthesis Procedure:

B.1.8.2 Based on the work of Xiao *et al.*[72], 100 mg of the bulk g-C_3N_4 powder and 200 mg of glucose were added to 50 mL of distilled water and vigorously stirred for 12 h to obtain a homogeneous suspension. The mixture was dried at 80 ℃ overnight, and then placed in a crucible with a cover. The crucible was heated to 450 ℃ at a 5 ℃ min^{-1} heating rate in a tube furnace for 2 h in air.

B.1.8.3 Synthesis Yield: The synthesis yield was not reported in the referenced paper. Thus, 100% yield was assumed to enable comparison with other methods. Bulk g-C_3N_4 was considered the limiting reagent.

B.1.8.4 LCI Details:

LCI Inputs

i. 100 g of bulk g-C_3N_4

ii. 200 g of glucose

iii. 50 mL of water

iv. Electricity (stirring): 12 h duration

- Considering the Thermo Scientific™ SP88854100 stirring hot plate with power consumption of 540 W

Electricity (drying): 12 h duration (assumed to reflect overnight)

- Assuming the Thermo Scientific™ SP88854100 stirring hot plate with power consumption of 540 W

Electricity (calcination): Calculated for a heating temperature of 450 °C for 2 h using a tube furnace, when the heating rate is 5 °C min^{-1}

- Assuming the Thermo Scientific Lindberg/Blue M TF55035A-1 tube furnace with power consumption of 800 W

Electricity input calculations:

Calculating total time of tube furnace turned on for heating:

Start temperature = 25 °C (room temperature)

Annealing temperature = 450 °C

Heating rate = 5 °C/min

Time to reach annealing temperature = (450 °C – 25 °C) / (5 °C/min) = 85 min

Total time of furnace turned on = 85 min + 2 h = 3.42 h

Electricity consumed = Device power consumption (W) × time of use (h)

- Stirring (stirring hot plate) = 540 W × 12 h = 6.48 kWh\
- Drying (stirring hot plate) = 540 W × 12 h = 6.48 kWh
- Calcination (tube furnace) = 800 W × 3.42 h = 2.74 kWh

Total = (6.48 + 6.48 + 2.74) kWh = 15.7 kWh

LCI Emissions to Air

i. 50 g of Water.

Table B.8. Life cycle inventory to produce C-doped g-C_3N_4 nanosheets by two-step calcination, including the Pedigree matrix for the unit processes (all distributions assumed to be lognormal).

	Section	Material	Amount	Unit	LCI Database	Pedigree matrix SD^2	Comments
1 g of g-C_3N_4 nanosheets	Input	Bulk g-C_3N_4	1	g	Created	1,4,2,3,1,na 1.12	Details shown in Table S1
Yield 100%		Glucose	2	g	Glucose {GLO}, market for glucose, APOS U Ecoinvent 3	1,4,2,3,1,na 1.12	
		Water	0.5	g	Water, deionised, at plant/US* US- EI U US-EI	1,4,2,3,1,na 1.12	
		Electricity	15.7	kWh	Electricity mix 2018/US U US-EI	4,4,1,1,1,na 1.24	Used for stirring, drying, and calcination
	Emission to air	Water	0.5	g		1,4,2,3,1,na 1.12	Evaporation

B.1.9 Synthesis of O-doped g-C_3N_4 Nanosheets

B.1.9.1 Synthesis Procedure: Based on the work of Huang *et al*.[176], porous O-doped g-C_3N_4 was synthesized by mixing melamine (0.15g) with hydrogen peroxide (30 vol%, 5.2 or 10.4 mL) and stirring for 10 min at 60 ℃. The mixture was then separated via centrifugation, washed 3 times with high purity water and ethanol, and dried at 40 ℃ overnight. Finally, the mixture was ground into powder and calcined at 550 ℃ for 2 h with a heating rate of 5.0 ℃/min in N_2 atmosphere. Sample using 5.2 mL of H_2O_2 has higher photocatalytic activity.

B.1.9.2 Synthesis Yield: The synthesis yield was not reported in the referenced paper. Thus, 100% yield was assumed to enable comparison with other methods. Melamine was considered the limiting reagent.

B.1.9.3 LCI Details:

LCI Inputs

i. 0.15 g melamine

ii. 5.2 mL hydrogen peroxide 30%, which is equal 3.46 g of hydrogen peroxide 50% plus 2.14 g of water

iii. Electricity (stirring): 10 minutes

- Considering the Thermo Scientific™ SP88854100 stirring hot plate with power consumption of 540 W

Electricity (centrifugation): 30 minutes (assumed 10 minutes each time since time is not reported).

- Assuming the Fisherbrand™ HORIZON™ 24 Clinical Centrifuge with power consumption of 220 W

iv. 15 mL of water (assumed)

v. 15 mL of ethanol (assumed), which is equal 11.84 g of ethanol (density of 0.789 g/mL).

vi. Electricity (drying): 12 h duration (assumed)

- Assuming the Thermo Scientific™ SP88854100 stirring hot plate with power consumption of 540 W

Electricity (calcination): Calculated for a heating temperature of 550 °C for 2 h using a tube furnace, when the heating rate is 5 °C min^{-1}

- Assuming the Thermo Scientific Lindberg/Blue M TF55035A-1 tube furnace with power consumption of 800 W

vii. Nitrogen gas: assuming flow of 100 mL/min, and temperature of 21 ℃.

- 100 mL/min × 3.75 h = 22.5 L of N_2. Mass = 22.5 L × 1.16 kg/m^3 × 1 m^3/1000 L = 0.0261 kg = 26.1 g

Electricity input calculations:

Calculating total time of tube furnace turned on for heating:

Start temperature = 25 °C (room temperature)

Annealing temperature = 550 °C

Heating rate = 5 °C/min

Time to reach annealing temperature = (550 °C – 25 °C) / (5 °C/min) = 105 min

Total time of furnace turned on = 1.75 h + 2 h = 3.75 h

Electricity consumed = Device power consumption (W) × time of use (h)

- Stirring (stirring hot plate) = 540 W × 0.17 h = 0.0918 kWh
- Centrifugation (centrifuge) = 220 W × 0.25 h = 0.055 kWh
- Drying (stirring hot plate) = 540 W × 12 h = 6.48 kWh
- Calcination (tube furnace) = 800 W × 3.75 h = 3.0 kWh

Total = (0.0918 + 0.055 + 6.48 + 3.0) kWh = 9.63 kWh

LCI Emissions to Air

i. 0.042 g of Ammonia

ii. 15 g of Water

iii. 11.84 g of Ethanol

iv. 26.1 g of Nitrogen

Table B.9. Life cycle inventory to produce O-doped g-C_3N_4 nanosheets, including the Pedigree matrix for the unit processes (all distributions assumed to be lognormal).

	Section	Material	Amount	Unit	LCI Database	Pedigree matrix SD^2	Comments
1 g of g-C_3N_4 nanosheets	Input	Melamine	1.36	g	Melamine, at plant/US- US-EI U US-EI	1,4,3,3,1,na 1.16	
Yield 100%		Hydrogen peroxide	31.37	g	Hydrogen peroxide, 50% in H2O, at plant/US- US-EI U US-EI	1,4,3,3,1,na 1.16	
		Water	19.40	g	Water, deionised, at plant/US* US- EI U US-EI	4,4,3,3,1,na 1.26	Dilution
		Water	15	g	Water, deionised, at plant/US* US- EI U US-EI	4,4,3,3,1,na 1.26	Washing
		Ethanol	11.84	g	Ethanol from ethylene, at plant/US- US-EI U US-EI	4,4,3,3,1,na 1.26	Washing
		Nitrogen gas	26.10	g	Nitrogen, liquid, at plant/US- US-EI U US-EI	2,4,1,1,1,na 1.12	Calcination inert gas
		Electricity	9.63	kWh	Electricity mix 2018/US U US-EI	4,4,1,1,1,na 1.24	Used for stirring, centrifugation, drying, and calcination
	Emission to air	Ammonia	0.38	g		2,4,5,1,1,na 1.53	Approximately 2 NH_3 liberated by melamine pyrolysis at 550 °C for 2 h (mole/mole melamine). Based on [206]

Table B.9. (continued)

		Water	15	g		4,4,3,3,1,na 1.26	Evaporation
		Ethanol	11.84	g		4,4,3,3,1,na 1.26	Evaporation
		Nitrogen	26.1	g		2,4,1,1,1,na 1.12	Calcination inert gas

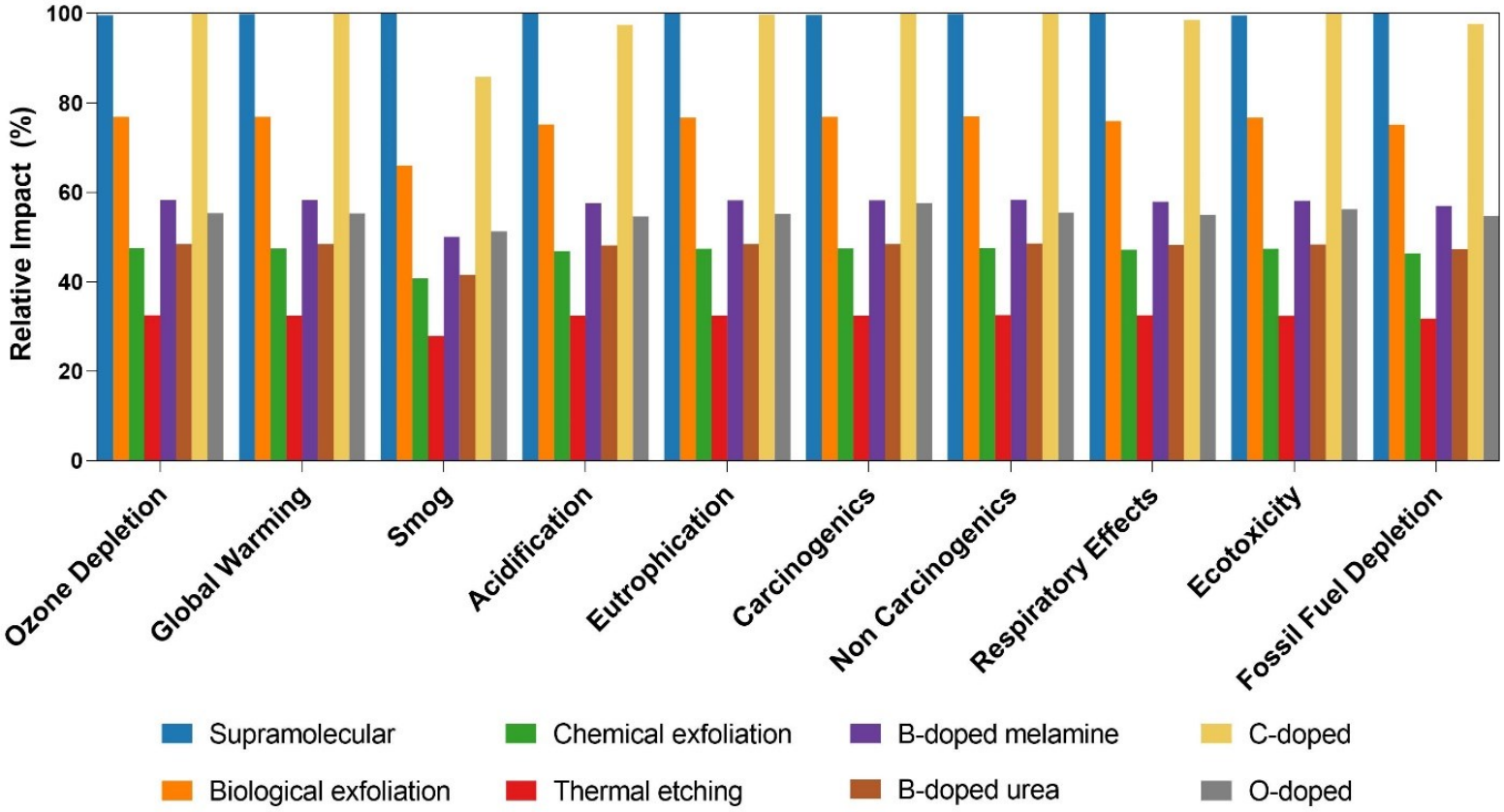

Figure B.1. Relative environmental impacts of eight g-C_3N_4 synthesis routes to produce 1 g of g-C_3N_4 nanosheets, using TRACI 2.1 life cycle impact assessment method. The trends and magnitudes of impacts are similar for all impact categories. Relative impacts are normalized to the highest value in each category.

Table B.10. Absolute values of environmental impacts to produce 1 g of g-C_3N_4 nanosheets by the eight synthesis routes assuming 100% yield (CTU: Comparative Toxic Unit, h: for humans, e: for ecosystems, eq: equivalents).

Impact category	Unit	**Supra molecular**	**Biological exfoliation**	**Chemical exfoliation**	**Thermal etching**	**B-doped melamine**	**B-doped urea**	**C-doped**	**O-doped**
Ozone Depletion	kg CFC-11 eq	4.37E-07	3.37E-07	2.09E-07	1.43E-07	2.56E-07	2.13E-07	4.39E-07	2.43E-07
Global Warming	kg CO_2 eq	1.08E+01	8.32E+00	5.14E+00	3.52E+00	6.30E+00	5.25E+00	1.08E+01	5.98E+00
Smog	kg O_3 eq	4.68E-01	3.09E-01	1.91E-01	1.31E-01	2.34E-01	1.95E-01	4.02E-01	2.40E-01
Acidification	kg SO_2 eq	4.71E-02	3.54E-02	2.21E-02	1.53E-02	2.71E-02	2.27E-02	4.59E-02	2.57E-02
Eutrophication	kg N eq	2.38E-02	1.82E-02	1.13E-02	7.73E-03	1.38E-02	1.15E-02	2.37E-02	1.31E-02
Carcinogenics	CTUh	3.97E-07	3.06E-07	1.89E-07	1.29E-07	2.32E-07	1.93E-07	3.98E-07	2.29E-07
Non Carcinogenics	CTUh	1.39E-06	1.07E-06	6.60E-07	4.52E-07	8.10E-07	6.73E-07	1.39E-06	7.70E-07
Respiratory Effects	kg $PM_{2.5}$ eq	2.85E-03	2.17E-03	1.35E-03	9.29E-04	1.65E-03	1.38E-03	2.81E-03	1.57E-03
Ecotoxicity	CTUe	3.14E+01	2.42E+01	1.50E+01	1.02E+01	1.84E+01	1.53E+01	3.16E+01	1.78E+01
Fossil Fuel Depletion	MJ surplus	1.27E+01	9.58E+00	5.92E+00	4.05E+00	7.26E+00	6.04E+00	1.25E+01	6.98E+00

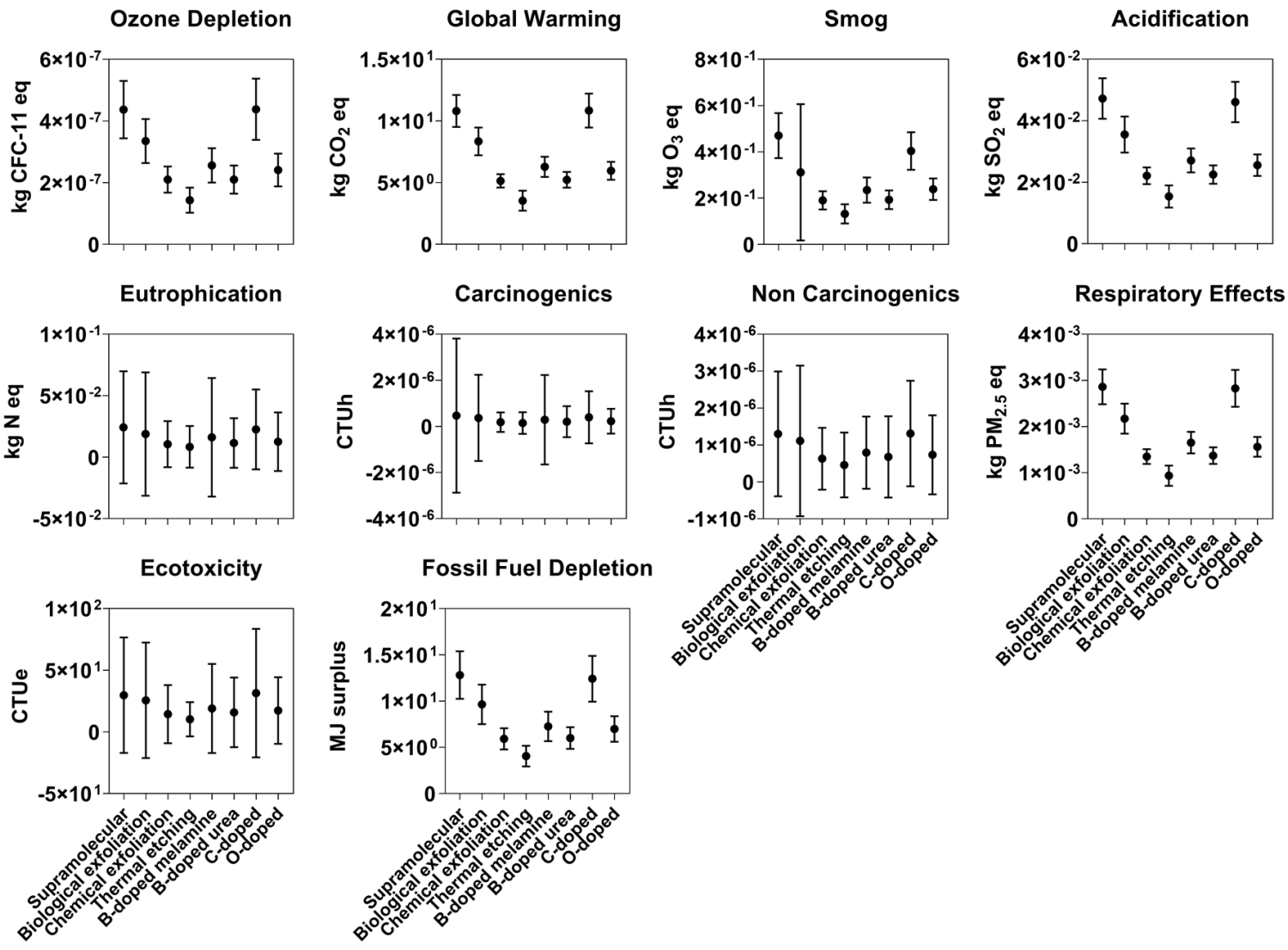

Figure B.2. The mean impact and the associated uncertainty for each synthesis route in all assessed impact categories. Error bars represent 95% confidence intervals for the uncertainties in the unit processes and are calculated using a Monte Carlo approach.

Table B.11. Absolute values of environmental impacts associated with electricity when varying calcination parameters (CTU: Comparative Toxic Unit, h: for humans, e: for ecosystems, eq: equivalents).

Impact category	Unit	2.3 °C/min, 2 h, 520 °C	15 °C/min, 2 h, 520 °C	2 h, 5 °C/min, 520 °C	4 h, 5 °C/min, 520 °C	520 °C, 2 h, 5 °C/min	600 °C, 2 h, 5 °C/min
Ozone Depletion	kg CFC-11 eq	1.11E-07	5.07E-08	7.25E-08	1.12E-07	7.25E-08	7.79E-08
Global Warming	kg CO_2 eq	2.74E+00	1.25E+00	1.79E+00	2.77E+00	1.79E+00	1.92E+00
Smog	kg O_3 eq	1.02E-01	4.65E-02	6.65E-02	1.03E-01	6.65E-02	7.15E-02
Acidification	kg SO_2 eq	1.15E-02	5.24E-03	7.50E-03	1.16E-02	7.50E-03	8.06E-03
Eutrophication	kg N eq	6.00E-03	2.74E-03	3.92E-03	6.07E-03	3.92E-03	4.21E-03
Carcinogenics	CTUh	1.01E-07	4.60E-08	6.59E-08	1.02E-07	6.59E-08	7.07E-08
Non Carcinogenics	CTUh	3.52E-07	1.61E-07	2.30E-07	3.56E-07	2.30E-07	2.47E-07
Respiratory Effects	kg $PM_{2.5}$ eq	7.07E-04	3.22E-04	4.61E-04	7.14E-04	4.61E-04	4.96E-04
Ecotoxicity	CTUe	7.98E+00	3.64E+00	5.21E+00	8.07E+00	5.21E+00	5.60E+00
Fossil Fuel Depletion	MJ surplus	3.15E+00	1.44E+00	2.06E+00	3.19E+00	2.06E+00	2.21E+00

Table B.12. Absolute values of environmental impacts to produce 1 g of g-C_3N_4 nanosheets by eight synthesis routes assuming 100% yield, and considering a cleaner electricity grid mix (CTU: Comparative Toxic Unit, h: for humans, e: for ecosystems, eq: equivalents).

Impact category	Unit	Supra molecular	Biological exfoliation	Chemical exfoliation	Thermal etching	B-doped melamine	B-doped urea	C-doped	O-doped
Ozone Depletion	kg CFC-11 eq	2.93E-08	2.14E-08	1.37E-08	9.27E-09	1.63E-08	1.33E-08	2.78E-08	1.86E-08
Global Warming	kg CO_2 eq	2.45E+00	1.84E+00	1.14E+00	7.82E-01	1.40E+00	1.16E+00	2.39E+00	1.38E+00
Smog	kg O_3 eq	2.48E-01	1.39E-01	8.57E-02	5.87E-02	1.05E-01	8.74E-02	1.80E-01	1.19E-01
Acidification	kg SO_2 eq	2.31E-02	1.68E-02	1.06E-02	7.45E-03	1.31E-02	1.10E-02	2.17E-02	1.25E-02
Eutrophication	kg N eq	1.33E-03	8.66E-04	5.51E-04	3.89E-04	6.72E-04	5.61E-04	1.12E-03	7.76E-04
Carcinogenics	CTUh	4.75E-08	3.53E-08	2.19E-08	1.50E-08	2.68E-08	2.22E-08	4.60E-08	3.69E-08
Non Carcinogenics	CTUh	3.01E-07	2.28E-07	1.41E-07	9.68E-08	1.73E-07	1.43E-07	2.94E-07	1.73E-07
Respiratory Effects	kg $PM_{2.5}$ eq	1.37E-03	1.02E-03	6.35E-04	4.42E-04	7.81E-04	6.51E-04	1.31E-03	7.51E-04
Ecotoxicity	CTUe	7.78E+00	5.90E+00	3.65E+00	2.50E+00	4.47E+00	3.70E+00	7.72E+00	4.74E+00
Fossil Fuel Depletion	MJ surplus	6.12E+00	4.45E+00	2.75E+00	1.89E+00	3.38E+00	2.80E+00	5.78E+00	3.34E+00

Table B.13. Percent reduction in environmental impacts to produce 1 g of g-C_3N_4 nanosheets when considering a cleaner electricity grid mix compared to the 2018 country mix from SimaPro.

Impact category	Supramolecular	Biological exfoliation	Chemical exfoliation	Thermal etching	B-doped melamine	B-doped urea	C-doped	O-doped
Ozone Depletion	93	94	93	93	94	94	94	92
Global Warming	77	78	78	78	78	78	78	77
Smog	47	55	55	55	55	55	55	50
Acidification	51	52	52	51	52	52	53	51
Eutrophication	94	95	95	95	95	95	95	94
Carcinogenics	88	88	88	88	88	89	88	84
Non Carcinogenics	78	79	79	79	79	79	79	77
Respiratory Effects	52	53	53	52	53	53	53	52
Ecotoxicity	75	76	76	76	76	76	76	73
Fossil Fuel Depletion	52	54	53	53	54	54	54	52

B.2 Environmental Impacts Associated with Scaled Up Scenarios

B.2.1 Scaling up the g-C_3N_4 Production from 1 g to 1 kg

The synthesis procedures are detailed in section 1 on a per gram basis. To synthesize 1 kg of g-C_3N_4, a higher capacity muffle furnace was considered, and all other equipment necessary for the syntheses remained the same (i.e., the power consumption was only modified for the calcination step, which is the most energy intensive). Additionally, all precursors, reagents and emissions were linearly scaled to produce 1 kg of g-C_3N_4 (i.e., × 1000).

- Assuming the Thermo Scientific™ BF51842PBFMC1 muffle furnace (capacity of 55.3 L) with power consumption of 5800 W
- Assuming the Chemglass Life Sciences CGQ400004 quartz crucible of 100 mL, it would be possible to fit 60 crucibles within the muffle furnace, totaling a volume of 6 L
- According to our experimental data, a 10 mL crucible holds about 2.5 g of g-C_3N_4 precursors. Thus, 6 L of crucible volume can hold 1.5 kg of g-C_3N_4 precursors, which means this muffle furnace could be used to make 1 kg of g- C_3N_4 by all synthesis routes.
- Electricity consumed = Device power consumption (W) × time of use (h)

B.2.1.1 Electricity Demand for Bulk g-C_3N_4

- Calcination (higher capacity muffle furnace) = 5800 W × 3.65 h = 21.17 kWh

B.2.1.2 Electricity Demand for Supramolecular

- Stirring = 540 W × 3 h = 1.62 kWh

- Bath sonication = 400 W × 1 h = 0.4 kWh
- Drying = 540 W × 16 h = 8.64 kWh
- Calcination (higher capacity muffle furnace) = 5800 W × 7.8 h = 45.24 kWh

  Total = (1.62 + 0.4 + 8.64 + 45.24) kWh = 55.9 kWh

Note: The helium gas input is not included because an air atmosphere is assumed for the reaction in the muffle furnace.

B.2.1.3 Electricity Demand for Biological Exfoliation

- Incubation = 300 W × 4 h = 1.2 kWh
- Centrifugation = 220 W × 0.17 h = 0.037 kWh
- Calcination (higher capacity muffle furnace) = 5800 W × 5.75 h = 33.35 kWh

  Total = (1.2 + 0.037 + 33.35) kWh = 34.59 kWh

B.2.1.4 Electricity Demand for Chemical Exfoliation

- Ultrasonication = 400 W × 16 h = 6.4 kWh
- Centrifugation = 220 W × 0.17 h = 0.037 kWh

  Total = (6.4 + 0.037) kWh = 6.44 kWh

B.2.1.5 Electricity Demand for Thermal Etching

- Calcination (higher capacity muffle furnace) = 5800 W × 4.75 h = 27.55 kWh

  Total = 27.55 kWh

B.2.1.6 Electricity Demand for B-doped from Melamine

- Stirring = 540 W × 3 h = 1.62 kWh
- Drying = 540 W × 5 h = 2.70 kWh
- Calcination (higher capacity muffle furnace) = 5800 W × 5.75 h = 33.35 kWh
- Drying = 540 W × 2.5 h = 1.35 kWh

Total = (1.62 + 2.70 + 33.35 + 1.35) kWh = 39.02 kWh

B.2.1.7 Electricity Demand for B-doped from Urea

- Calcination (higher capacity muffle furnace) = 5800 W × 4.75 h = 27.55 kWh

Total = 27.55 kWh

B.2.1.8 Electricity Demand for C-doped

- Stirring = 540 W × 12 h = 6.48 kWh
- Drying = 540 W × 12 h = 6.48 kWh
- Calcination (higher capacity muffle furnace) = 5800 W × 3.42 h = 19.84 kWh

Total = (6.48 + 6.48 + 19.84) kWh = 32.80 kWh

B.2.1.9 Electricity Demand for O-doped

- Stirring = 540 W × 0.17 h = 0.0918 kWh
- Centrifugation = 220 W × 0.25 h = 0.055 kWh
- Drying = 540 W × 12 h = 6.48 kWh
- Calcination (higher capacity muffle furnace) = 5800 W × 3.75 h = 21.75 kWh

Total = (0.0918 + 0.055 + 6.48 + 21.75) kWh = 28.38 kWh

Note: The nitrogen gas input is not included because an air atmosphere is assumed for the reaction in the muffle furnace.

Table B.14. Absolute values of environmental impacts for each nano-TiO_2 synthesis when producing 1 kg, based on the study of Wu et al.,[87] and when scaling down the production to 1 g (CTU: Comparative Toxic Unit, h: for humans, e: for ecosystems, eq: equivalents).

		Sol-gel		Radio frequency thermal plasma	
Impact category	**Unit**	**1 kg**	**1 g**	**1 kg**	**1 g**
Ozone depletion	kg CFC-11 eq	2.04E-06	1.29E-07	3.40E-05	3.09E-05
Global warming	kg CO_2 eq	3.27E+01	3.15E+00	8.23E+02	7.70E+02
Smog	kg O_3 eq	1.55E+00	1.18E-01	3.11E+01	2.89E+01
Acidification	kg SO_2 eq	1.32E-01	1.32E-02	3.47E+00	3.26E+00
Eutrophication	kg N eq	1.35E-01	6.97E-03	1.86E+00	1.73E+00
Carcinogenics	CTUh	1.05E-06	1.16E-07	3.10E-05	2.94E-05
Non carcinogenics	CTUh	3.74E-06	4.05E-07	1.08E-04	1.02E-04
Respiratory effects	kg $PM_{2.5}$ eq	1.55E-02	8.20E-04	2.21E-01	1.98E-01
Ecotoxicity	CTUe	1.88E+02	9.27E+00	2.59E+03	2.34E+03
Fossil fuel depletion	MJ surplus	1.08E+02	3.70E+00	1.07E+03	8.70E+02

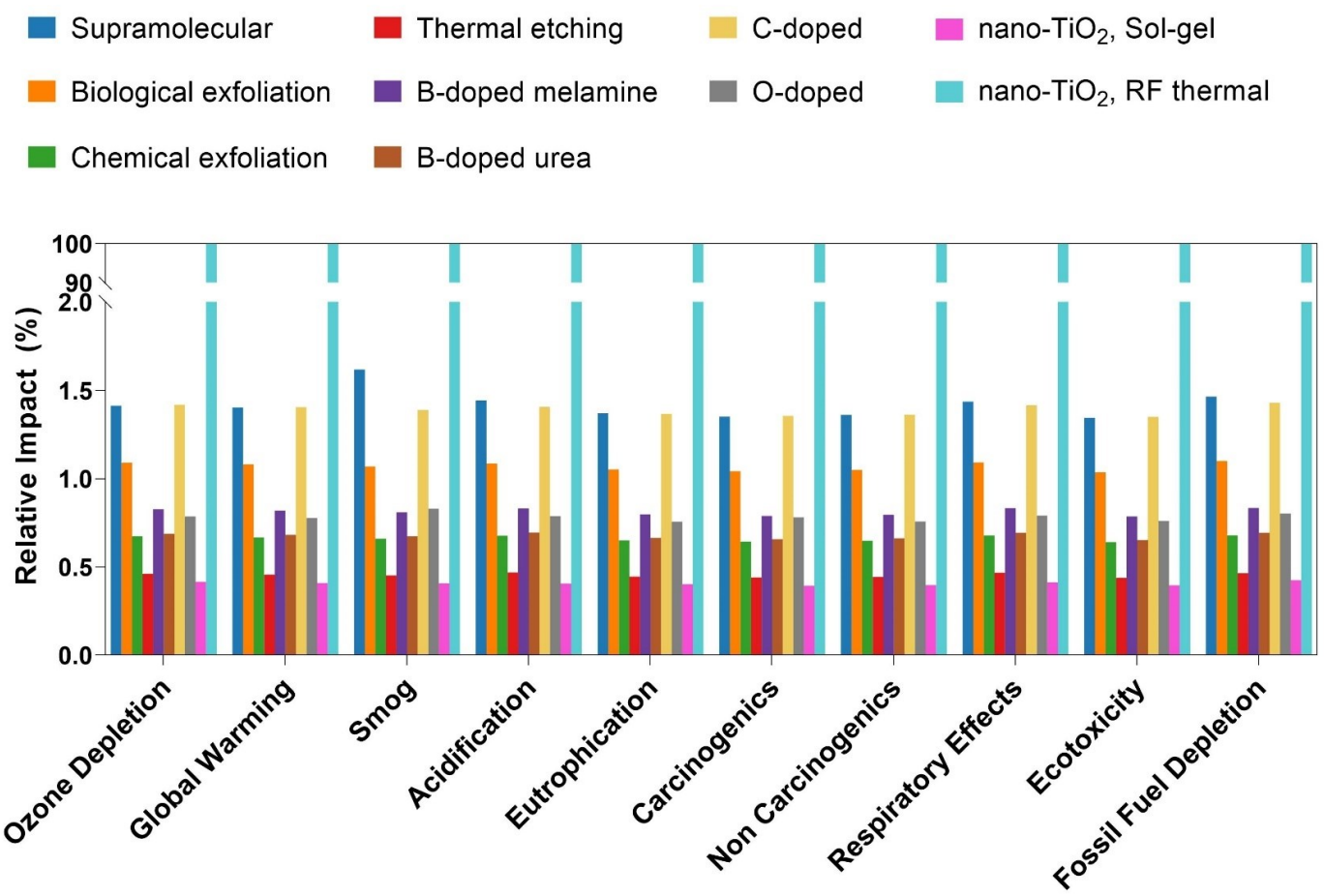

Figure B.3. Relative environmental impacts for producing 1 g of g-C_3N_4 nanosheets and nano-TiO_2 by different synthesis routes. Relative impacts are normalized to the highest value in each category. The relative impact values for nano-TiO2 syntheses were obtained based on the life cycle inventory reported by Wu et al.,87 assuming the same electricity input and materials necessary for the equipment functioning when scaling down the functional unit from kg to g. Precursors and reagents were linearly scaled (i.e., ÷ 1000). RF thermal = radio frequency thermal plasma

Table B.15. Absolute values of environmental impacts for producing 1 kg of g-C_3N_4 nanosheets by each synthesis route when scaling up the g-C_3N_4 nanosheets production from 1 g to 1 kg (CTU: Comparative Toxic Unit, h: for humans, e: for ecosystems, eq: equivalents).

Impact category	Unit	Supramolecular	Biological exfoliation	Chemical exfoliation	Thermal etching
Ozone depletion	kg CFC-11 eq	1.79E-05	2.95E-06	1.58E-06	1.71E-06
Global warming	kg CO_2 eq	4.68E+02	6.73E+01	2.61E+01	3.78E+01
Smog	kg O_3 eq	8.40E+01	2.44E+00	9.16E-01	1.34E+00
Acidification	kg SO_2 eq	3.77E+00	9.83E-01	8.08E-01	8.57E-01
Eutrophication	kg N eq	1.15E+00	1.88E-01	9.42E-02	1.19E-01
Carcinogenics	CTUh	1.67E-05	2.43E-06	9.50E-07	1.33E-06
Non carcinogenics	CTUh	5.96E-05	8.94E-06	3.85E-06	5.10E-06
Respiratory effects	kg $PM_{2.5}$ eq	1.89E-01	4.49E-02	3.38E-02	3.68E-02
Ecotoxicity	CTUe	1.37E+03	2.13E+02	8.50E+01	1.16E+02
Fossil fuel depletion	MJ surplus	7.95E+02	8.52E+01	3.82E+01	5.18E+01
Impact category	**Unit**	**B-doped melamine**	**B-doped urea**	**C-doped**	**O-doped**
Ozone depletion	kg CFC-11 eq	1.52E-06	9.02E-07	4.94E-05	3.92E-06
Global warming	kg CO_2 eq	3.25E+01	2.03E+01	1.21E+03	8.16E+01
Smog	kg O_3 eq	1.17E+00	7.16E-01	4.50E+01	2.09E+01
Acidification	kg SO_2 eq	8.44E-01	7.80E-01	5.64E+00	9.97E-01
Eutrophication	kg N eq	1.08E-01	8.47E-02	2.69E+00	2.00E-01
Carcinogenics	CTUh	1.15E-06	7.07E-07	4.45E-05	1.21E-05
Non carcinogenics	CTUh	4.52E-06	2.66E-06	1.53E-04	1.27E-05
Respiratory effects	kg $PM_{2.5}$ eq	3.67E-02	3.09E-02	3.36E-01	4.84E-02
Ecotoxicity	CTUe	1.03E+02	6.04E+01	3.60E+03	5.85E+02
Fossil fuel depletion	MJ surplus	4.59E+01	2.71E+01	1.40E+03	1.97E+02

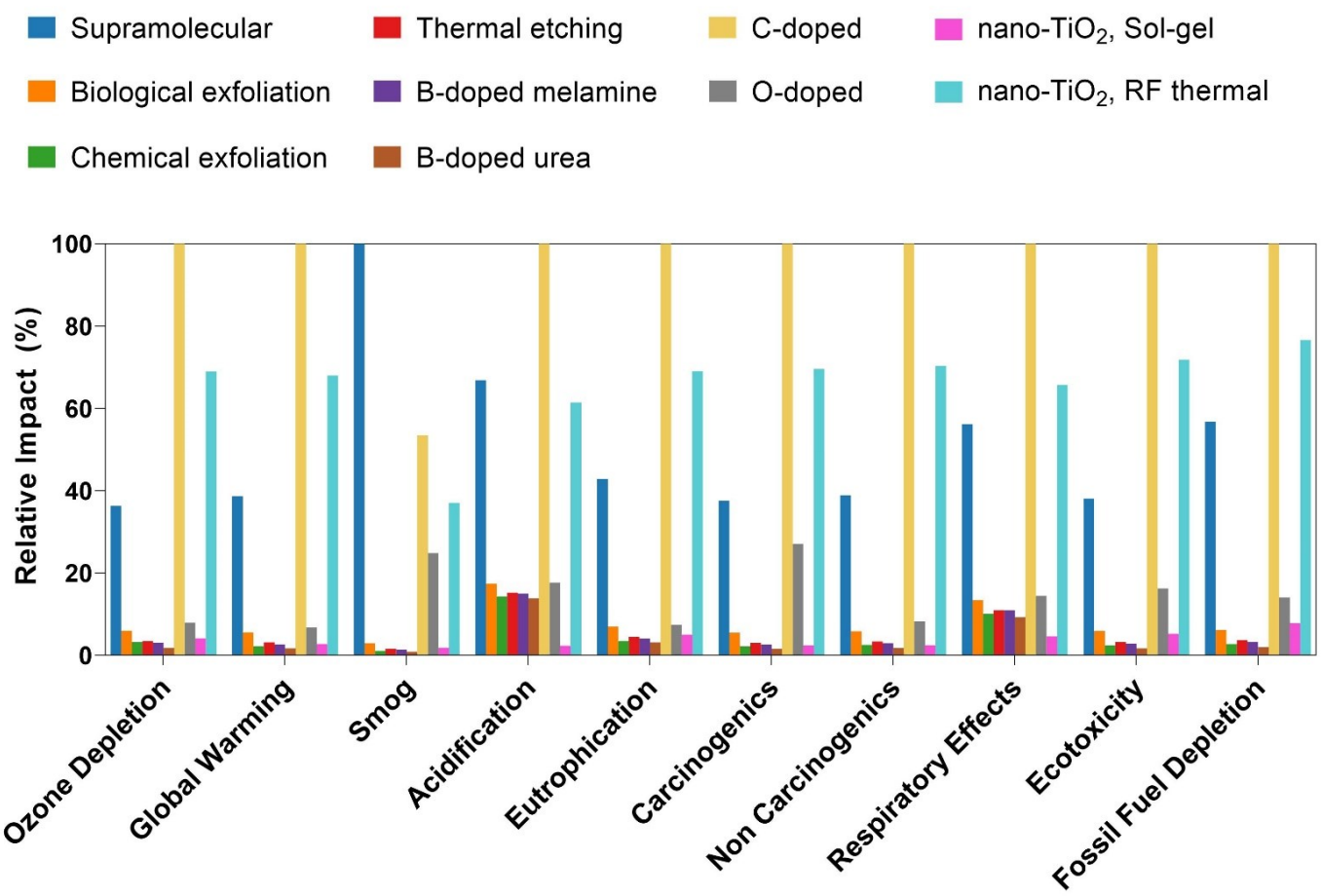

Figure B.4. Relative environmental impacts for producing 1 kg of g-C_3N_4 nanosheets and nano-TiO_2 by different synthesis routes. The relative impact values for nano-TiO_2 syntheses were obtained based on the life cycle inventory reported by Wu *et al.*[87] The g-C_3N_4 nanosheet syntheses were scaled up from 1 g to 1 kg assuming a higher capacity muffle furnace while all other equipment necessary for the syntheses remained the same. Precursors, reagents, and emissions were linearly scaled (i.e., multiplied by 1000). RF thermal = radio frequency thermal plasma

Table B.16. Absolute values of environmental impacts for producing 1 kg of g-C_3N_4 nanosheets and nano-TiO_2 precursors (CTU: Comparative Toxic Unit, h: for humans, e: for ecosystems, eq: equivalents).

Impact category	Unit	Melamine	Urea	Cyanamide	TTIP	TTBO
Ozone depletion	kg CFC-11 eq	3.66E-07	1.11E-07	1.20E-06	5.27E-07	4.60E-07
Global warming	kg CO_2 eq	5.82E+00	1.74E+00	4.26E+01	7.89E+00	7.54E+00
Smog	kg O_3 eq	1.66E-01	4.45E-02	1.23E+00	3.86E-01	3.51E-01
Acidification	kg SO_2 eq	2.62E-02	6.85E-03	1.76E-01	3.17E-02	2.90E-02
Eutrophication	kg N eq	7.43E-03	1.95E-03	4.43E-02	3.27E-02	1.59E-02
Carcinogenics	CTUh	1.71E-07	4.37E-08	1.03E-06	2.51E-07	2.37E-07
Non carcinogenics	CTUh	9.24E-07	2.49E-07	4.42E-06	8.99E-07	8.26E-07
Respiratory effects	kg $PM_{2.5}$ eq	3.21E-03	9.67E-04	1.63E-02	4.00E-03	3.61E-03
Ecotoxicity	CTUe	2.12E+01	5.73E+00	1.45E+02	4.92E+01	4.34E+01
Fossil fuel depletion	MJ surplus	1.27E+01	3.93E+00	1.23E+02	2.76E+01	3.23E+01

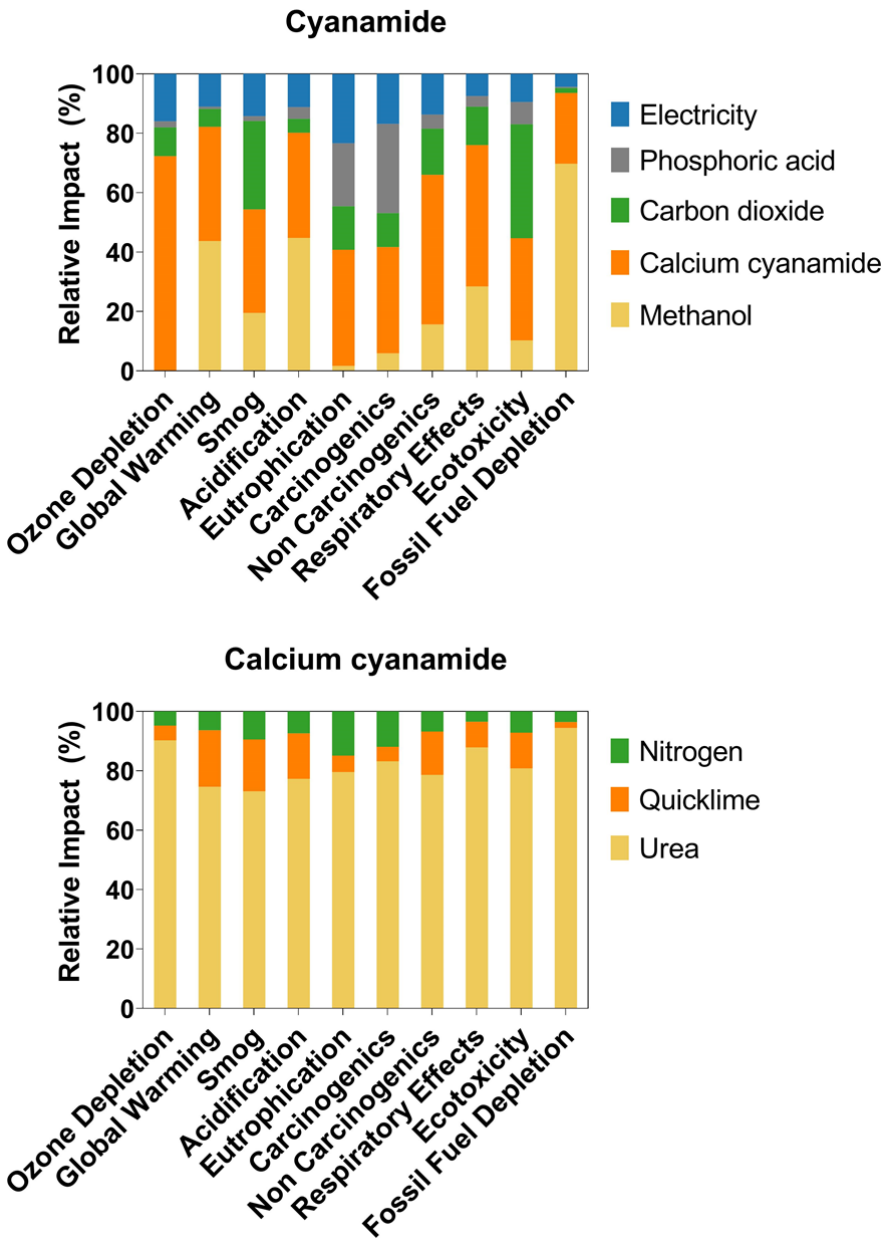

Figure B.5. Process contributions associated with the ten TRACI mid-point impact categories to produce 1 kg of cyanamide and 1 kg of calcium cyanamide.

Table B.17. Life cycle inventory to produce cyanamide, including the Pedigree matrix for the unit processes (all distributions assumed to be lognormal).

	Section	Material	Amount	Unit	LCI Database	Pedigree matrix SD^2
Cyanamide (for 639.2 g)	Input	Methanol	9.516	kg	Methanol, at plant/RNA USLCI	1,4,5,3,1,na 1.52
Yield 100%		Calcium cyanamide	2	kg	Created	1,4,5,3,1,na 1.52
		Carbon dioxide	1.98	kg	Carbon dioxide, liquid {RoW}| production | APOS, U Ecoinvent 3	1,4,5,3,1,na 1.52
		Phosphoric acid	0.129	kg	Phosphoric acid, industrial grade, 85% in H2O, at plant/US- US-EI U US-EI	1,4,5,3,1,na 1.52
		Electricity	4.93	kWh	Electricity mix 2018/US U US-EI	4,4,1,1,1,na 1.24
Calcium cyanamide (for 80.102 kg)	Input	Urea	83.027	kg	Urea, as N, at regional storehouse/US- US-EI U US-EI	1,4,5,1,1,na 1.52
		Quicklime	56.077	kg	Quicklime, at plant NREL/US U US-EI	1,4,5,1,1,na 1.52
		Nitrogen	48.24	kg	Nitrogen, liquid, at plant/US- US-EI U US-EI	4,4,5,1,1,na 1.58

Table B.18. Absolute values of environmental impacts for disinfecting 1 m^3 of drinking water by UV light with a dose of 186 mJ/cm^2 (CTU: Comparative Toxic Unit, h: for humans, e: for ecosystems, eq: equivalents).

Impact category	Unit	UV disinfection
Ozone Depletion	kg CFC-11 eq	6.01E-08
Global Warming	kg CO_2 eq	1.01E+00
Smog	kg O_3 eq	5.71E-02
Acidification	kg SO_2 eq	4.89E-03
Eutrophication	kg N eq	2.62E-03
Carcinogenics	CTUh	5.51E-07
Non Carcinogenics	CTUh	4.23E-05
Respiratory Effects	kg $PM_{2.5}$ eq	2.00E-03
Ecotoxicity	CTUe	1.51E+01
Fossil Fuel Depletion	MJ surplus	1.32E+00

Table B.19. Absolute values of environmental impacts for producing 1 g of g-C_3N_4 nanosheets including electricity as the only input (CTU: Comparative Toxic Unit, h: for humans, e: for ecosystems, eq: equivalents).

Impact category	Unit	Supramolecular	Thermal etching
Ozone Depletion	kg CFC-11 eq	4.20E-07	9.44E-08
Global Warming	kg CO_2 eq	1.04E+01	2.33E+00
Smog	kg O_3 eq	3.85E-01	8.66E-02
Acidification	kg SO_2 eq	4.34E-02	9.76E-03
Eutrophication	kg N eq	2.27E-02	5.10E-03
Carcinogenics	CTUh	3.81E-07	8.57E-08
Non Carcinogenics	CTUh	1.33E-06	2.99E-07
Respiratory Effects	kg $PM_{2.5}$ eq	2.67E-03	6.01E-04
Ecotoxicity	CTUe	3.02E+01	6.78E+00
Fossil Fuel Depletion	MJ surplus	1.19E+01	2.68E+00

Table B.20. Absolute values of environmental impacts for producing 1 g of g-C_3N_4 nanosheets when reducing or removing the synthesis associated electricity (CTU: Comparative Toxic Unit, h: for humans, e: for ecosystems, eq: equivalents).

Impact category	Unit	Supramolecular (reducing electricity to 0.93 kWh)	Thermal etching (zero electricity)
Ozone Depletion	kg CFC-11 eq	4.04E-08	4.83E-08
Global Warming	kg CO_2 eq	1.01E+00	1.19E+00
Smog	kg O_3 eq	1.04E-01	4.41E-02
Acidification	kg SO_2 eq	6.05E-03	5.53E-03
Eutrophication	kg N eq	2.33E-03	2.63E-03
Carcinogenics	CTUh	3.66E-08	4.36E-08
Non Carcinogenics	CTUh	1.29E-07	1.53E-07
Respiratory Effects	kg $PM_{2.5}$ eq	3.29E-04	3.28E-04
Ecotoxicity	CTUe	2.94E+00	3.46E+00
Fossil Fuel Depletion	MJ surplus	1.48E+00	1.37E+00

Appendix C Additional Published Work

Evaluation of Phi6 Persistence and Suitability as an Enveloped Virus Surrogate

Reprinted (adapted) with permission from:

Aquino de Carvalho, N.; Stachler, E. N.; Cimabue, N.; Bibby, K. *Environmental Science & Technology*, **2017**, 51, 15, 8692–8700. DOI: 10.1021/acs.est.7b01296

Recent outbreaks involving enveloped viruses, such as Ebola virus, have raised questions regarding the persistence of enveloped viruses in the water environment. Efforts have been made to find appropriate enveloped virus surrogates due to challenges investigating enveloped viruses that require biosafety-level 3 or 4 handling. In this study, the enveloped bacteriophage Phi6 was evaluated as a surrogate for enveloped waterborne viruses. The persistence of Phi6 was tested in representative aqueous conditions chosen based on previously published viral persistence studies. Our results demonstrated that the predicted T90 (time for 90% inactivation) of Phi6 under the evaluated conditions varied from 24 minutes to 117 days depending on temperature, biological activity, and aqueous media composition. Phi6 T90 was compared with the T90 of other enveloped viruses reported in the literature. The apparent suitability of Phi6 as an enveloped virus surrogate was dependent on the temperature and composition of the media tested. Phi6 was not a universally conservative enveloped virus surrogate – 33% of evaluated virus-condition combinations had T90 values greater than the 95% confidence interval for Phi6. Ultimately, these results highlight the variability of enveloped virus persistence in the environment and the value of working with the virus of interest for environmental persistence studies.

C.1 Introduction

Recent disease outbreaks of enveloped viruses, such as Ebola virus,[213] Coronaviruses (e.g. MERS and SARS),[214-216] Hantavirus,[217] and Lassa virus,[218] have raised questions regarding the appropriate management of infectious patient waste, including wastewater, and the persistence of these viruses in the water environment.[219] Multiple enveloped viruses require biosafety level (BSL) 3 or 4 handling, such as Ebola virus, Marburg virus, Hantavirus, Lassa virus, and SARS and MERS Coronaviruses.[220] It is challenging to perform environmental persistence studies with these pathogens because access to BSL3 and BSL4 laboratories is expensive and limited. Historically it has been assumed that most enveloped viruses are rapidly inactivated in the environment;[221,222] however, recent studies have undermined this assumption. For example, infectious Ebola virus persisted in sterile wastewater for at least eight days.[223] In addition, a recent review highlighted that the T90 (time for 90% virus inactivation) varied from hours to months for enveloped viruses.[221] Consequently, it is desirable to work with agents that do not require access to BSL3 or BSL4 laboratories to conduct environmental persistence studies of these viruses. Subsequently, efforts have been made to find appropriate virus surrogates[222,224-227] – viruses that mimic the behavior of the pathogen of concern but are available at lower biosafety levels.

Bacteriophage Phi6 is a candidate surrogate for enveloped viruses. Phi6 is a member of the family *Cystoviridae*, which are unique among bacteriophages to have a lipid envelope.[228] This bacteriophage has a double-stranded RNA genome of 13.4 kbp,[229] a diameter of 75 nm[230], a nucleoprotein capsid of 60 nm in diameter[230,231], and 10 major coat proteins.[231,232] Phi6 has been widely used as an enveloped virus surrogate[222,224,226,227,233-235] and offers many advantages as a potential surrogate. First, both Phi6 and its host, *Pseudomonas syringae,*[236] are nonpathogenic to

humans and require minimal containment (BSL 1).[237,238] Second, its envelope makes it a potentially suitable model for studies of mammalian enveloped viruses due to physiological similarity.[239] Third, Phi6 and its host are easily cultivated in the laboratory, the analysis time is relatively rapid, and the assays are cost-effective.[224] Other bacteriophage members of the *Cystoviridae* family are also enveloped and share similar characteristics,[236,240,241] ; however, Phi6 was the first to be isolated[228] and is the best characterized,[242-244] which is why it has historically been chosen as an enveloped virus surrogate.

Despite the aforementioned advantages as an enveloped viral surrogate, the suitability of Phi6 for this application has yet to be formally evaluated. The appropriate surrogate choice should have a similar inactivation profile to the virus of comparison. The inactivation behavior for persistence studies is commonly represented by the time necessary for 90% reduction of the virus titer (T90), which assumes linear inactivation. Consequently, the evaluation of the potential surrogate can be performed by comparing its T90 value with the one of the pathogen of concern.

In this study, the bacteriophage Phi6 was evaluated as a surrogate for enveloped virus persistence in liquid. Application of Phi6 to study enveloped virus transport or persistence on surfaces was not considered. The persistence of Phi6 was evaluated in representative aqueous conditions chosen based on previously published studies. Additionally, a regression model for the effect of temperature on the persistence of Phi6 in DI water was developed. Finally, to assess the suitability of Phi6 as a surrogate for enveloped viruses, we performed a meta-analysis to compare the persistence of Phi6 with other enveloped viruses reported in the literature.

C.2 Materials and Methods

C.2.1 Phi6 Stock Preparation and Quantification

Bacteriophage Phi6 and its host *Pseudomonas syringae* (HB10Y) were kindly provided by Dr. Leonard Mindich (Public Health Research Institute Center, New Jersey Medical School - Rutgers, The State University of New Jersey). *Pseudomonas syringae* was propagated in 6 mL of Luria-Bertani (LB) Broth Lennox containing 5 g L^{-1} NaCl and incubated overnight at 25°C. Phi6 bacteriophage was grown in *Pseudomonas syringae* by overlaying 35mL of LB agar (1.5% agar) with 6 mL of diluted soft agar (3 mL LB broth plus 3mL LB soft agar – 0.6% agar) containing 1mL of an overnight culture of HB10Y and 10^5 PFU Phi6. The plate was incubated overnight at 25°C. The top layer was harvested and purified by centrifuging at 14,000 rpm for 15 minutes at 4°C. The supernatant Phi6 stock was enumerated and stored at -80°C.

C.2.2 Media Preparation

Experiments were conducted in cell culture media (Dulbecco's modified Eagle's medium, Sigma) and guinea pig sera (Sigma) as previously described by Piercy et al.[245] DI water was produced by a Millipore Synergy® UV Water Purification System and stored at room temperature. Tap water was collected from the faucet in the Environmental Engineering laboratory at the University of Pittsburgh. The tap was run for 5 minutes to purge the system and samples were collected in sterile 50 mL Falcon tubes. The free chlorine of the tap water was measured using a Hach kit (DR900, program 80) and dechlorinated using a 46 g/L solution of sodium thiosulfate. The free chlorine was measured again after sodium thiosulfate addition to ensure dechlorination of the tap water. River water samples were collected from the Allegheny River in Pittsburgh on

02/04/2016, sealed in sterile plastic bottles and transported on ice to the University of Pittsburgh. Two bottles were immediately stored at 4°C and two were autoclaved before storage at 4°C. Experiments began the same day, and remaining samples were stored at -80°C for future characterization. Both autoclaved and non-autoclaved samples were sent to Microbac Laboratories (Marietta, OH) overnight on ice for physical and chemical analysis (**Table D.1**). Wastewater influent was collected from an anonymous wastewater treatment plant in western Pennsylvania. Samples were collected in sterilized bottles and kept on ice while transported to the lab. Upon arrival to the lab, samples were frozen at -80°C to minimize changes in the chemical composition. On the day of the experiment, a sample bottle was thawed and autoclaved for 15 minutes. The autoclaved sample was sent to Microbac Laboratories (Marietta, OH) for chemical analysis (**Table D.1**).

C.2.3 Phi6 Persistence Experiments

Phi6 stock was spiked into 20 mL samples of liquid media – cell culture media, guinea pig sera, deionized water (DI), dechlorinated tap water, autoclaved river water, river water, or autoclaved wastewater influent – to a final concentration of $10^6 – 10^7$ PFU mL^{-1}. Spiked samples were immediately mixed and separated into 30 individual aliquots, which were stored in the dark for persistence experiments: cell culture media at 4°C and room temperature (RT = 22°C ±1°C), guinea pig sera at 4°C and RT, autoclaved river water and river water at 23°C, autoclaved wastewater at RT, dechlorinated tap water at RT, and DI at 4°C, 25°C, 37°C, and 45°C. At each sampling time point, three aliquots were selected from the test condition and the concentration of infectious particles of Phi6 was determined using double agar overlay plaque assay. Dulbecco's Modified Eagle's medium (DMEM) was used for the dilution of samples for Phi6 quantification. Negative controls were DMEM without Phi6. Plates containing between 10 and 100 plaques were

counted after 24 hours incubation at 25°C. Phi6 concentration from sample and technical triplicates was expressed in PFU mL^{-1}.

C.2.4 Data Analysis

Phi6 concentration at each time point was expressed as $\log_{10}(C_t/C_0)$ – where C_t is the virus concentration in PFU mL^{-1} at time t, and C_0 is the mean virus concentration in PFU mL^{-1} at time zero. The theoretical lower detection limit for virus concentration in the experiment was 100 PFU mL^{-1}. Undetected virus observations were assumed to have a concentration of 50 PFU mL^{-1} – half of the lower theoretical detection limit – for analysis. We ceased measuring Phi6 concentration when the total experiment duration was over or when the virus concentration values were under the detection limit for two consecutive sampling points. For the experiment performed at 45°C, we stopped sampling after two hours based upon preliminary experiments.

Linear regression models for Phi6 inactivation were obtained using GraphPad Prism version 7.00 (La Jolla, CA), and used to calculate T90 values. GraphPad Prism was used to compare the slopes of different conditions by performing the extra-sum-of-squares F test. To assess data deviation from linearity, the Runs test was performed. Statistical comparison between T90 values was achieved using the 2-sample t-test with unequal variances from Minitab 17.3.1. The significance level was 95%, i.e. *P* values smaller than 0.05 were considered statistically significant.

C.2.5 Literature Meta-Analysis

A literature review was performed to obtain T90 values of enveloped viruses or regression models of enveloped virus persistence in aqueous media. The articles of interest were found by

searching the database Compendex using the terms “virus” AND “persistence” in “all fields”. Additionally, references from the papers selected were checked and articles with relevant information were included. When T90 values were not explicit by the authors, they were read from graphs or calculated from linear regression models.

Published studies of viral persistence were performed in different pH, temperature, and salinity conditions; therefore, to enable comparison between viral persistence, we chose to include the values of viral persistence in a pH range of 6 – 9, and 0 ppt salinity, when specified. This pH range was chosen because most organisms present greatest stability at a near-neutral pH,[246] and the salinity constraint was chosen to eliminate the effect of salinity in viral inactivation.[247,248]

C.3 Results

Phi6 Persistence

The persistence of bacteriophage Phi6 was calculated from each experimental condition: cell culture media (4°C and RT), guinea pig sera (4°C and RT), river water (autoclaved and non-autoclaved at 23°C), autoclaved untreated wastewater (RT), dechlorinated tap water (RT), and deionized water (4°C, 25°C, 37°C, 45°C) (**Table C.1**).

Table C.1. Linear regression models for survival of bacteriophage Phi6 in liquid media at different conditions.

Matrix	Temperature (ºC)	T-90 (d) (95%CI) [A]	Linear regression model [B]	First order rate constant k (d^{-1}) (95%CI)
Autoclaved river water	23	7.1 (5.8 to 9.3)	Y = -0.140*X	-0.140 (-0.173 to -0.108)
Non-autoclaved river water	23	3.1 (2.3 to 4.7)	Y = -0.322*X	-0.322 (-0.430 to -0.213)
Cell culture media	RT	8.4 (6.3 to 12.4)	Y = -0.119*X	-0.119 (-0.158 to -0.081)
Cell culture media	4	116.9 (20.1 to +infinity)	Y = -0.009*X	-0.009 (-0.050 to 0.033)
Dechlorinated tap water	RT	3.1 (2.2 to 5.3)	Y = -0.321*X	-0.321 (-0.453 to -0.189)
Autoclaved wastewater influent	RT	2.5 (2.4 to 2.7)	Y = -0.398*X	-0.398 (-0.419 to -0.377)
Guinea pig sera	RT	5.3 (5.0 to 5.6)	Y = -0.189*X	-0.189 (-0.201 to -0.178)
Guinea pig sera	4	72.7 (46.5 to 166.5)	Y = -0.014*X	-0.014 (-0.022 to 0.006)
DI water	4	66.1 (30.2 to +infinity)	Y = -0.015*X	-0.015 (-0.033 to 0.003)
DI water	25	1.6 (1.4 to 1.8)	Y = -0.634*X	-0.634 (-0.711 to -0.557)
DI water	37	0.34 (0.32 to 0.37)	Y = -2.907*X	-2.907 (-3.101 to -2.712)
DI water	45	0.017 (0.015 to 0.021)	Y = -57.52*X	-57.52 (-67.26 to -47.79)

Phi6 inactivation followed first-order kinetics in all tested conditions – i.e., none of the linear regression models had a statistically significant deviation from linearity. Two alternative non-linear regression models were tested as a possible better fit for the persistence curves. When compared to the linear regression model, the one-phase exponential decay curve was the best fit for non-autoclaved river water, and the second order polynomial (quadratic) was the best fit for dechlorinated tap water, guinea pig sera at RT, and DI water at 4°C and 45°C (**Table D.2**). Non-linear models have been previously reported for Phi6 inactivation in pasteurized sewage.[227] Published enveloped viruses persistence studies have reported T90 values calculated from linear regression models; therefore, we utilized linear regression models for all conditions as the linear regression models were statistically valid and enabled the comparison of T90 values obtained in this study with literature values. Viral persistence significantly decreased over time ($P < 0.05$), i.e. the slopes were significantly different from zero, for all conditions except for guinea pig sera at 4°C ($P = 0.5561$) and DI water at 4°C ($P = 0.0878$).

Inactivation of Phi6 was assessed for different liquid media under the same temperature conditions to evaluate the role of aqueous media composition on Phi6 persistence. Phi6 persistence in cell culture media and guinea pig sera was measured over a period of 46 days, and in DI water and autoclaved wastewater over a period of 28 days. There was a statistically significant effect of matrix composition on Phi6 persistence when the experiment was conducted at RT (**Figure C.1.A**, $P < 0.0001$), but it was not significant at 4°C (**Figure C.1.B**, $P = 0.8905$). In the experiment at RT, Phi6 inactivation was fastest in DI, followed by autoclaved wastewater, guinea pig sera, and cell culture media.

Phi6 persistence in autoclaved and non-autoclaved river water was measured over 28 days at 23°C (**Figure C.1.C**) to investigate the role of microbiological activity on Phi6 inactivation.

Phi6 inactivation was significantly faster in non-autoclaved river water when compared to autoclaved river water ($P < 0.0001$).

To assess the role of temperature on inactivation rate, Phi6 persistence was quantified in DI water at 4°C, 25°C, 37°C, and 45°C (**Figure C.1.D**). The effect of temperature on Phi6 persistence was statistically significant ($P < 0.0001$), with Phi6 persistence decreasing with increasing temperature. At 45°C, Phi6 abundance decreased to below the limit of detection within 2 hours. The temperature effect was also observed in other matrices considered: the inactivation kinetics of Phi6 were significantly faster in guinea pig sera ($P < 0.0001$) and cell culture media ($P = 0.0003$) at RT when compared to 4°C.

The effect of temperature on viral inactivation has previously been reported in the literature.[222,225,227,245,247-256] We subsequently developed a temperature model for Phi6 persistence in DI water (**Figure C.2**). DI water was chosen to avoid the interference of biological activity and media composition. The relationship between $\log_{10}$(T90), where T90 is in days, and temperature (°C), followed the linear regression model $\log_{10}(T90) = 2.23 - 0.082*\text{temperature}$ ($R^2 = 0.97$) (**Figure C.2**).

Figure C.3 is a compilation of T90 values obtained from the Phi6 persistence studies and T90 values of enveloped viruses from the literature. Overall, the persistence of enveloped viruses varies widely for comparable conditions, and is highly dependent upon virus type, aqueous matrix composition, and temperature. For our meta-analysis, we considered room temperature to be from 20°C to 25°C. Based on our temperature model for Phi6 persistence in DI water, the difference in T90 values between temperatures of 20°C and 25°C would be 2.4 days.

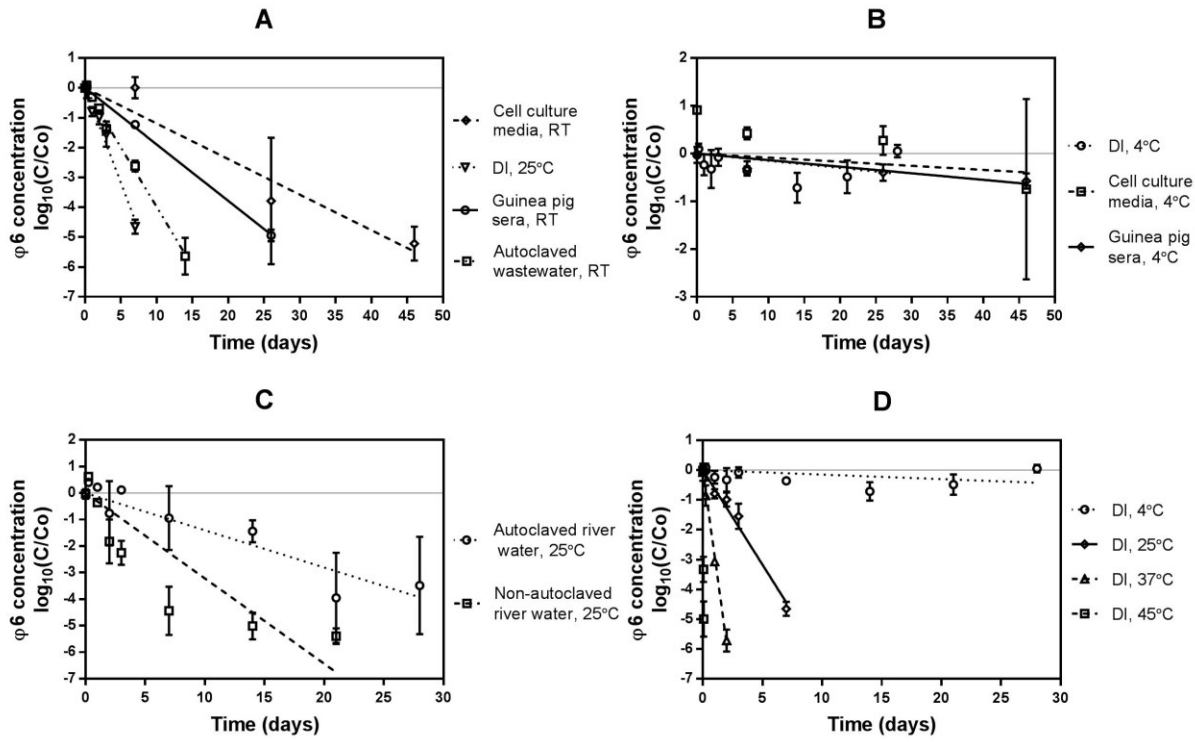

[A] T-90 value: Time required for 90% reduction in virus infectivity.

[B] $Y = \log_{10}(C/Co)$; X = persistence in days.

Figure C.1. Experimentally determined Phi6 persistence and linear regression models of the bacteriophage Phi6 in liquid media under different conditions. A) Phi6 inactivation at room temperature (RT) in different matrices. The reduction of virus concentration was significantly different for the matrices considered ($P < 0.0001$). B) Phi6 inactivation at 4°C in different matrices. The reduction of virus concentration was not significantly different for the matrices considered ($P = 0.8905$). Viral persistence did not significantly decrease over time in guinea pig sera ($P = 0.0861$) and DI water ($P = 0.5732$). C) Phi6 inactivation at 25°C in sterilized and non-sterilized river water. Virus persistence was reduced significantly faster in non-sterilized river water than in sterilized river water ($P < 0.0001$). D) Phi6 inactivation in DI water. Viral persistence decreased with temperature increase ($P < 0.0001$). Both biological and technical triplicates were taken at each time point. Geometric symbols represent mean value of the $\log_{10}$ of the virus concentration at each sample time over the mean concentration at time zero. Error bars indicate 95% confidence intervals (n = 9). Error bars not evident on the figure are smaller than the geometric symbol. Grey line represents zero viral decay.

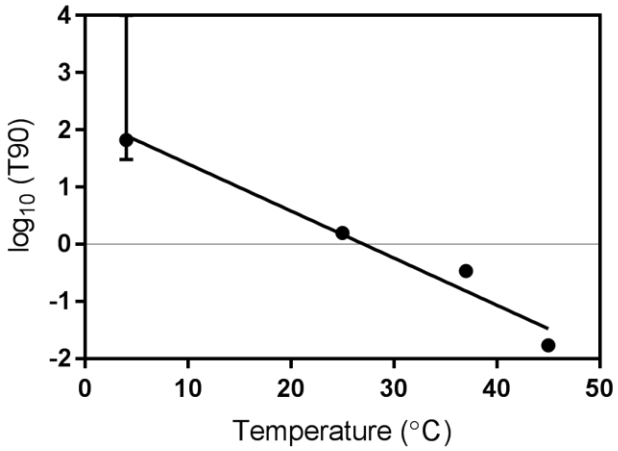

Figure C.2. Linear regression model for the change of Phi6 T90 value (days) with temperature variation. The relationship between $\log_{10}$(T90) and temperature was linear; therefore, increasing temperature causes time for 90% inactivation of the virus to decrease. Persistence studies were conducted in DI at four different temperatures (4°C, 25°C, 37°C, 45°C). Error bars indicate 95% confidence internals. Error bars not evident on the figure are smaller than the geometric symbol. The upper 95% CI of the $\log_{10}$ (T90) value at 4°C is large because viral reduction was not significant over time and the upper 95% CI of the slope was positive. For this experiment, the linear regression model obtained was Y = 2.23 – 0.082*X, with R^2 equals 0.97 and first order rate constant k ($°C^{-1}$) (95%CI) equals -0.082 (-0.128 to -0.037).

Comparing Phi6 T90 values from our study with T90 values of other enveloped viruses published in the literature, we found that Phi6 inactivation was more rapid, i.e. reported viral T90 values were above the confidence interval for Phi6, than all other viruses in guinea pig sera at RT (2 viruses), and wastewater at RT (4 viruses). Conversely, all viruses considered in cell culture media at 4°C (7 viruses), DI at 4°C (28 viruses), dechlorinated tap water at RT (3 viruses), and guinea pig sera at 4°C (2 viruses) had mean T90 values under the upper bound of the 95% CI for Phi6. The percentages of the viruses with greater persistence than Phi6 were 67% (6/9) for natural

waters at RT, 11% (2/18) for cell culture media at RT, 84% (16/19) for DI at RT, and 50% (2/4) for sterilized wastewater at RT.

In order to expand our evaluation of Phi6 suitability as a surrogate for enveloped viruses, we compared Phi6 T90 values obtained in the literature with T90 values of other enveloped viruses from previously published studies. As our study and one prior published study overlapped in a single evaluated condition (sterilized wastewater at RT), we used a 2-sample t-test with unequal variances to compare our Phi6 T90 value with that reported by Ye et al. (2016).[222] The verification of variance inequality was performed with the F-test ($P < 0.001$), and the two T90 values were not statistically significantly different ($P = 0.256$). The percentages of the viruses investigated that were more persistent than reported Phi6 T90 values from other studies were 33% (22/67) for DI at 17°C, 33% (21/63) for DI at 27-28°C, 100% (1/1) in wastewater at 10°C, and 0% (0/1) for sterilized wastewater at 10°C.

Accounting for all enveloped viruses obtained from the meta-analysis, 33% (76/228) had mean T90 values higher than the upper limit of the confidence interval of Phi6. Considering viruses that had data available for at least three conditions, only strains of influenza virus (H2N4, H5N7, H9N2, H11N6, and H12N5) never had a T90 value higher than the upper limit of the confidence interval of Phi6.

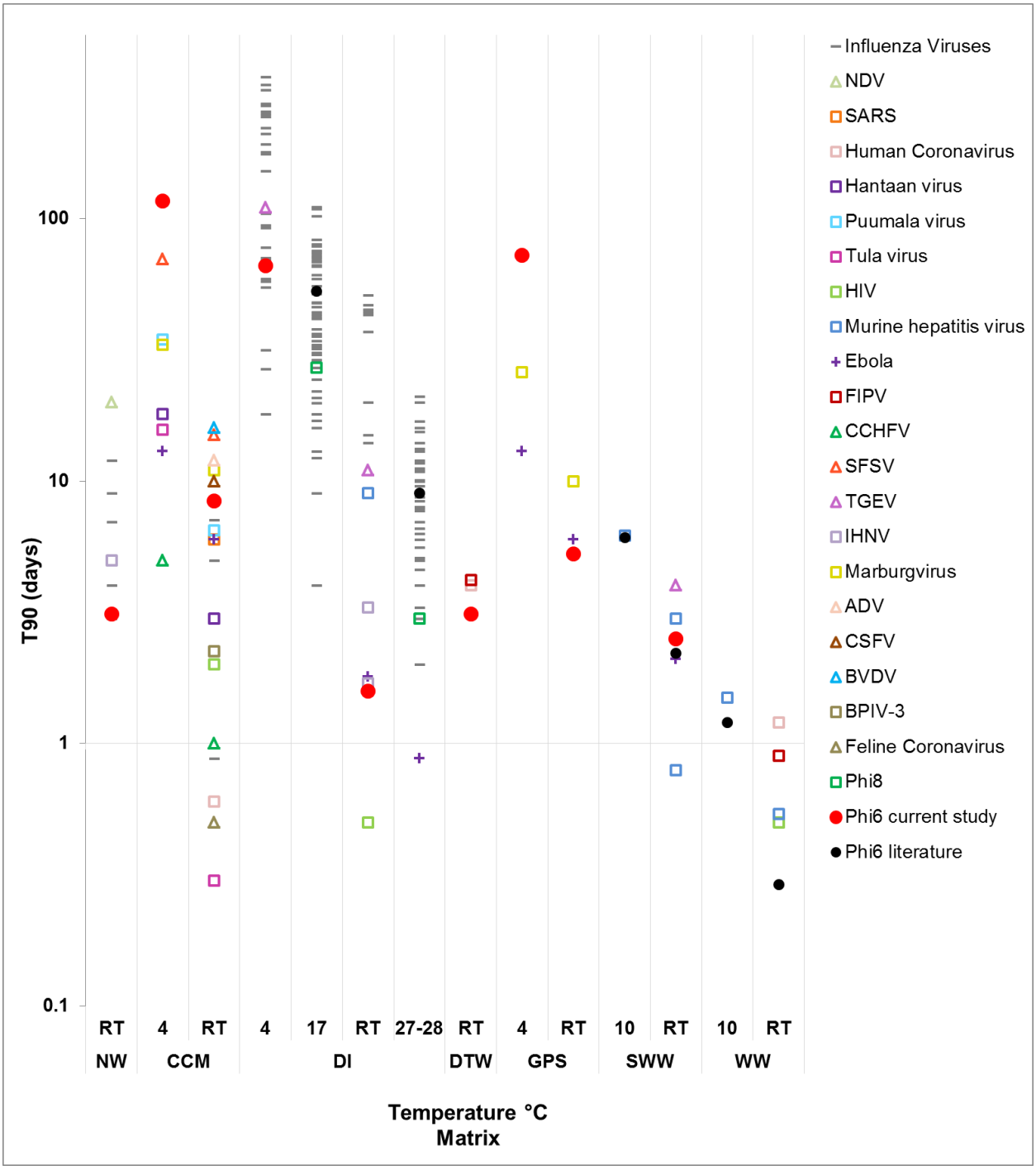

Figure C.3. T90 (days) of Phi6 obtained on this current study and of various enveloped viruses reported in the literature. [222-225,245,247,248,250-273] **Details of persistence studies obtained from literature review are shown in Table D.3. Error bars on "Phi6 current study" indicate 95% CI, and on "Phi6 literature" indicate standard deviation. RT = room temperature (20°C – 25°C); NW = natural water; ARW = autoclaved river water; CCM = cell culture media; DI = deionized water; DTW = dechlorinated tap water; GPS = guinea pig sera;**

SWW = sterilized wastewater; WW = wastewater. NDV = Newcastle disease virus; FIPV = Feline infectious peritonitis virus; CCHFV = Crimean-Congo hemorrhagic fever virus; SFSV = Sandfly fever Sicilian virus; TGEV = Transmissible gastroenteritis virus; IHNV = Infectious haematopoietic necrosis virus; ADV = Aujeszky's disease virus; CSFV = Classical swine fever virus; BVBD = Bovine viral diarrhea virus; BPIV-3 = Bovine parainfluenza virus type 3. HIV T90 (1 hour) in DTW was excluded from the graph.

C.4 Discussion

We assessed Phi6 persistence under representative aqueous conditions selected from the literature and analyzed the suitability of Phi6 as a surrogate for enveloped virus persistence. We found that Phi6 inactivation was significantly affected by temperature, biological activity, and liquid media composition, consistent with previous reports for enveloped viruses. In addition, we found that enveloped virus persistence varies widely and the apparent suitability of Phi6 as a surrogate is dependent upon the evaluated condition.

C.4.1 Environmental Factors Affecting Virus Inactivation

Our results demonstrated that temperature, biological activity, and matrix composition have a significant effect on the persistence of Phi6. These trends are consistent with those previously observed for other enveloped viruses.[222,225,245,247-253,255,256,259,260,263,264,267,272,274] Moreover, our meta-analysis highlights that virus persistence in water also varies between viral strains.[221,252,254]

In the present study, Phi6 inactivation in all evaluated conditions followed first-order kinetics, consistent with previous findings.[222] In five cases, the best-fit regression model for Phi6 persistence was found to be a one-phase exponential decay or second order polynomial. This

inactivation behavior suggests that a subpopulation of viruses may persist longer than predicted by a linear decay model. An apparent decrease in the Phi6 inactivation rate was also observed in sewage in a previously published study.[227] The mechanism that promotes such virus resistance behavior is not yet understood; however, attempts to model apparent biphasic pathogen decay are ongoing.[275] It is critical to elucidate the mechanisms of enhanced persistence and to further consider viral subpopulations with potentially enhanced persistence in future studies evaluating viral persistence and disinfection.

The role of temperature in viral persistence as observed in this study has been widely reported. Decreasing persistence with increasing temperature is attributed to the denaturation of proteins and nucleic acids, and the increased activity of extracellular enzymes.[246,255]

The effect of matrix composition on viral persistence may be due to multiple factors. Organic content can protect microorganisms from disinfection processes[276] and can be used as a nutrient supply by active microorganisms, possibly supporting the growth of microbial predators.[246] In addition, ammonia inactivates viruses by genome degradation, and RNA viruses have been shown to be more sensitive to inactivation by ammonia than DNA viruses.[277] Aggregation or adsorption of viral particles to particles in liquid media has been previously suggested to play a role in rapid virus decrease, which would be only an apparent viral decrease and not true virus inactivation.[223] Although we found a statistically significant difference ($P < 0.0001$) between Phi6 inactivation in guinea pig sera and cell culture media, a previous study investigating Ebola virus and Marburg virus in the same experimental conditions found no significant difference in virus survival.[245] This variation suggests that inactivation mechanisms related to the matrix composition are different between enveloped virus types.

The effect of biological activity on viral persistence has been previously studied, and is suggested to be due to microbial predation[278] or cleavage of viral proteins by proteolytic bacterial enzymes.[279] Biomacromolecules that result from microbial activity such as proteases, deoxyribonucleases (DNase), and ribonucleases (RNase) have been reported to have a virucidal effect.[280] Proteases are proposed to inactivate virus by catalyzing the viral protein envelope (capsid), and DNase/RNase by disintegrating the nucleic acid core of DNA/RNA viruses.[280] The specific mechanisms for inactivation of enveloped viruses due to biological activity are not well understood, and this is a necessary area of further investigation. This effect is associated with sterilization practices during laboratory experiments and is often necessary for subsequent viral culture. Sterilization was observed to enhance Phi6 persistence in liquid media for this and previous studies; however, previous work with murine hepatitis virus (MHV) demonstrated similar decay rates between pasteurized and non-pasteurized wastewater at 25°C,[222] suggesting that this trend may not be universal. Based upon these observations, it is recommended that virus persistence studies are performed in non-sterilized media, when possible, or that authors note this likely enhanced persistence due to sterilization.

C.4.2 Suitability of Phi6 as a Surrogate for Enveloped Viruses

Consistent with a recent review,[221] our meta-analysis suggests that enveloped virus persistence varies by orders of magnitude depending on the environmental conditions, and it may take hours to weeks for a one $\log_{10}$ decay of various enveloped viruses under relevant environmental conditions. This finding is contrary to the assumption that enveloped viruses are rapidly inactivated in the environment. The persistence of enveloped viruses in liquid may be of potential concern for secondary disease transmission, especially during wastewater handling in

outbreak response.[219] This study highlights the continued importance of environmental persistence studies for emerging enveloped viruses.

For Phi6 to be a desirable surrogate, the T90 value of Phi6 should be similar (within the 95% CI) or higher than the T90 of the virus of interest. The apparent suitability of Phi6 as a surrogate was dependent on the evaluated condition. All evaluated viruses with at least three available conditions had a T90 value above the 95% confidence interval for Phi6 under at least one condition, with the exception of some strains of influenza virus. Subsequently, Phi6 cannot be considered to be a universally conservative surrogate for enveloped viruses in aqueous media. These results also highlight inter-virus variability in persistence trends under different conditions. To overcome this limitation, it would be necessary to identify other enveloped viruses that could be used as surrogates, or to work with the actual pathogen of interest. Moreover, we indicated that Phi6 was an adequate surrogate when its inactivation was significantly slower than the virus of concern; however, this assumption may lead to overestimating virus survival and unnecessary public safety policies. If surrogate work is necessary, it would be best to identify surrogates that mimic viral pathogen persistence as closely as possible, and to include multiple surrogates to capture the inherent variability of environmental viral persistence.

C.4.3 Study Limitations

This study had three main limitations. First, our analysis of Phi6 suitability as an enveloped virus surrogate was limited by published data. In addition, many studies do not report standard deviations, limiting our ability to statistically compare these values with observed Phi6 persistence. Second, in cases where T90 values or regression models for virus inactivation were not reported in the study, T90 values were estimated from graphs presented. Third, virus inactivation has been

shown to be affected by pH and salinity;[247,248,281] however, these factors were not considered in the current study.

C.4.4 Implications

While methods are being developed to estimate viral persistence *a priori* (e.g. censored regression modeling),[282] the inherently high variability of viral persistence necessitates pathogen survival studies to predict exposure after virus release in the environment.[221,246] Our study demonstrates that Phi6 is not a universal surrogate for enveloped viruses; therefore, it is recommended that multiple surrogates are considered to cover the wide range of virus persistence variability, and, when possible, the virus of interest itself should be used to determine viral persistence. Consequently, appropriate virus control and public health safety strategies can be developed for future cases of enveloped virus outbreaks.

Appendix D Supporting Information for Appendix C

Content: Liquid media characterization (autoclaved wastewater, autoclaved and non-autoclaved river water); Non-linear regression models for survival of bacteriophage Phi6 in liquid media at different conditions; Detailed conditions and time for 90% reduction of enveloped viruses infectivity (T90) from persistence studies reported in the literature.

Table D.1. Liquid media characterization.

Analyte (mg/L)	Autoclaved River Water	Non-Autoclaved River Water	Autoclaved Wastewater
Chemical Oxygen Demand	ND	18.8	125
Nitrogen, Ammonia	0.306	0.197	21.5
Nitrate (as N)	0.705	0.758	0.186
Phosphorus, Total	ND	ND	4.27
Nitrogen, Total Kjeldahl	ND	ND	14.1
Total Organic Carbon	2.69	2.64	38.9
Total Suspended Solids	3.50	4.00	95.5
Turbidity*	3.03	3.87	5.52
Volatile Suspended Solids	3.50	3.50	153
pH**	7.47	7.43	NM

*Measurement unit is NTU. **Dimensionless. ND = not detected at or above adjusted sample detection limit. NM = not measured.

Table D.2. Non-linear regression models for survival of bacteriophage Phi6 in liquid media at different conditions.

Matrix	Temp. (°C)	T-90 (d) (95%CI)	Best-fit non-linear regression model	R^2	K (d^{-1}) (95%CI)	Plateau (95%CI)	B1(95%CI)	B2(95%CI)
Non-autoclaved river water	23	1.1 (0.8 to 1.5)	One-phase exponential decay	0.97	0.182 (0.102 to 0.296)	-5.575 (-7.004 to -4.619)		
Dechlorinated tap water	RT	2.8 (1.7 to 7.7)	Second order polynomial	0.99			0.038 (-0.195 to 0.272)	-0.140 (-0.229 to -0.052)
Guinea pig sera	RT	5.7 (5.2 to 6.3	Second order polynomial	1			-0.17 (-0.184 to -0.156)	-0.0007 (-0.0013 to -0.0002)
Deionized water	4	Inf (9.8 to ∞)	Second order polynomial	0.81			-0.0916 (-0.1219 to -0.06133)	0.003 (0.002 to 0.005)
Deionized water	45	0.024 (0.0195 to 0.032)	Second order polynomial	1			-33.28 (-42.47 to -24.09)	-319.7 (-439.9 to -199.6)

Table D.3. Detailed conditions and time for 90% reduction of enveloped viruses infectivity (T90) from persistence studies reported in the literature.

Enveloped Virus	T90 (days)	Temp (°C)	pH	Matrix	Strain	Note	Ref
Ebola virus	13	4		Cell culture medium	E718	From graph	245
Crimean-Congo hemorrhagic fever virus (CCHFV)	5	4		Cell-free medium	IbAr 10200	From graph	250
Sandfly fever Sicilian virus (SFSV)	70	4		Cell-free medium	Sabin	From graph	250
Hantaan virus	18	4		Cell-free medium	76-118	From graph	250
Puumala virus	34.7	4		Cell culture medium	Sotkamo		262,270
Tula virus	15.7	4		Cell culture medium	Moravia		262,270
Marburgvirus (MARV)	33	4		Cell culture medium	Popp	From graph	245
Transmissible gastroenteritis virus (TGEV)	110	4	6	Reagent-grade water			225
Avian influenza virus H1N1	179	4	6.5	Distilled water	A/Paris/2590/2009	0 salinity	260
Avian influenza virus H1N1	152	4	6.5	Distilled water	A/NewCaledonia/20/99	0 salinity	260
Avian influenza Virus H1N1	77.7	4	7.2	Distilled water	A/green-winged teal/Louisiana/213GW/1987	0 salinity	247
Avian influenza virus H2N4	176.2	4	7.2	Distilled water	A/blue-winged teal/Texas/421717/2001	0 salinity	247
Avian influenza virus H3N2	94.6	4	7.2	Distilled water	A/mallard/Minnesota/199036/1999	0 salinity	247
Avian influenza virus H3N8	245	4	7.2	Distilled water	A/Mallard/MN/Sg-00169/2007		253
Avian influenza virus H3N8	211	4	7.2	Distilled water	A/Surface water/Minnesota/W07-2241/2007		264

Table D.3 (continued)

Avian influenza virus H4N6	270	4	7.2	Distilled water			264
Avian influenza virus H4N6	71	4	7.2	Distilled water	A/mallard/Minnesota/199057/1999	0 salinity	247
Avian influenza virus H4N8	323	4	7.2	Distilled water	A/Mallard/MN/Sg-00219/2007		253
Avian influenza virus H5N1	59	4		Distilled water	A/Mute swan/305/06		251
Avian influenza virus H5N2	31.6	4	7.2	Distilled water	A/Mallard/Minnesota/346250/2000	0 salinity	247
Avian influenza virus H5N3	192	4		Distilled water	A/Mallard/MN/355790/2000		271
Avian influenza virus H5N7	256	4		Distilled water	A/Ruddy Turnstone/NJ/828219/2001		271
Avian influenza virus H6N1	346	4	7.2	Distilled water	A/Mallard/MN/Sg-00170/2007		253
Avian influenza virus H6N2	274	4	7.2	Distilled water	A/Mallard/MN/Sg-00107/2007		253
Avian influenza virus H6N4	57.5	4	7.2	Distilled water	A/ring-billed gull/Georgia/421733/2001	0 salinity	247
Avian influenza virus H6N8	309	4	7.2	Distilled water	A/Green-winged teal/MN/Sg-00197/2007		253
Avian influenza virus H7N3	178	4		Distilled water	A/Mallard/MN/182761/1998		271
Avian influenza virus H7N3	222	4		Distilled water	A/Laughing Gull/NY/A100-2455/2001		271
Avian influenza virus H7N6	104.5	4	7.2	Distilled water	A/Northern shoveler/North Carolina/1523546/2005	0 salinity	247
Avian influenza virus H8N4	92.4	4	7.2	Distilled water	A/Northern pintail/Texas/421716/2001	0 salinity	247

Table D.3 (continued)

Avian influenza virus H9N2	54.7	4	7.2	Distilled water	A/ruddy turnstone/New Jersey/1016409/2009	0 salinity	247
Avian influenza virus H10N7	26.8	4	7.2	Distilled water	A/red knot/Delaware/AI00-1329/2000	0 salinity	247
Avian influenza virus H10N7	250	4	7.3	Distilled water	A/Green-Winged Teal/LA/169GW/88		272
Avian influenza virus H11N6	18	4	7.2	Distilled water	A/dunlin/Delaware/AI00-1459/2000	0 salinity	247
Avian influenza virus H12N5	69.8	4	7.2	Distilled water	A/mallard/Minnesota/355788/2000	0 salinity	247
Marburgvirus	26	4		Guinea pig sera	Popp	From graph	245
Ebola virus	13	4		Guinea pig sera	E718	From graph	245
Murine hepatitis virus	6.2	10		Pasteurized wastewater	A59		222
Phi6	6.1	10		Pasteurized wastewater			222
Murine hepatitis virus	1.5	10	7.63	Wastewater	A59		222
Phi6	1.2	10	7.63	Wastewater			222
Phi6	53	17	7.4	Distilled water		0 salinity	224
Phi8	27	17	7.4	Distilled water		0 salinity	224
Avian influenza Virus H1N1	55.3	17	7.4	Distilled water	A/green-winged teal/Louisiana/213GW/1987	0 salinity	247
Avian influenza Virus H1N1	51.8	17	7.2	Distilled water	A/green-winged teal/Louisiana/213GW/1987	0 salinity	247

Table D.3 (continued)

Avian influenza virus H2N4	32.5	17	7.4	Distilled water	A/blue-winged teal/Texas/421717/2001	0 salinity	247
Avian influenza virus H3N2	34.2	17	7.4	Distilled water	A/mallard/Minnesota/199036/1999	0 salinity	247
Avian influenza virus H3N8	83	17	7.2	Distilled water	A/Mallard/MN/Sg-00169/2007		253
Avian influenza virus H3N8	79	17	7.2	Distilled water	A/Surface water/Minnesota/W07-2241/2007		264
Avian influenza virus H3N8	13	17	6.2	Distilled water	A/Surface water/Minnesota/W07-2241/2007		264
Avian influenza virus H3N8	22	17	8.2	Distilled water	A/Surface water/Minnesota/W07-2241/2007		264
Avian influenza virus H3N8	32.3	17	7.3	Distilled water	A/Gadwall/LA/17G/87		272
Avian influenza virus H3N8	65.9	17	7.2	Distilled water	A/Mallard/Minnesota/Sg-00051/2007		263
Avian influenza virus H3N8	73.7	17	7.2	Distilled water	A/Mallard/Minnesota/Sg-00048/2007		263
Avian influenza virus H3N8	78.8	17	7.2	Distilled water	A/Mallard/Minnesota/199106/1999		263
Avian influenza virus H3N8	59.1	17	7.2	Distilled water	A/Mallard/Minnesota/Sg-00169/2007		263
Avian influenza virus H4N6	75.6	17	7.2	Distilled water	A/Mallard/Minnesota/Sg-00050/2007		263
Avian influenza virus H4N6	69.2	17	7.2	Distilled water	A/Mallard/Minnesota/Sg-00053/2007		263
Avian influenza virus H4N6	66.6	17	7.2	Distilled water	A/Mallard/Minnesota/199044/1999		263

Table D.3 (continued)

Avian influenza virus H4N6	46.2	17	7.2	Distilled water	A/Mallard/Minnesota/Sg-00063/2007		263
Avian influenza virus H4N6	47.6	17	7.8	Distilled water	A/mallard/Minnesota/199057/1999	0 salinity	247
Avian influenza virus H4N6	102	17	7.2	Distilled water	A/Surface water/Minnesota/NW1-T/2006		264
Avian influenza virus H4N6	9	17	6.2	Distilled water	A/Surface water/Minnesota/NW1-T/2006		264
Avian influenza virus H4N6	18	17	8.2	Distilled water	A/Surface water/Minnesota/NW1-T/2006		264
Avian influenza virus H4N6	35.7	17	7.3	Distilled water	A/Blue-Winged Teal/LA/44B/87		272
Avian influenza virus H4N8	109	17	7.2	Distilled water	A/Mallard/MN/Sg-00219/2007		253
Avian influenza virus H5N1	26	17	7.4	Distilled water	A/Whooper Swan/Mongolia/244/05	0 salinity	252
Avian influenza virus H5N1	16	17	7.4	Distilled water	A/Duck Meat/Anyang/01	0 salinity	252
Avian influenza virus H5N1	16	17	7.4	Distilled water	A/Duck Meat/Anyang/AVL-1/01	0 salinity	224
Avian influenza virus H5N1	26	17	7.4	Distilled water	A/Whooper Swan/Mongolia/244/05	0 salinity	224
Avian influenza virus H5N1	29	17	7.2	Distilled water	A/chicken/Hong Kong/220/1997	0 salinity	254
Avian influenza virus H5N1	42	17	7.2	Distilled water	A/chicken/Korea/ES/2003	0 salinity	254

Table D.3 (continued)

Avian influenza virus H5N1	27	17	7.2	Distilled water	A/chicken/Nigeria/-228-10/2006	0 salinity	254
Avian influenza virus H5N1	22	17	7.2	Distilled water	A/duck/Bac Lieu/NCVD 07-09/2007	0 salinity	254
Avian influenza virus H5N1	43	17	7.2	Distilled water	A/duck/Vietnam/201/2006	0 salinity	254
Avian influenza virus H5N1	44	17	7.2	Distilled water	A/environment/Hong Kong/485.3/2000	0 salinity	254
Avian influenza virus H5N1	69	17	7.2	Distilled water	A/goose/Vietnam/113/2001	0 salinity	254
Avian influenza virus H5N1	66	17	7.2	Distilled water	A/Vietnam/1203/2004	0 salinity	254
Avian influenza virus H5N1	33	17	7.2	Distilled water	A/West Java//PWT-WIJ/2006	0 salinity	254
Avian influenza virus H5N1	46	17	7.2	Distilled water	A/muscovy/Ha Nam/NCVD 07-84/2007	0 salinity	254
Avian influenza virus H5N1	75	17	7.2	Distilled water	A/egret/Hong Kong/757.2/2002	0 salinity	254
Avian influenza virus H5N2	41.5	17	8.2	Distilled water	A/mallard/Minnesota/346250/2000	0 salinity	247
Avian influenza virus H5N2	71	17	7.4	Distilled water	A/Mallard/MN/182742/98	0 salinity	252
Avian influenza virus H5N3	53	17	7.4	Distilled water	A/Mallard/MN/355790/00	0 salinity	252
Avian influenza virus H5N7	38	17	7.4	Distilled water	A/Ruddy Turnstone/NJ/828219/01	0 salinity	252
Avian influenza virus H5N8	48	17	7.4	Distilled water	A/Ruddy Turnstone/NJ/828227/01	0 salinity	252
Avian influenza virus H6N1	80	17	7.2	Distilled water	A/Mallard/MN/Sg-00170/2007		253
Avian influenza virus H6N2	61	17	7.2	Distilled water	A/Mallard/MN/Sg-00107/2007		253

Table D.3 (continued)

Avian influenza virus H6N2	4	17	6.2	Distilled water	A/mottled duck/LA/38M/87	0 salinity	248
Avian influenza virus H6N2	9	17	7.2	Distilled water	A/mottled duck/LA/38M/87	0 salinity	248
Avian influenza virus H6N2	17	17	8.2	Distilled water	A/mottled duck/LA/38M/87	0 salinity	248
Avian influenza virus H6N2	35.7	17	7.3	Distilled water	A/Mottled Duck/LA/38M/87		272
Avian influenza virus H6N4	32.7	17	8.2	Distilled water	A/ring-billed gull/Georgia/421733/2001	0 salinity	247
Avian influenza virus H6N8	72	17	7.2	Distilled water	A/Green-winged teal/MN/Sg-00197/2007		253
Avian influenza virus H7N3	36	17	7.4	Distilled water	A/Mallard/MN/182761/98	0 salinity	252
Avian influenza virus H7N3	32	17	7.4	Distilled water	A/Ruddy Turnstone/DE/650635/02	0 salinity	252
Avian influenza virus H7N3	111	17	7.4	Distilled water	A/Laughing Gull/DE/AI00-2455/00	0 salinity	252
Avian influenza Virus H7N4	29	17	7.4	Distilled water	A/Blue-winged Teal/TX/578579/02	0 salinity	252
Avian influenza virus H7N6	78.8	17	7.2	Distilled water	A/Northern shoveler/North Carolina/1523546/2005	0 salinity	247
Avian influenza virus H7N6	74.7	17	7.4	Distilled water	A/Northern shoveler/North Carolina/1523546/2005	0 salinity	247
Avian influenza virus H8N4	36.4	17	7.4	Distilled water	A/Northern pintail/Texas/421716/2001	0 salinity	247
Avian influenza virus H8N4	68.6	17	7.2	Distilled water	A/Northern Pintail/TX/421716/01		263

Table D.3 (continued)

Avian influenza virus H9N2	30.4	17	7.2	Distilled water	A/ruddy turnstone/New Jersey/1016409/2009	0 salinity	247
Avian influenza virus H9N2	30.8	17	7.0	Distilled water	A/ruddy turnstone/New Jersey/1016409/2009	0 salinity	247
Avian influenza virus H10N7	24.4	17	7.3	Distilled water	A/Green-Winged Teal/LA/169GW/88		272
Avian influenza virus H10N7	19.9	17	7.4	Distilled water	A/red knot/Delaware/AI00-1329/2000	0 salinity	247
Avian influenza virus H11N6	12.3	17	8.2	Distilled water	A/dunlin/Delaware/AI00-1459/2000	0 salinity	247
Avian influenza virus H12N5	20.8	17	7.3	Distilled water	A/Blue-Winged Teal/188B/87		272
Avian influenza virus H12N5	30.7	17	7.4	Distilled water	A/mallard/Minnesota/355788/2000	0 salinity	247
Avian influenza virus H1N1	9	20	7.84	Lake water	A/Puerto Rico/8/1934	pH measured in the beginning of the trial	266
Avian influenza virus H4N6	7	20	7.84	Lake water	A/Mallard/Wv1732-34/03	pH measured in the beginning of the trial	266
Avian influenza virus H4N6	4	20	7.84	Surface water	A/mallard/Germany Wv1732-34/03	pH relatively constant (might have fallen to 7.44)	267

Table D.3 (continued)

Avian influenza virus H5N1	7	20	7.84	Lake water	A/Teal/Wv/632/Germany/05	pH measured in the beginning of the trial	266
Avian influenza virus H5N1	3	20	7.84	Surface water	A/teal/Germany/Wv632/05	pH relatively constant (might have fallen to 7.44)	267
Avian influenza virus H6N8	12	20	7.84	Lake water	A/Mute Swan/Germany/R2927/07	pH measured in the beginning of the trial	266
Avian influenza virus H6N8	3	20	7.84	Surface water	A/mute swan/Germany/R2927/07	pH relatively constant (might have fallen to 7.44)	267
Newcastle disease virus (NDV)	20	20	7.84	Lake water		pH measured in the beginning of the trial	266
Infectious Haematopoietic Necrosis Virus (IHNV)	5	20	6.8	Freshwater	Metolius strain	0 salinity	273
SARS Coronavirus	6	21 - 25		Serum-free culture medium		From graph	269
Human Coronavirus	0.6	21 - 25		Serum-free culture medium	229E	From graph	269
Crimean-Congo hemorrhagic fever virus (CCHFV)	1	20		Cell-free medium	IbAr 10200	From graph	250

Table D.3 (continued)

Sandfly fever Sicilian virus (SFSV)	15	20		Cell-free medium	Sabin	From graph	250
Hantaan virus	3	20		Cell-free medium	76-118	From graph	250
Puumala virus	6.5	23		Cell culture medium	Sotkamo		262,270
Tula virus	0.3	23		Cell culture medium	Moravia		262,270
HIV	2	25		Cell culture medium	IIIB		259
Marburgvirus	11	RT		Cell culture medium	Popp	From graph	245
Ebola virus	6	RT		Cell culture medium	E718	From graph	245
Aujeszky's Disease Virus (ADV)	12	20		Cell culture medium	DK 3275/81	From graph	257
Classical Swine Fever Virus (CSFV)	10	20		Cell culture medium (EMEM)	Alfort	From graph	258
Bovine Viral Diarrhea Virus (BVDV)	16	20		Cell culture medium (EMEM)	UG 59	From graph	258
Swine Influenza Virus H1N1	5	20		Cell culture medium (EMEM)	4744	From graph	258
HIV	0.25 - 0.5	25	5.0 - 7.5	Sterile water (Gibco BRL)	IIIB		259
Avian Influenza Virus H7N1	0.88	25	7.6	Cell culture medium	A/turkey/Italy/ 1387/00		261
Avian Influenza Virus H5N3	7.13	25	7.6	Cell culture medium	A/mallard/Swe den/1174/05		261
Bovine Parainfluenza Virus type 3 (BPIV-3)	2.25	25	7.6	Cell culture medium	1878/88		261
Feline Coronavirus	0.5	25	7.6	Cell culture medium	DF2		261
Transmissible gastroenteritis virus (TGEV)	11	25	6	Reagent-grade water			225

Table D.3 (continued)

Murine hepatitis virus	9	25	6	Reagent-grade water			225
Ebola virus	1.8	21		DEPC-treated Water	Makona-WPGC07		256
Avian influenza virus H3N8	44	23	7.2	Distilled water	A/Mallard/MN/Sg-00169/2007		253
Avian influenza virus H3N8	51	23	7.2	Distilled water	A/Surface water/Minnesota/W07-2241/2007		264
Avian influenza virus H4N6	51	23	7.2	Distilled water	A/Surface water/Minnesota/NW1-T/2006		264
Avian influenza virus H4N6	15	20	7.84	Distilled water	A/mallard/Germany Wv1732-34/03	pH relatively constant (might have fallen to 7.44)	267
Avian influenza virus H4N8	47	23	7.2	Distilled water	A/Mallard/MN/Sg-00219/2007		253
Avian influenza virus H5N1	20	20		Distilled water	A/Mute swan/305/06		251
Avian influenza virus H5N1	14	20	7.84	Distilled water	A/teal/Germany/Wv632/05	pH relatively constant (might have fallen to 7.44)	267
Avian influenza virus H6N1	45	23	7.2	Distilled water	A/Mallard/MN/Sg-00170/2007		253
Avian influenza virus H6N2	43	23	7.2	Distilled water	A/Mallard/MN/Sg-00107/2007		253

Table D.3 (continued)

Avian influenza virus H6N8	44	23	7.2	Distilled water	A/Green-winged teal/MN/Sg-00197/2007		253
Avian influenza virus H6N8	37	20	7.84	Distilled water	A/mute swan/Germany/R2927/07	pH relatively constant (might have fallen to 7.44)	267
Infectious Haematopoietic Necrosis Virus (IHNV)	3.3	21	6	Distilled water			268
Infectious Haematopoietic Necrosis Virus (IHNV)	3.3	21	7	Distilled water			268
Infectious Haematopoietic Necrosis Virus (IHNV)	3.3	21	8	Distilled water			268
Infectious Haematopoietic Necrosis Virus (IHNV)	1.7	21	9	Distilled water			268
Human Coronavirus	4	23	7.8	Dechlorinated unfiltered tap water	229E		255
Feline infectious peritonitis virus (FIPV)	4.2	23	7.8	Dechlorinated unfiltered tap water			255
HIV	0.021 - 0.042	25	6.5 - 7.0	Dechlorinated Tap Water			265
Marburgvirus	10	RT		Guinea pig sera	Popp	From graph	245
Ebola virus	6	RT		Guinea pig sera	E718	From graph	245

Table D.3 (continued)

Transmissible gastroenteritis virus (TGEV)	4	25	7.6	Pasteurized settled sewage		pH measured before pasteurization	225
Murine hepatitis virus	3	25	7.6	Pasteurized settled sewage			225
Murine hepatitis virus	0.79	25		Pasteurized wastewater	A59		222
Phi6	2.21	25		Pasteurized wastewater			222
Ebola virus	2.1	20	8.6	Sterilized wastewater (gamma-irradiated)		pH measured before gamma-irradiation	223
Human Coronavirus	1.2	23		Primary wastewater effluent unfiltered	229E		255
Feline infectious peritonitis virus (FIPV)	0.9	23		Primary wastewater effluent unfiltered			255
HIV	0.5	25	6.5 - 7.5	Primary wastewater effluent			259
Murine hepatitis virus	0.54	25	7.6 3	Wastewater (before primary settling tanks)	A59		222
Phi6	0.29	25	7.6 3	Wastewater (before primary settling tanks)			222
Phi6	9	28	7.4	Distilled water		0 salinity	224
Phi8	3	28	7.4	Distilled water		0 salinity	224

Table D.3 (continued)

Ebola virus	0.88	27		DEPC Water			256
Avian influenza Virus H1N1	6.3	28	7.2	Distilled water	A/green-winged teal/Louisiana/213GW/1987	0 salinity	247
Avian influenza Virus H1N1	11.9	28	7.4	Distilled water	A/green-winged teal/Louisiana/213GW/1987	0 salinity	247
Avian influenza virus H2N4	8.4	28	7.2	Distilled water	A/blue-winged teal/Texas/421717/2001	0 salinity	247
Avian influenza virus H2N4	6.6	28	7.4	Distilled water	A/blue-winged teal/Texas/421717/2001	0 salinity	247
Avian influenza virus H3N2	6.3	28	7.2	Distilled water	A/mallard/Minnesota/199036/1999	0 salinity	247
Avian influenza virus H3N2	11.7	28	7.4	Distilled water	A/mallard/Minnesota/199036/1999	0 salinity	247
Avian influenza virus H3N8	14	28	7.2	Distilled water	A/Mallard/MN/Sg-00169/2007		253
Avian influenza virus H3N8	6	28	6.2	Distilled water	A/Surface water/Minnesota/W07-2241/2007		264
Avian influenza virus H3N8	11	28	7.2	Distilled water	A/Surface water/Minnesota/W07-2241/2007		264
Avian influenza virus H3N8	8	28	8.2	Distilled water	A/Surface water/Minnesota/W07-2241/2007		264
Avian influenza virus H3N8	10.9	28	7.3	Distilled water	A/Gadwall/LA/17G/87		272
Avian influenza virus H4N6	13	28	7.2	Distilled water	A/Surface water/Minnesota/NW1-T/2006		264

Table D.3 (continued)

Avian influenza virus H4N6	3	28	6.2	Distilled water	A/Surface water/Minnesota/NW1-T/2006		264
Avian influenza virus H4N6	7	28	8.2	Distilled water	A/Surface water/Minnesota/NW1-T/2006		264
Avian influenza virus H4N6	13.3	28	7.3	Distilled water	A/Blue-Winged Teal/LA/44B/87		272
Avian influenza virus H4N6	9.6	28	7.2	Distilled water	A/mallard/Minnesota/199057/1999	0 salinity	247
Avian influenza virus H4N6	7.9	28	7.4	Distilled water	A/mallard/Minnesota/199057/1999	0 salinity	247
Avian influenza virus H4N8	13	28	7.2	Distilled water	A/Mallard/MN/Sg-00219/2007		253
Avian influenza virus H5N1	4	28	7.4	Distilled water	A/Whooper Swan/Mongolia/244/05	0 salinity	252
Avian influenza virus H5N1	5	28	7.4	Distilled water	A/Duck Meat/Anyang/01	0 salinity	252
Avian influenza virus H5N1	5	28	7.4	Distilled water	A/Duck Meat/Anyang/AVL-1/01	0 salinity	224
Avian influenza virus H5N1	4	28	7.4	Distilled water	A/Whooper Swan/Mongolia/244/05	0 salinity	224
Avian influenza virus H5N1	5	28	7.2	Distilled water	A/chicken/Hong Kong/220/1997	0 salinity	254
Avian influenza virus H5N1	7	28	7.2	Distilled water	A/chicken/Korea/ES/2003	0 salinity	254
Avian influenza virus H5N1	10	28	7.2	Distilled water	A/chicken/Nigeria/-228-10/2006	0 salinity	254

Table D.3 (continued)

Avian influenza virus H5N1	2	28	7.2	Distilled water	A/duck/Bac Lieu/NCVD 07-09/2007	0 salinity	254
Avian influenza virus H5N1	21	28	7.2	Distilled water	A/duck/Vietnam/201/2006	0 salinity	254
Avian influenza virus H5N1	7	28	7.2	Distilled water	A/egret/Hong Kong/757.2/2002	0 salinity	254
Avian influenza virus H5N1	8	28	7.2	Distilled water	A/environment/Hong Kong/485.3/2000	0 salinity	254
Avian influenza virus H5N1	14	28	7.2	Distilled water	A/goose/Vietnam/113/2001	0 salinity	254
Avian influenza virus H5N1	16	28	7.2	Distilled water	A/Vietnam/1203/2004	0 salinity	254
Avian influenza virus H5N1	10	28	7.2	Distilled water	A/West Java//PWT-WIJ/2006	0 salinity	254
Avian influenza virus H5N1	6	28	7.2	Distilled water	A/muscovy/Ha Nam/NCVD 07-84/2007	0 salinity	254
Avian influenza virus H5N2	11.2	28	7.8	Distilled water	A/Mallard/Minnesota/346250/2000	0 salinity	247
Avian influenza virus H5N2	20	28	7.4	Distilled water	A/Mallard/MN/182742/98	0 salinity	252
Avian influenza virus H5N3	14	28	7.4	Distilled water	A/Mallard/MN/355790/00	0 salinity	252
Avian influenza virus H5N7	9	28	7.4	Distilled water	A/Ruddy Turnstone/NJ/828219/01	0 salinity	252
Avian influenza virus H5N8	6	28	7.4	Distilled water	A/Ruddy Turnstone/NJ/828227/01	0 salinity	252
Avian influenza virus H6N1	14	28	7.2	Distilled water	A/Mallard/MN/Sg-00170/2007		253
Avian influenza virus H6N2	13	28	7.2	Distilled water	A/Mallard/MN/Sg-00107/2007		253
Avian influenza virus H6N2	2	28	6.2	Distilled water	A/mottled duck/LA/38M/87	0 salinity	272

Table D.3 (continued)

Avian influenza virus H6N2	8	28	7.2	Distilled water	A/mottled duck/LA/38M/87	0 salinity	272
Avian influenza virus H6N2	8	28	8.2	Distilled water	A/mottled duck/LA/38M/87	0 salinity	272
Avian influenza virus H6N2	15.4	28	7.3	Distilled water	A/mottled duck/LA/38M/87		272
Avian influenza virus H6N4	10.9	28	8.6	Distilled water	A/ring-billed gull/Georgia/421733/2001	0 salinity	247
Avian influenza virus H6N8	10	28	7.2	Distilled water	A/Green-winged teal/MN/Sg-00197/2007		253
Avian influenza virus H7N3	11	28	7.4	Distilled water	A/Laughing Gull/DE/AI00-2455/00	0 salinity	252
Avian influenza virus H7N3	4	28	7.4	Distilled water	A/Ruddy Turnstone/DE/650635/02	0 salinity	252
Avian influenza virus H7N3	12	28	7.4	Distilled water	A/Mallard/MN/182761/98	0 salinity	252
Avian influenza virus H7N4	10	28	7.4	Distilled water	A/Blue-winged Teal/TX/578579/02	0 salinity	252
Avian influenza virus H7N6	9.6	28	7.8	Distilled water	A/Northern shoveler/North Carolina/1523546/2005	0 salinity	247
Avian influenza virus H8N4	10.0	28	7.2	Distilled water	A/Northern pintail/Texas/421716/2001	0 salinity	247
Avian influenza virus H8N4	7.7	28	7.8	Distilled water	A/Northern pintail/Texas/421716/2001	0 salinity	247
Avian influenza virus H9N2	5.6	28	7.2	Distilled water	A/ruddy turnstone/New Jersey/1016409/2009	0 salinity	247

Table D.3 (continued)

Avian influenza virus H9N2	3.3	28	7.4	Distilled water	A/ruddy turnstone/New Jersey/1016409/2009	0 salinity	247
Avian influenza virus H10N7	16.9	28	7.3	Distilled water	A/green-winged Teal/LA/169GW/88		272
Avian influenza virus H10N7	10.1	28	7.4	Distilled water	A/red knot/Delaware/AI00-1329/2000	0 salinity	247
Avian influenza virus H10N7	7.7	28	7.2	Distilled water	A/red knot/Delaware/AI00-1329/2000	0 salinity	247
Avian influenza virus H11N6	4.6	28	7.4	Distilled water	A/dunlin/Delaware/AI00-1459/2000	0 salinity	247
Avian influenza virus H12N5	5.1	28	7.3	Distilled water	A/Blue-Winged Teal/188B/87		272
Avian influenza virus H12N5	8.7	28	7.4	Distilled water	A/mallard/Minnesota/355788/2000	0 salinity	247

Appendix E Additional Publications Contributing to the Microbiology and Nanotechnology Fields

1. Wang, Y.; **Aquino de Carvalho, N.**; Tan, S.; Gilbertson, L. "Leveraging Electrochemistry to Uncover the Role of Nitrogen in the Biological Reactivity of Nitrogen-Doped Graphene". *Environmental Science: Nano*, **2019**, 6, 3525–3538. DOI: 10.1039/C9EN00802K

2. Stachler, E.; Akyon, B.; **Aquino de Carvalho, N.**; et al. "Correlation of crAssphage-based qPCR markers with culturable and molecular indicators of human fecal pollution in an impacted urban watershed". *Environmental Science & Technology*, **2018**, 52, 13, 7505–7512. DOI: 10.1021/acs.est.8b00638

3. Bibby, K.; Fischer, RJ.; Casson, LW.; **Aquino de Carvalho, N.**; Haas, CN.; Munster, VJ. "Disinfection of Ebola virus in sterilized municipal wastewater". *PLoS Neglected Tropical Diseases*, **2017**, 11 (2): e0005299. DOI: 10.1371/journal.pntd.0005299

4. Bibby, K.; **Aquino de Carvalho, N.**; Wigginton, K. "Research Needs for Wastewater Handling in Virus Outbreak Response". Environmental Science & Technology, **2017**, 51, 5, 2534–2535. DOI: 10.1021/acs.est.6b06492

Bibliography

1 World Health Organization (WHO). Drinking Water. Retrieved in November 2021 from https://www.who.int/news-room/fact-sheets/detail/drinking-water (2019).

2 Krasner, S. W. *et al.* Occurrence of a New Generation of Disinfection Byproducts. *Environmental Science & Technology* **40**, 7175-7185, doi:10.1021/es060353j (2006).

3 Anastasi, E. M., Wohlsen, T. D., Stratton, H. M. & Katouli, M. Survival of Escherichia coli in two sewage treatment plants using UV irradiation and chlorination for disinfection. *Water Research* **47**, 6670-6679, doi:https://doi.org/10.1016/j.watres.2013.09.008 (2013).

4 Gomes, J., Matos, A., Gmurek, M., Quinta-Ferreira, R. M. & Martins, R. C. Ozone and Photocatalytic Processes for Pathogens Removal from Water: A Review. *Catalysts* **9**, doi:10.3390/catal9010046 (2019).

5 BCC Publishing Staff. Advanced Technologies for Municipal Water Treatment (Report Code MST036E). *BCC Research*, Retrieved in November 2021 from https://www.bccresearch.com/ (2021).

6 Fierascu, I. *et al.* A Short Overview of Recent Developments on Antimicrobial Coatings Based on Phytosynthesized Metal Nanoparticles. *Coatings* **9**, doi:10.3390/coatings9120787 (2019).

7 Torres Dominguez, E., Nguyen, P. H., Hunt, H. K. & Mustapha, A. Antimicrobial Coatings for Food Contact Surfaces: Legal Framework, Mechanical Properties, and Potential Applications. *Comprehensive Reviews in Food Science and Food Safety* **18**, 1825-1858, doi:https://doi.org/10.1111/1541-4337.12502 (2019).

8 Kumaravel, V. *et al.* Antimicrobial TiO2 nanocomposite coatings for surfaces, dental and orthopaedic implants. *Chemical Engineering Journal* **416**, 129071, doi:https://doi.org/10.1016/j.cej.2021.129071 (2021).

9 BCC Publishing Staff. Antimicrobial Coatings: Global Markets to 2026 (Report Code CHM171A). *BCC Research*, Retrieved in November 2021 from https://www.bccresearch.com/ (2021).

10 Fujishima, A. & Honda, K. Electrochemical Photolysis of Water at a Semiconductor Electrode. *Nature* **238**, 37-38, doi:10.1038/238037a0 (1972).

11 Boyjoo, Y., Sun, H., Liu, J., Pareek, V. K. & Wang, S. A review on photocatalysis for air treatment: From catalyst development to reactor design. *Chemical Engineering Journal* **310**, 537-559, doi:https://doi.org/10.1016/j.cej.2016.06.090 (2017).

12 Ibhadon, A. O. & Fitzpatrick, P. Heterogeneous Photocatalysis: Recent Advances and Applications. *Catalysts* **3**, doi:10.3390/catal3010189 (2013).

13 Ahmed, S. N. & Haider, W. Heterogeneous photocatalysis and its potential applications in water and wastewater treatment: a review. *Nanotechnology* **29**, 342001, doi:10.1088/1361-6528/aac6ea (2018).

14 BCC Publishing Staff. Photocatalysts: Technologies and Global Markets (Report Code AVM069C). *BCC Research*, Retrieved in November 2021 from https://www.bccresearch.com/ (2021).

15 Li, Y. *et al. Visible-light-driven photocatalytic inactivation of MS2 by metal-free g-C3N4: Virucidal performance and mechanism*. Vol. 106 (2016).

16 Mamba, G. & Mishra, A. K. Graphitic carbon nitride (g-C3N4) nanocomposites: A new and exciting generation of visible light driven photocatalysts for environmental pollution remediation. *Applied Catalysis B: Environmental* **198**, 347-377, doi:https://doi.org/10.1016/j.apcatb.2016.05.052 (2016).

17 Lee, S.-Y. & Park, S.-J. TiO2 photocatalyst for water treatment applications. *Journal of Industrial and Engineering Chemistry* **19**, 1761-1769, doi:https://doi.org/10.1016/j.jiec.2013.07.012 (2013).

18 Krishna, V. *et al.* Contaminant-Activated Visible Light Photocatalysis. *Scientific Reports* **8**, 1894, doi:10.1038/s41598-018-19972-0 (2018).

19 Wang, W., Huang, G., Yu, J. C. & Wong, P. K. Advances in photocatalytic disinfection of bacteria: Development of photocatalysts and mechanisms. *Journal of Environmental Sciences* **34**, 232-247, doi:https://doi.org/10.1016/j.jes.2015.05.003 (2015).

20 Zheng, Q., Shen, H. & Shuai, D. Emerging investigators series: advances and challenges of graphitic carbon nitride as a visible-light-responsive photocatalyst for sustainable water purification. *Environmental Science: Water Research & Technology* **3**, 982-1001, doi:10.1039/C7EW00159B (2017).

21 Zhao, Z., Sun, Y. & Dong, F. Graphitic carbon nitride based nanocomposites: a review. *Nanoscale* **7**, 15-37, doi:10.1039/C4NR03008G (2015).

22 Adhikari, S. P. *et al.* One pot synthesis and characterization of Ag-ZnO/g-C3N4 photocatalyst with improved photoactivity and antibacterial properties. *Colloids and Surfaces A: Physicochemical and Engineering Aspects* **482**, 477-484, doi:https://doi.org/10.1016/j.colsurfa.2015.07.003 (2015).

23 Bing, W. *et al.* Visible-light-driven enhanced antibacterial and biofilm elimination activity of graphitic carbon nitride by embedded Ag nanoparticles. *Nano Research* **8**, 1648-1658, doi:10.1007/s12274-014-0654-1 (2015).

24 Ma, S., Zhan, S., Jia, Y., Shi, Q. & Zhou, Q. Enhanced disinfection application of Ag-modified g-C3N4 composite under visible light. *Applied Catalysis B: Environmental* **186**, 77-87, doi:https://doi.org/10.1016/j.apcatb.2015.12.051 (2016).

25 Raulio, M. *et al.* Destruction of Deinococcus geothermalis biofilm by photocatalytic ALD and sol-gel TiO2 surfaces. *Journal of Industrial Microbiology and Biotechnology* **33**, 261-268, doi:10.1007/s10295-005-0063-2 (2006).

26 Xia, D. *et al.* Enhanced photocatalytic inactivation of Escherichia coli by a novel Z-scheme g-C3N4/m-Bi2O4 hybrid photocatalyst under visible light: The role of reactive oxygen species. *Applied Catalysis B: Environmental* **214**, 23-33, doi:https://doi.org/10.1016/j.apcatb.2017.05.035 (2017).

27 Regmi, C., Joshi, B., Ray, S. K., Gyawali, G. & Pandey, R. P. Understanding Mechanism of Photocatalytic Microbial Decontamination of Environmental Wastewater. *Frontiers in chemistry* **6**, 33-33, doi:10.3389/fchem.2018.00033 (2018).

28 Zhang, C. *et al.* Visible-light-driven, water-surface-floating antimicrobials developed from graphitic carbon nitride and expanded perlite for water disinfection. *Chemosphere* **208**, 84-92, doi:https://doi.org/10.1016/j.chemosphere.2018.05.163 (2018).

29 National Renewable Energy Laboratory. Calculated from data in "Reference Air Mass 1.5 Spectra, ASTM G173-03 Reference Spectra". Retrieved in November 2021 from https://www.nrel.gov/grid/solar-resource/spectra-am2021.2025.html.

30 Dong, S. *et al.* Recent developments in heterogeneous photocatalytic water treatment using visible light-responsive photocatalysts: a review. *RSC Advances* **5**, 14610-14630, doi:10.1039/C4RA13734E (2015).

31 Moniz, S. J. A., Shevlin, S. A., Martin, D. J., Guo, Z.-X. & Tang, J. Visible-light driven heterojunction photocatalysts for water splitting – a critical review. *Energy & Environmental Science* **8**, 731-759, doi:10.1039/C4EE03271C (2015).

32 Acharya, R. & Parida, K. A review on TiO2/g-C3N4 visible-light- responsive photocatalysts for sustainable energy generation and environmental remediation. *Journal of Environmental Chemical Engineering* **8**, 103896, doi:https://doi.org/10.1016/j.jece.2020.103896 (2020).

33 You, J., Guo, Y., Guo, R. & Liu, X. A review of visible light-active photocatalysts for water disinfection: Features and prospects. *Chemical Engineering Journal* **373**, 624-641, doi:https://doi.org/10.1016/j.cej.2019.05.071 (2019).

34 Arunachalam, P. *et al.* Recent Developments in the Use of Heterogeneous Semiconductor Photocatalyst Based Materials for a Visible-Light-Induced Water-Splitting System—A Brief Review. *Catalysts* **11**, doi:10.3390/catal11020160 (2021).

35 Wang, X. *et al.* A metal-free polymeric photocatalyst for hydrogen production from water under visible light. *Nature Materials* **8**, 76, doi:10.1038/nmat2317

https://www.nature.com/articles/nmat2317#supplementary-information (2008).

36 Zhao, H. *et al.* Fabrication of atomic single layer graphitic-C3N4 and its high performance of photocatalytic disinfection under visible light irradiation. *Applied Catalysis B: Environmental* **152-153**, 46-50, doi:https://doi.org/10.1016/j.apcatb.2014.01.023 (2014).

37 Huang, J., Ho, W. & Wang, X. Metal-free disinfection effects induced by graphitic carbon nitride polymers under visible light illumination. *Chemical Communications* **50**, 4338-4340, doi:10.1039/C3CC48374F (2014).

38 Ding, N. *et al.* Enhanced inactivation of antibiotic-resistant bacteria isolated from secondary effluents by g-C3N4 photocatalysis. *Environmental Science and Pollution Research* **26**, 18730-18738, doi:10.1007/s11356-019-05080-7 (2019).

39 Thurston, J. H., Hunter, N. M., Wayment, L. J. & Cornell, K. A. Urea-derived graphitic carbon nitride (u-g-C3N4) films with highly enhanced antimicrobial and sporicidal activity. *Journal of Colloid and Interface Science* **505**, 910-918, doi:https://doi.org/10.1016/j.jcis.2017.06.089 (2017).

40 Wang, R. *et al.* Mechanism insight into rapid photocatalytic disinfection of Salmonella based on vanadate QDs-interspersed g-C3N4 heterostructures. *Applied Catalysis B: Environmental* **225**, 228-237, doi:https://doi.org/10.1016/j.apcatb.2017.11.060 (2018).

41 Zhang, C. *et al. Graphitic carbon nitride (g-C3N4)-based photocatalysts for water disinfection and microbial control: A review*. Vol. 214 (2018).

42 Ismael, M. A review on graphitic carbon nitride (g-C3N4) based nanocomposites: Synthesis, categories, and their application in photocatalysis. *Journal of Alloys and Compounds* **846**, 156446, doi:https://doi.org/10.1016/j.jallcom.2020.156446 (2020).

43 Wang, L. *et al.* Graphitic Carbon Nitride-Based Photocatalytic Materials: Preparation Strategy and Application. *ACS Sustainable Chemistry & Engineering* **8**, 16048-16085, doi:10.1021/acssuschemeng.0c05246 (2020).

44 Kessler, F. K. *et al.* Functional carbon nitride materials — design strategies for electrochemical devices. *Nature Reviews Materials* **2**, 17030, doi:10.1038/natrevmats.2017.30 (2017).

45 Wang, A., Wang, C., Fu, L., Wong-Ng, W. & Lan, Y. Recent Advances of Graphitic Carbon Nitride-Based Structures and Applications in Catalyst, Sensing, Imaging, and LEDs. *Nano-Micro Letters* **9**, 47, doi:10.1007/s40820-017-0148-2 (2017).

46 Lau, V. W.-h. *et al.* Rational design of carbon nitride photocatalysts by identification of cyanamide defects as catalytically relevant sites. *Nature Communications* **7**, 12165, doi:10.1038/ncomms12165

https://www.nature.com/articles/ncomms12165#supplementary-information (2016).

47 Zheng, Y., Lin, L., Wang, B. & Wang, X. Graphitic Carbon Nitride Polymers toward Sustainable Photoredox Catalysis. *Angewandte Chemie International Edition* **54**, 12868-12884, doi:https://doi.org/10.1002/anie.201501788 (2015).

48 Dong, G., Zhang, Y., Pan, Q. & Qiu, J. A fantastic graphitic carbon nitride (g-C3N4) material: Electronic structure, photocatalytic and photoelectronic properties. *Journal of Photochemistry and Photobiology C: Photochemistry Reviews* **20**, 33-50, doi:https://doi.org/10.1016/j.jphotochemrev.2014.04.002 (2014).

49 Lin, L.-S. *et al.* Graphitic-phase C3N4 nanosheets as efficient photosensitizers and pH-responsive drug nanocarriers for cancer imaging and therapy. *Journal of Materials Chemistry B* **2**, 1031-1037, doi:10.1039/C3TB21479F (2014).

50 Fidan, T. *et al.* Functionalized Graphitic Carbon Nitrides for Environmental and Sensing Applications. *Advanced Energy and Sustainability Research* **2**, 2000073, doi:https://doi.org/10.1002/aesr.202000073 (2021).

51 Thomas, A. *et al.* Graphitic carbon nitride materials: variation of structure and morphology and their use as metal-free catalysts. *Journal of Materials Chemistry* **18**, 4893-4908, doi:10.1039/B800274F (2008).

52 Zuluaga, S. *et al.* Structural band-gap tuning in g-C3N4. *Physical Chemistry Chemical Physics* **17**, 957-962, doi:10.1039/C4CP05164E (2015).

53 Yang, Z. *et al.* Tuning the band gap and the nitrogen content in carbon nitride materials by high temperature treatment at high pressure. *Carbon* **130**, 170-177, doi:https://doi.org/10.1016/j.carbon.2017.12.115 (2018).

54 Zhang, J. *et al.* Engineering monomer structure of carbon nitride for the effective and mild photooxidation reaction. *Carbon* **100**, 450-455, doi:https://doi.org/10.1016/j.carbon.2016.01.027 (2016).

55 Yu, H. *et al.* Alkali-Assisted Synthesis of Nitrogen Deficient Graphitic Carbon Nitride with Tunable Band Structures for Efficient Visible-Light-Driven Hydrogen Evolution. *Advanced Materials* **29**, 1605148, doi:10.1002/adma.201605148 (2017).

56 Sun, H., Cao, Y., Feng, L. & Chen, Y. Immobilizing photogenerated electrons from graphitic carbon nitride for an improved visible-light photocatalytic activity. *Scientific Reports* **6**, 22808, doi:10.1038/srep22808

https://www.nature.com/articles/srep22808#supplementary-information (2016).

57 Kroke, E. & Schwarz, M. Novel group 14 nitrides. *Coordination Chemistry Reviews* **248**, 493-532, doi:https://doi.org/10.1016/j.ccr.2004.02.001 (2004).

58 Kroke, E. *et al.* Tri-s-triazine derivatives. Part I. From trichloro-tri-s-triazine to graphitic C3N4 structures. *New Journal of Chemistry* **26**, 508-512, doi:10.1039/B111062B (2002).

59 Yang, B., Zhou, H., Zhang, X. & Zhao, M. Electron spin-polarization and band gap engineering in carbon-modified graphitic carbon nitrides. *Journal of Materials Chemistry C* **3**, 10886-10891, doi:10.1039/C5TC02423D (2015).

60 Zheng, Q. *et al.* Visible-Light-Responsive Graphitic Carbon Nitride: Rational Design and Photocatalytic Applications for Water Treatment. *Environmental Science & Technology* **50**, 12938-12948, doi:10.1021/acs.est.6b02579 (2016).

61 Mo, Z. *et al.* Synthesis of g-C3N4 at different temperatures for superior visible/UV photocatalytic performance and photoelectrochemical sensing of MB solution. *RSC Advances* **5**, 101552-101562, doi:10.1039/C5RA19586A (2015).

62 Zheng, Q., Shen, H. & Shuai, D. *Emerging Investigators Series: Advances and Challenges of Graphitic Carbon Nitride as a Visible-light-responsive Photocatalyst for Sustainable Water Purification*. Vol. 3 (2017).

63 Kang, S. *et al.* "Alternated cooling and heating" strategy enables rapid fabrication of highly-crystalline g-C3N4 nanosheets for efficient photocatalytic water purification under visible light irradiation. *Carbon* **137**, 19-30, doi:https://doi.org/10.1016/j.carbon.2018.05.010 (2018).

64 Kang, S. *et al.* Moderate Bacterial Etching Allows Scalable and Clean Delamination of g-C3N4 with Enriched Unpaired Electrons for Highly Improved Photocatalytic Water Disinfection. *ACS Applied Materials & Interfaces* **10**, 13796-13804, doi:10.1021/acsami.8b00007 (2018).

65 Choudhury, B. & Giri, P. K. Isotype heterostructure of bulk and nanosheets of graphitic carbon nitride for efficient visible light photodegradation of methylene blue. *RSC Advances* **6**, 24976-24984, doi:10.1039/C6RA00933F (2016).

66 Thurston, J., M Hunter, N. & Cornell, K. *Preparation and characterization of photoactive antimicrobial graphitic carbon nitride (g-C 3 N 4) films*. Vol. 6 (2016).

67 Wang, W. *et al.* Carbon nitride based photocatalysts for solar photocatalytic disinfection, can we go further? *Chemical Engineering Journal* **404**, 126540, doi:https://doi.org/10.1016/j.cej.2020.126540 (2021).

68 Yongsheng, N. *et al.* Graphitic carbon nitride (g-C3N4)-based nanostructured materials for photodynamic inactivation: Synthesis, efficacy and mechanism. *Chemical Engineering Journal* **404**, 126528, doi:10.1016/j.cej.2020.126528 (2020).

69 Wang, H., Huang, G., Chen, Z. & Li, W. Carbon Self-Doped Carbon Nitride Nanosheets with Enhanced Visible-Light Photocatalytic Hydrogen Production. *Catalysts* **8**, 366, doi:10.3390/catal8090366 (2018).

70 Zhang, W.-D., Su, F.-Y., Xun, C.-Q. & Yu, Y.-X. Carbon Self-Doping Induced Activation of n-π* Electronic Transitions of g-C3N4 Nanosheets for Efficient Photocatalytic H2 Evolution. *ChemCatChem* **8**, 3527-3535., doi:10.1002/cctc.201600928 (2016).

71 Mohamed, M. A. *et al.* Enhancement of visible light photocatalytic hydrogen evolution by bio-mimetic C-doped graphitic carbon nitride. *International Journal of Hydrogen Energy* **44**, 13098-13105, doi:https://doi.org/10.1016/j.ijhydene.2019.02.243 (2019).

72 Xiao, P., Jiang, D., Liu, T., Li, D. & Chen, M. Facile synthesis of carbon-doped g-C3N4 for enhanced photocatalytic hydrogen evolution under visible light. *Materials Letters* **212**, 111-113, doi:https://doi.org/10.1016/j.matlet.2017.10.079 (2018).

73 Liu, G., Xue, M., Liu, Q., Yang, H. & Zhou, Y. Facile synthesis of C-doped hollow spherical g-C3N4 from supramolecular self-assembly for enhanced photoredox water splitting. *International Journal of Hydrogen Energy* **44**, 25671-25679, doi:https://doi.org/10.1016/j.ijhydene.2019.08.056 (2019).

74 Chen, Z. *et al.* Gradual carbon doping of graphitic carbon nitride towards metal-free visible light photocatalytic hydrogen evolution. *Journal of Materials Chemistry A* **6**, 15310-15319, doi:10.1039/C8TA03303J (2018).

75 Shalom, M. *et al.* In Situ Formation of Heterojunctions in Modified Graphitic Carbon Nitride: Synthesis and Noble Metal Free Photocatalysis. *Chemistry of Materials* **26**, 5812-5818, doi:10.1021/cm503258z (2014).

76 Dong, G., Zhao, K. & Zhang, L. Carbon self-doping induced high electronic conductivity and photoreactivity of g-C3N4. *Chemical Communications* **48**, 6178-6180, doi:10.1039/C2CC32181E (2012).

77 Mohamed, M. A. *et al.* Constructing bio-templated 3D porous microtubular C-doped g-C3N4 with tunable band structure and enhanced charge carrier separation. *Applied Catalysis B: Environmental* **236**, 265-279, doi:https://doi.org/10.1016/j.apcatb.2018.05.037 (2018).

78 Ran, M. *et al.* Efficient and stable photocatalytic NO removal on C self-doped g-C3N4: Electronic structure and reaction mechanism. *Catalysis Science & Technology* **8**, 3387-3394., doi:10.1039/C8CY00887F (2018).

79 Xue, J., Huang, C., Xu, P., Wang, M. & Ma, S. Facile one-step synthesis of broken case-like carbon-doped g-C3N4 for photocatalytic degradation of benzene. *Applied Organometallic Chemistry* **33**, DOI 10.1002/aoc.4966., doi:10.1002/aoc.4966 (2019).

80 Zhang, P., Li, X., Shao, C. & Liu, Y. Hydrothermal synthesis of carbon-rich graphitic carbon nitride nanosheets for photoredox catalysis. *Journal of Materials Chemistry A* **3**, 3281-3284, doi:10.1039/C5TA00202H (2015).

81 Li, Z. *et al.* Metal-free carbon nitride with boosting photo-redox ability realized by the controlled carbon dopants. *Chemical Engineering Journal* **382**, 122657, doi:https://doi.org/10.1016/j.cej.2019.122657 (2020).

82 Li, Y. *et al.* Synthesis of carbon-doped g-C3N4 composites with enhanced visible-light photocatalytic activity. *Materials Letters* **137**, 281-284, doi:https://doi.org/10.1016/j.matlet.2014.08.142 (2014).

83 Bao, N. *et al.* Synthesis of porous carbon-doped g-C3N4 nanosheets with enhanced visible-light photocatalytic activity. *Applied Surface Science* **403**, 682-690, doi:https://doi.org/10.1016/j.apsusc.2017.01.256 (2017).

84 International Organisation for Standardization (ISO). ISO 14040:2006 Environmental Management – Life Cycle Assessment – Principles and Framework. https://www.iso.org/standard/37456.html (2006).

85 International Organisation for Standardization (ISO). ISO 14044:2006 Environmental Management – Life Cycle Assessment – Requirements and Guidelines. https://www.iso.org/standard/38498.html (2006).

86 Pati, P., McGinnis, S. & Vikesland, P. Life Cycle Assessment of "Green" Nanoparticle Synthesis Methods. *Environmental Engineering Science* **31**, doi:10.1089/ees.2013.0444 (2014).

87 Wu, F., Zhou, Z. & Hicks, A. L. Life Cycle Impact of Titanium Dioxide Nanoparticle Synthesis through Physical, Chemical, and Biological Routes. *Environmental Science & Technology* **53**, 4078-4087, doi:10.1021/acs.est.8b06800 (2019).

88 Pourzahedi, L. & Eckelman, M. J. Comparative life cycle assessment of silver nanoparticle synthesis routes. *Environmental Science: Nano* **2**, 361-369, doi:10.1039/C5EN00075K (2015).

89 Zhang, X. *et al.* Enhanced Photoresponsive Ultrathin Graphitic-Phase C3N4 Nanosheets for Bioimaging. *Journal of the American Chemical Society* **135**, 18-21, doi:10.1021/ja308249k (2013).

90 Yang, S. *et al.* Exfoliated Graphitic Carbon Nitride Nanosheets as Efficient Catalysts for Hydrogen Evolution Under Visible Light. *Advanced Materials* **25**, 2452-2456, doi:https://doi.org/10.1002/adma.201204453 (2013).

91 Gargano, J. W. *et al.* Mortality from selected diseases that can be transmitted by water – United States, 2003–2009. *Journal of Water and Health* **15**, 438-450, doi:10.2166/wh.2017.301 (2017).

92 Kramer, A., Schwebke, I. & Kampf, G. How long do nosocomial pathogens persist on inanimate surfaces? A systematic review. *BMC Infectious Diseases* **6**, 130, doi:10.1186/1471-2334-6-130 (2006).

93 Vankerckhoven, E. *et al.* Exploring the potential synergistic effects of chemical disinfectants and UV on the inactivation of free-living bacteria and treatment of biofilms in a pilot-scale system. *Water Science and Technology* **64**, 1247-1253, doi:10.2166/wst.2011.718 (2011).

94 Song, K., Mohseni, M. & Taghipour, F. Application of ultraviolet light-emitting diodes (UV-LEDs) for water disinfection: A review. *Water Research* **94**, 341-349, doi:https://doi.org/10.1016/j.watres.2016.03.003 (2016).

95 Li, X.-F. & Mitch, W. A. Drinking Water Disinfection Byproducts (DBPs) and Human Health Effects: Multidisciplinary Challenges and Opportunities. *Environmental Science & Technology* **52**, 1681-1689, doi:10.1021/acs.est.7b05440 (2018).

96 Li, Q. *et al.* Antimicrobial nanomaterials for water disinfection and microbial control: Potential applications and implications. *Water Research* **42**, 4591-4602, doi:https://doi.org/10.1016/j.watres.2008.08.015 (2008).

97 Duncan, T. V. Applications of nanotechnology in food packaging and food safety: Barrier materials, antimicrobials and sensors. *Journal of Colloid and Interface Science* **363**, 1-24, doi:https://doi.org/10.1016/j.jcis.2011.07.017 (2011).

98 Rutala, W. A., White, M. S., Gergen, M. F. & Weber, D. J. Bacterial Contamination of Keyboards: Efficacy and Functional Impact of Disinfectants. *Infection Control & Hospital Epidemiology* **27**, 372-377, doi:10.1086/503340 (2006).

99 McDonnell, G. & Russell, A. D. Antiseptics and Disinfectants: Activity, Action, and Resistance. *Clinical Microbiology Reviews* **12**, 147, doi:10.1128/CMR.12.1.147 (1999).

100 Chen, Y. S. *et al.* Efficacy of point-of-entry copper–silver ionisation system in eradicating Legionella pneumophila in a tropical tertiary care hospital: implications for hospitals contaminated with Legionella in both hot and cold water. *Journal of Hospital Infection* **68**, 152-158, doi:https://doi.org/10.1016/j.jhin.2007.10.020 (2008).

101 Birmele, M., O'Neal, J. & Roberts, M. *Disinfection of Spacecraft Potable Water Systems by Photocatalytic Oxidation Using UV-A Light Emitting Diodes*. (2011).

102 Lui, G. Y. *et al.* Photovoltaic powered ultraviolet and visible light-emitting diodes for sustainable point-of-use disinfection of drinking waters. *Science of The Total Environment* **493**, 185-196, doi:https://doi.org/10.1016/j.scitotenv.2014.05.104 (2014).

103 Zhang, C., Li, Y., Shuai, D., Shen, Y. & Wang, D. Progress and challenges in photocatalytic disinfection of waterborne Viruses: A review to fill current knowledge gaps. *Chemical Engineering Journal* **355**, 399-415, doi:https://doi.org/10.1016/j.cej.2018.08.158 (2019).

104 Xiao, X. *et al.* Impairment of Biofilm Formation by TiO2 Photocatalysis through Quorum Quenching. *Environmental Science & Technology* **50**, 11895-11902, doi:10.1021/acs.est.6b03134 (2016).

105 Fresno, F., Portela, R., Suárez, S. & Coronado, J. M. Photocatalytic materials: recent achievements and near future trends. *Journal of Materials Chemistry A* **2**, 2863-2884, doi:10.1039/C3TA13793G (2014).

106 Lee, K. M., Lai, C. W., Ngai, K. S. & Juan, J. C. Recent developments of zinc oxide based photocatalyst in water treatment technology: A review. *Water Research* **88**, 428-448, doi:https://doi.org/10.1016/j.watres.2015.09.045 (2016).

107 Loeb, S. K. *et al.* The Technology Horizon for Photocatalytic Water Treatment: Sunrise or Sunset? *Environmental Science & Technology* **53**, 2937-2947, doi:10.1021/acs.est.8b05041 (2019).

108 Xu, J., Wang, Z. & Zhu, Y. Enhanced Visible-Light-Driven Photocatalytic Disinfection Performance and Organic Pollutant Degradation Activity of Porous g-C3N4 Nanosheets. *ACS Applied Materials & Interfaces* **9**, 27727-27735, doi:10.1021/acsami.7b07657 (2017).

109 Darkwah, W. K. & Oswald, K. A. Photocatalytic Applications of Heterostructure Graphitic Carbon Nitride: Pollutant Degradation, Hydrogen Gas Production (water splitting), and CO2 Reduction. *Nanoscale Research Letters* **14**, 234, doi:10.1186/s11671-019-3070-3 (2019).

110 Liu, C. *et al.* Graphitic Hollow Carbon Nitride Nanosphere as a Novel Photochemical Internalization Agent for Targeted and Stimuli-responsive Cancer Therapy. *Nanoscale* **8**, 12570-12578., doi:10.1039/C5NR07719B (2015).

111 Mishra, A. *et al.* Graphitic carbon nitride (g–C3N4)–based metal-free photocatalysts for water splitting: A review. *Carbon* **149**, 693-721, doi:https://doi.org/10.1016/j.carbon.2019.04.104 (2019).

112 Ye, S., Wang, R., Wu, M.-Z. & Yuan, Y.-P. A review on g-C3N4 for photocatalytic water splitting and CO2 reduction. *Applied Surface Science* **358**, 15-27, doi:https://doi.org/10.1016/j.apsusc.2015.08.173 (2015).

113 Papailias, I. *et al.* Effect of processing temperature on structure and photocatalytic properties of g-C3N4. *Applied Surface Science* **358**, 278-286, doi:https://doi.org/10.1016/j.apsusc.2015.08.097 (2015).

114 Jiang, L. *et al.* Doping of graphitic carbon nitride for photocatalysis: A reveiw. *Applied Catalysis B: Environmental* **217**, 388-406, doi:https://doi.org/10.1016/j.apcatb.2017.06.003 (2017).

115 Ismael, M. & Wu, Y. A mini-review on the synthesis and structural modification of g-C3N4-based materials, and their applications in solar energy conversion and environmental remediation. *Sustainable Energy & Fuels* **3**, 2907-2925, doi:10.1039/C9SE00422J (2019).

116 Choudhury, B., Paul, K. K., Sanyal, D., Hazarika, A. & Giri, P. K. Evolution of Nitrogen-Related Defects in Graphitic Carbon Nitride Nanosheets Probed by Positron Annihilation and Photoluminescence Spectroscopy. *The Journal of Physical Chemistry C* **122**, 9209-9219, doi:10.1021/acs.jpcc.8b01388 (2018).

117 Da Silva, E. S. *et al.* β-Cyclodextrin as a Precursor to Holey C-Doped g-C3N4 Nanosheets for Photocatalytic Hydrogen Generation. *ChemSusChem* **11**, 2681-2694, doi:10.1002/cssc.201801003 (2018).

118 Panneri, S. *et al.* Photoregenerable, Bifunctional Granules of Carbon-Doped g-C3N4 as Adsorptive Photocatalyst for the Efficient Removal of Tetracycline Antibiotic. *ACS Sustainable Chemistry & Engineering* **5**, 1610-1618, doi:10.1021/acssuschemeng.6b02383 (2017).

119 Zhao, Z., Sun, Y., Dong, F., Zhang, Y. & Zhao, H. Template synthesis of carbon self-doped g-C3N4 with enhanced visible to near-infrared absorption and photocatalytic performance. *RSC Advances* **5**, 39549-39556, doi:10.1039/C5RA03433G (2015).

120 Zhu, S. & Wang, D. Photocatalysis: Basic Principles, Diverse Forms of Implementations and Emerging Scientific Opportunities. *Advanced Energy Materials* **7**, 1700841 (2017).

121 Chen, Y. *et al.* Naturally Occurring Sphalerite As a Novel Cost-Effective Photocatalyst for Bacterial Disinfection under Visible Light. *Environmental Science & Technology* **45**, 5689-5695, doi:10.1021/es200778p (2011).

122 Jun, Y.-S. *et al.* From Melamine-Cyanuric Acid Supramolecular Aggregates to Carbon Nitride Hollow Spheres. *Advanced Functional Materials* **23**, 3661-3667, doi:10.1002/adfm.201203732 (2013).

123 Shalom, M., Inal, S., Fettkenhauer, C., Neher, D. & Antonietti, M. Improving Carbon Nitride Photocatalysis by Supramolecular Preorganization of Monomers. *Journal of the American Chemical Society* **135**, 7118-7121, doi:10.1021/ja402521s (2013).

124 Reactive Oxygen Species (ROS) Detection Reagents. Report No. Product Information Sheet, (Molecular Probes, 2006).

125 Jin, C. *et al.* Near-infrared light photocatalysis and photothermy of carbon quantum dots and au nanoparticles loaded titania nanotube array. *Materials & Design* **177**, 107845, doi:https://doi.org/10.1016/j.matdes.2019.107845 (2019).

126 Sutton, S. in *Journal of Validation Technology* Vol. 17 42+ (2011).

127 Tenover, F. C. & Goering, R. V. Methicillin-resistant Staphylococcus aureus strain USA300: origin and epidemiology. *Journal of Antimicrobial Chemotherapy* **64**, 441-446, doi:10.1093/jac/dkp241 (2009).

128 Paulsen, I. T. *et al.* Role of Mobile DNA in the Evolution of Vancomycin-Resistant <em>Enterococcus faecalis</em&gt. *Science* **299**, 2071, doi:10.1126/science.1080613 (2003).

129 Cao, J. *et al.* Constructing nitrogen vacancy introduced g-C3N4 p-n homojunction for enhanced photocatalytic activity. *Journal of Environmental Chemical Engineering* **7**, 102984, doi:https://doi.org/10.1016/j.jece.2019.102984 (2019).

130 Fang, J., Fan, H., Li, M. & Long, C. Nitrogen self-doped graphitic carbon nitride as efficient visible light photocatalyst for hydrogen evolution. *Journal of Materials Chemistry A* **3**, 13819-13826, doi:10.1039/C5TA02257F (2015).

131 Sun, B.-w. *et al.* New complete assignment of X-ray powder diffraction patterns in graphitic carbon nitride using discrete Fourier transform and direct experimental evidence. *Physical Chemistry Chemical Physics* **19**, 26072-26084, doi:10.1039/C7CP05242A (2017).

132 Mu, T. *et al.* Synthesis and characterization of polyether structure carbon nitride. *Journal of Materials Research* **19**, 1736-1741, doi:10.1557/JMR.2004.0249 (2004).

133 Das, D. *et al.* Defect induced tuning of photoluminescence property in graphitic carbon nitride nanosheets through synthesis conditions. *Journal of Luminescence* **185**, 155-165, doi:https://doi.org/10.1016/j.jlumin.2017.01.007 (2017).

134 Chen, Y., Wang, B., Lin, S., Zhang, Y. & Wang, X. Activation of n → π* Transitions in Two-Dimensional Conjugated Polymers for Visible Light Photocatalysis. *The Journal of Physical Chemistry C* **118**, 29981-29989, doi:10.1021/jp510187c (2014).

135 Jiang, L. *et al.* A facile band alignment of polymeric carbon nitride isotype heterojunctions for enhanced photocatalytic tetracycline degradation. *Environmental Science: Nano* **5**, 2604-2617, doi:10.1039/C8EN00807H (2018).

136 Hu, S. *et al.* Band gap-tunable potassium doped graphitic carbon nitride with enhanced mineralization ability. *Dalton Transactions* **44**, 1084-1092, doi:10.1039/C4DT02658F (2015).

137 Zhao, J. *et al.* Novel band gap-tunable K–Na co-doped graphitic carbon nitride prepared by molten salt method. *Applied Surface Science* **332**, 625-630, doi:https://doi.org/10.1016/j.apsusc.2015.01.233 (2015).

138 Choudhury, B. & Choudhury, A. Oxygen defect dependent variation of band gap, Urbach energy and luminescence property of anatase, anatase–rutile mixed phase and of rutile phases of TiO2 nanoparticles. *Physica E: Low-dimensional Systems and Nanostructures* **56**, 364-371, doi:https://doi.org/10.1016/j.physe.2013.10.014 (2014).

139 Yaghoubi, H. *et al.* Toward a Visible Light-Driven Photocatalyst: The Effect of Midgap-States-Induced Energy Gap of Undoped TiO2 Nanoparticles. *ACS Catalysis* **5**, 327-335, doi:10.1021/cs501539q (2015).

140 Wu, P., Wang, J., Zhao, J., Guo, L. & Osterloh, F. E. Structure defects in g-C3N4 limit visible light driven hydrogen evolution and photovoltage. *Journal of Materials Chemistry A* **2**, 20338-20344, doi:10.1039/C4TA04100C (2014).

141 Schneider, J. *et al.* Understanding TiO2 Photocatalysis: Mechanisms and Materials. *Chemical Reviews* **114**, 9919-9986, doi:10.1021/cr5001892 (2014).

142 Nosaka, Y. & Nosaka, A. Y. Generation and Detection of Reactive Oxygen Species in Photocatalysis. *Chemical Reviews* **117**, 11302-11336, doi:10.1021/acs.chemrev.7b00161 (2017).

143 Wang, W. *et al.* Visible-Light-Driven Photocatalytic Inactivation of E. coli K-12 by Bismuth Vanadate Nanotubes: Bactericidal Performance and Mechanism. *Environmental Science & Technology* **46**, 4599-4606, doi:10.1021/es2042977 (2012).

144 Ng, T. W. *et al.* Visible-light-driven photocatalytic inactivation of Escherichia coli by magnetic Fe2O3–AgBr. *Water Research* **90**, 111-118, doi:https://doi.org/10.1016/j.watres.2015.12.022 (2016).

145 Shi, H. *et al.* Defects Promote Ultrafast Charge Separation in Graphitic Carbon Nitride for Enhanced Visible-Light-Driven CO2 Reduction Activity. *Chemistry – A European Journal* **25**, 5028-5035, doi:10.1002/chem.201805923 (2019).

146 Murugesan, P., Moses, J. A. & Anandharamakrishnan, C. Photocatalytic disinfection efficiency of 2D structure graphitic carbon nitride-based nanocomposites: a review. *Journal of Materials Science* **54**, 12206-12235, doi:10.1007/s10853-019-03695-2 (2019).

147 Fu, P. P., Xia, Q., Hwang, H.-M., Ray, P. C. & Yu, H. Mechanisms of nanotoxicity: Generation of reactive oxygen species. *Journal of Food and Drug Analysis* **22**, 64-75, doi:10.1016/j.jfda.2014.01.005 (2014).

148 Azeez, F. *et al.* The effect of surface charge on photocatalytic degradation of methylene blue dye using chargeable titania nanoparticles. *Scientific Reports* **8**, 7104, doi:10.1038/s41598-018-25673-5 (2018).

149 Teng, Z. *et al.* Edge-Functionalized g-C3N4 Nanosheets as a Highly Efficient Metal-free Photocatalyst for Safe Drinking Water. *Chem* **5**, 664-680, doi:https://doi.org/10.1016/j.chempr.2018.12.009 (2019).

150 Painter, K. L. *et al.* Staphylococcus aureus Adapts to Oxidative Stress by Producing H₂O₂-Resistant Small-Colony Variants via the SOS Response. *Infection and Immunity* **83**, 1830, doi:10.1128/IAI.03016-14 (2015).

151 BCC Publishing Staff. Photocatalysts: Technologies and Global Markets (Report Code AVM069C). *BCC Research*, Retrieved in November 2021 from https://www.bccresearch.com/ (2020).

152 Miller, T. S. *et al.* Carbon nitrides: synthesis and characterization of a new class of functional materials. *Physical Chemistry Chemical Physics* **19**, 15613-15638, doi:10.1039/C7CP02711G (2017).

153 Aquino de Carvalho, N. *et al.* Using C-Doping to Identify Photocatalytic Properties of Graphitic Carbon Nitride That Govern Antibacterial Efficacy. *ACS ES&T Water*, doi:10.1021/acsestwater.0c00053 (2020).

154 Liu, H. *et al.* Defective engineering in graphitic carbon nitride nanosheet for efficient photocatalytic pathogenic bacteria disinfection. *Applied Catalysis B: Environmental* **261**, 118201, doi:https://doi.org/10.1016/j.apcatb.2019.118201 (2020).

155 Zhang, G., Zhang, J., Zhang, M. & Wang, X. Polycondensation of thiourea into carbon nitride semiconductors as visible light photocatalysts. *Journal of Materials Chemistry* **22**, 8083-8091, doi:10.1039/C2JM00097K (2012).

156 Pawar, R. C. *et al.* Room-temperature synthesis of nanoporous 1D microrods of graphitic carbon nitride (g-C3N4) with highly enhanced photocatalytic activity and stability. *Scientific Reports* **6**, 31147, doi:10.1038/srep31147 (2016).

157 Zheng, Y., Liu, J., Liang, J., Jaroniec, M. & Qiao, S. Z. Graphitic carbon nitride materials: controllable synthesis and applications in fuel cells and photocatalysis. *Energy & Environmental Science* **5**, 6717-6731, doi:10.1039/C2EE03479D (2012).

158 Zhang, J., Chen, Y. & Wang, X. Two-dimensional covalent carbon nitride nanosheets: synthesis, functionalization, and applications. *Energy & Environmental Science* **8**, 3092-3108, doi:10.1039/C5EE01895A (2015).

159 Yadav, P., Nishanthi, S. T., Purohit, B., Shanavas, A. & Kailasam, K. Metal-free visible light photocatalytic carbon nitride quantum dots as efficient antibacterial agents: An insight study. *Carbon* **152**, 587-597, doi:https://doi.org/10.1016/j.carbon.2019.06.045 (2019).

160 Zhou, C. *et al.* Template-free large-scale synthesis of g-C3N4 microtubes for enhanced visible light-driven photocatalytic H2 production. *Nano Research* **11**, 3462-3468, doi:10.1007/s12274-018-2003-2 (2018).

161 Zheng, Y., Zhang, Z. & Li, C. A comparison of graphitic carbon nitrides synthesized from different precursors through pyrolysis. *Journal of Photochemistry and Photobiology A: Chemistry* **332**, 32-44, doi:https://doi.org/10.1016/j.jphotochem.2016.08.005 (2017).

162 Pourzahedi, L. & Eckelman, M. J. Environmental Life Cycle Assessment of Nanosilver-Enabled Bandages. *Environmental Science & Technology* **49**, 361-368, doi:10.1021/es504655y (2015).

163 Walser, T., Demou, E., Lang, D. J. & Hellweg, S. Prospective Environmental Life Cycle Assessment of Nanosilver T-Shirts. *Environmental Science & Technology* **45**, 4570-4578, doi:10.1021/es2001248 (2011).

164 Eckelman, M. J., Mauter, M. S., Isaacs, J. A. & Elimelech, M. New Perspectives on Nanomaterial Aquatic Ecotoxicity: Production Impacts Exceed Direct Exposure Impacts for Carbon Nanotoubes. *Environmental Science & Technology* **46**, 2902-2910, doi:10.1021/es203409a (2012).

165 Meyer, D. E., Curran, M. A. & Gonzalez, M. A. An examination of silver nanoparticles in socks using screening-level life cycle assessment. *Journal of Nanoparticle Research* **13**, 147-156, doi:10.1007/s11051-010-0013-4 (2011).

166 Falinski, M. M. *et al.* A framework for sustainable nanomaterial selection and design based on performance, hazard, and economic considerations. *Nature Nanotechnology* **13**, 708-714, doi:10.1038/s41565-018-0120-4 (2018).

167 Gilbertson, L. M. *et al.* Guiding the design space for nanotechnology to advance sustainable crop production. *Nature Nanotechnology* **15**, 801-810, doi:10.1038/s41565-020-0706-5 (2020).

168 Gilbertson, L. M., Busnaina, A. A., Isaacs, J. A., Zimmerman, J. B. & Eckelman, M. J. Life Cycle Impacts and Benefits of a Carbon Nanotube-Enabled Chemical Gas Sensor. *Environmental Science & Technology* **48**, 11360-11368, doi:10.1021/es5006576 (2014).

169 Hicks, A. L., Gilbertson, L. M., Yamani, J. S., Theis, T. L. & Zimmerman, J. B. Life Cycle Payback Estimates of Nanosilver Enabled Textiles under Different Silver Loading, Release, And Laundering Scenarios Informed by Literature Review. *Environmental Science & Technology* **49**, 7529-7542, doi:10.1021/acs.est.5b01176 (2015).

170 National Renewable Energy Laboratory. U.S. Life Cycle Inventory Database. Retrieved in September 2021 from https://www.nrel.gov/lci/ (2012).

171 Long Trail Sustainability (LTS). DATASMART Life Cycle Inventory Package. Retrieved in September 2021 from https://ltsexperts.com/services/software/datasmart-life-cycle-inventory/ (2020).

172 Wernet, G. *et al.* The ecoinvent database version 3 (part I): overview and methodology. *The International Journal of Life Cycle Assessment* **21**, 1218-1230, doi:10.1007/s11367-016-1087-8 (2016).

173 Bare, J. C. Tool for the Reduction and Assessment of Chemical and Other Environmental Impacts (TRACI) TRACI version 2.1 User's Guide. *US EPA Office of Research and Development, Washington, DC, EPA/600/R-12/554* (2014).

174 Yan, Q. *et al.* Facile synthesis and superior photocatalytic and electrocatalytic performances of porous B-doped g-C3N4 nanosheets. *Journal of Materials Science & Technology* **34**, 2515-2520, doi:https://doi.org/10.1016/j.jmst.2017.06.018 (2018).

175 Peng, D. *et al.* One-Pot Synthesis of Boron Carbon Nitride Nanosheets for Facile and Efficient Heavy Metal Ions Removal. *ACS Sustainable Chemistry & Engineering* **6**, 11685-11694, doi:10.1021/acssuschemeng.8b01951 (2018).

176 Huang, Z.-F. *et al.* Carbon nitride with simultaneous porous network and O-doping for efficient solar-energy-driven hydrogen evolution. *Nano Energy* **12**, 646-656, doi:https://doi.org/10.1016/j.nanoen.2015.01.043 (2015).

177 U.S. Energy Information Administration. Electricity explained: Electricity in the United States. Retrieved in March 2022 from https://www.eia.gov/energyexplained/electricity/electricity-in-the-us.php (2022).

178 Lin, Q. *et al.* Efficient synthesis of monolayer carbon nitride 2D nanosheet with tunable concentration and enhanced visible-light photocatalytic activities. *Applied Catalysis B: Environmental* **163**, 135-142, doi:https://doi.org/10.1016/j.apcatb.2014.07.053 (2015).

179 U.S. Environmental Protection Agency, EPA 430-R-22-003. EPA (2022) Inventory of U.S. Greenhouse Gas Emissions and Sinks: 1990-2020. https://www.epa.gov/ghgemissions/inventory-us-greenhouse-gas-emissions-and-sinks-1990-2020 (2022).

180 U.S. Census Bureau. Annual Estimates of the Population for the United States. (2021).

181 Pacific Gas and Electric Company. 2020 Power Content Label. Retrieved in March 2022 from https://www.pge.com/pge_global/common/pdfs/your-account/your-bill/understand-your-bill/bill-inserts/2021/1021-PowerContent.pdf (2020).

182 Shibafuchi, H. S., Masanori; Nitta, Hidenori; Yoshida, Masahiko. Process for producing cyanamide from calcium cyanamide. *European Patent Office, EP0347045B1* (1989).

183 Nyangaresi, P. O. *et al.* Comparison of UV-LED photolytic and UV-LED/TiO2 photocatalytic disinfection for Escherichia coli in water. *Catalysis Today* **335**, 200-207, doi:https://doi.org/10.1016/j.cattod.2018.11.015 (2019).

184 Xiong, P. & Hu, J. Inactivation/reactivation of antibiotic-resistant bacteria by a novel UVA/LED/TiO2 system. *Water Research* **47**, 4547-4555, doi:https://doi.org/10.1016/j.watres.2013.04.056 (2013).

185 Thorlabs. Mounted LEDs. Retrieved in March 2022 from https://www.thorlabs.com/newgrouppage2029.cfm?objectgroup_id=2692.

186 Burda, C. *et al.* Enhanced Nitrogen Doping in TiO2 Nanoparticles. *Nano Letters* **3**, 1049-1051, doi:10.1021/nl034332o (2003).

187 Egerton, T. A. UV-Absorption—The Primary Process in Photocatalysis and Some Practical Consequences. *Molecules* **19**, doi:10.3390/molecules191118192 (2014).

188 U.S. Environmental Protection Agency. National Primary Drinking Water Regulations: Long Term 2 Enhanced Surface Water Treatment Rule: Final Rule. 40 CFR Parts 9, 141 and 142. https://www.epa.gov/dwreginfo/long-term-2-enhanced-surface-water-treatment-rule-documents?msclkid=4e8d4bacd0d611ecafa578bcb8855ea8855 (2006).

189 Jones, C. H., Shilling, E. G., Linden, K. G. & Cook, S. M. Life Cycle Environmental Impacts of Disinfection Technologies Used in Small Drinking Water Systems. *Environmental Science & Technology* **52**, 2998-3007, doi:10.1021/acs.est.7b04448 (2018).

190 U.S. Environmental Protection Agency. Surface Water Treatment Rules (1989-2006). Retrieved in July 2022 from https://www.epa.gov/dwreginfo/surface-water-treatment-rules.

191 Zhang, L., Lou, J., Zhang, W., Wu, C. & Jin, Z. Bacteria killing in ICU associated infections: antibacterial nanosheets as disinfectant. *RSC Advances* **8**, 278-283, doi:10.1039/C7RA12148B (2018).

192 Li, G. *et al.* Enhanced visible-light-driven photocatalytic inactivation of Escherichia coli using g-C3N4/TiO2 hybrid photocatalyst synthesized using a hydrothermal-calcination approach. *Water Research* **86**, 17-24, doi:https://doi.org/10.1016/j.watres.2015.05.053 (2015).

193 Binas, V., Venieri, D., Kotzias, D. & Kiriakidis, G. Modified TiO2 based photocatalysts for improved air and health quality. *Journal of Materiomics* **3**, 3-16, doi:https://doi.org/10.1016/j.jmat.2016.11.002 (2017).

194 Achouri, F. *et al.* Comparative study of Gram-negative bacteria response to solar photocatalytic inactivation. *Environmental Science and Pollution Research*, doi:10.1007/s11356-018-2435-y (2018).

195 Cho, M., Chung, H., Choi, W. & Yoon, J. Different Inactivation Behaviors of MS-2 Phage and Escherichia coli in TiO₂ Photocatalytic Disinfection. *Applied and Environmental Microbiology* **71**, 270 (2005).

196 Josset, S., Taranto, J., Keller, N., Keller, V. & Lett, M.-C. Photocatalytic Treatment of Bioaerosols: Impact of the Reactor Design. *Environmental Science & Technology* **44**, 2605-2611, doi:10.1021/es902997v (2010).

197 Zhang, C., Li, Y., Wang, C. & Zheng, X. Different inactivation behaviors and mechanisms of representative pathogens (Escherichia coli bacteria, human adenoviruses and Bacillus subtilis spores) in g-C3N4-based metal-free visible-light-enabled photocatalytic disinfection. *Science of The Total Environment* **755**, 142588, doi:https://doi.org/10.1016/j.scitotenv.2020.142588 (2021).

198 Zhang, C., Li, Y., Zhang, W., Wang, P. & Wang, C. Metal-free virucidal effects induced by g-C3N4 under visible light irradiation: Statistical analysis and parameter optimization.

Chemosphere **195**, 551-558, doi:https://doi.org/10.1016/j.chemosphere.2017.12.122 (2018).

199 Zhang, C., Zhang, M., Li, Y. & Shuai, D. Visible-light-driven photocatalytic disinfection of human adenovirus by a novel heterostructure of oxygen-doped graphitic carbon nitride and hydrothermal carbonation carbon. *Applied Catalysis B: Environmental* **248**, 11-21, doi:https://doi.org/10.1016/j.apcatb.2019.02.009 (2019).

200 Cheng, R., Shen, L.-j., Yu, J.-h., Xiang, S.-y. & Zheng, X. Photocatalytic Inactivation of Bacteriophage f2 with Ag3PO4/g-C3N4 Composite under Visible Light Irradiation: Performance and Mechanism. *Catalysts* **8**, doi:10.3390/catal8100406 (2018).

201 McAllister, M. J. *et al.* Single sheet functionalized graphene by oxidation and thermal expansion of graphite. *Chem Mater* **19**, 4396-4404 (2007).

202 Guo, H.-L., Su, P., Kang, X. & Ning, S.-K. Synthesis and characterization of nitrogen-doped graphene hydrogels by hydrothermal route with urea as reducing-doping agents. *Journal of Materials Chemistry A* **1**, 2248-2255 (2013).

203 Wang, Y., Aquino de Carvalho, N., Tan, S. & Gilbertson, L. M. Leveraging electrochemistry to uncover the role of nitrogen in the biological reactivity of nitrogen-doped graphene. *Environmental Science: Nano* **6**, 3525-3538, doi:10.1039/C9EN00802K (2019).

204 Marks, R. & Doudrick, K. Photocatalytic reduction of chlorite in water using bismuth vanadate (BiVO4): effect of irradiance conditions and presence of oxalate on the reactivity and by-product selectivity. *Environmental Science: Water Research & Technology* **5**, 2015-2026, doi:10.1039/C9EW00636B (2019).

205 He, N. *et al.* Enhanced photocatalytic disinfection of Escherichia coli K-12 by porous g-C3N4 nanosheets: Combined effect of photo-generated and intracellular ROSs. *Chemosphere* **235**, 1116-1124, doi:https://doi.org/10.1016/j.chemosphere.2019.07.007 (2019).

206 May, H. Pyrolysis of melamine. *Journal of Applied Chemistry* **9**, 340-344, doi:https://doi.org/10.1002/jctb.5010090608 (1959).

207 Li, X. *et al.* Preparation and characterization of graphitic carbon nitride through pyrolysis of melamine. *Applied Physics A* **94**, 387-392 (2009).

208 She, D.-M., Yu, H.-L., Huang, Q.-L., Li, F.-M. & Li, C.-J. Liquid-phase synthesis of cyanuric acid from urea. *Molecules* **15**, 1898-1902, doi:10.3390/molecules15031898 (2010).

209 Huthmacher, K. & Most, D. Cyanuric Acid and Cyanuric Chloride. doi:10.1002/14356007.a08_191 (2000).

210 Schaber, P. M. *et al.* Thermal decomposition (pyrolysis) of urea in an open reaction vessel. *Thermochimica Acta* **424**, 131-142, doi:https://doi.org/10.1016/j.tca.2004.05.018 (2004).

211 Adcock, N. J. *et al.* The use of bacteriophages of the family Cystoviridae as surrogates for H5N1 highly pathogenic avian influenza viruses in persistence and inactivation studies. *J. Environ. Sci. Health, Part A: Toxic/Hazard. Subst. Environ. Eng.* **44**, 1362-1366, doi:10.1080/10934520903217054 (2009).

212 Liu, J., Zhang, T., Wang, Z., Dawson, G. & Chen, W. Simple pyrolysis of urea into graphitic carbon nitride with recyclable adsorption and photocatalytic activity. *Journal of Materials Chemistry* **21**, 14398-14401, doi:10.1039/C1JM12620B (2011).

213 CDC. *Ebola Outbreaks 2000-2014*, <(http://www.cdc.gov/vhf/ebola/outbreaks/history/summaries.html)> (

214 Hastings, D. L. *et al.* Outbreak of Middle East Respiratory Syndrome at Tertiary Care Hospital, Jeddah, Saudi Arabia, 2014. *Emerging Infectious Diseases* **22**, 794-801, doi:10.3201/eid2205.151797 (2016).

215 Moon-Woo, S. *et al.* Microevolution of Outbreak-Associated Middle East Respiratory Syndrome Coronavirus, South Korea, 2015. *Emerging Infectious Disease journal* **22**, 327, doi:10.3201/eid2202.151700 (2016).

216 Ying-Hen, H., Cathy, W. S. C. & Sze-Bi, H. SARS Outbreak, Taiwan, 2003. *Emerging Infectious Disease journal* **10**, 201, doi:10.3201/eid1002.030515 (2004).

217 Núñez, J. J. *et al.* Hantavirus Infections among Overnight Visitors to Yosemite National Park, California, USA, 2012. *Emerging Infectious Diseases* **20**, 386-393, doi:10.3201/eid2003.131581 (2014).

218 WHO. *Lassa Fever – Nigeria*, <(http://www.who.int/csr/don/27-may-2016-lassa-fever-nigeria/en/)> (2016).

219 Bibby, K., Aquino de Carvalho, N. & Wigginton, K. Research Needs for Wastewater Handling in Virus Outbreak Response. *Environmental Science & Technology*, doi:10.1021/acs.est.6b06492 (2017).

220 ABSA. *Risk Group Database*, <(https://my.absa.org/tiki-index.php?page=Riskgroups)> (

221 Wigginton, K. R., Ye, Y. & Ellenberg, R. M. Emerging investigators series: the source and fate of pandemic viruses in the urban water cycle. *Environmental Science: Water Research & Technology* **1**, 735-746, doi:10.1039/C5EW00125K (2015).

222 Ye, Y., Ellenberg, R. M., Graham, K. E. & Wigginton, K. R. Survivability, Partitioning, and Recovery of Enveloped Viruses in Untreated Municipal Wastewater. *Environmental Science & Technology* **50**, 5077-5085, doi:10.1021/acs.est.6b00876 (2016).

223 Bibby, K. *et al.* Persistence of Ebola Virus in Sterilized Wastewater. *Environmental Science & Technology Letters* **2**, 245-249, doi:10.1021/acs.estlett.5b00193 (2015).

224 Adcock, N. J. *et al.* The use of bacteriophages of the family Cystoviridae as surrogates for H5N1 highly pathogenic avian influenza viruses in persistence and inactivation studies. *Journal of Environmental Science and Health, Part A* **44**, 1362-1366, doi:10.1080/10934520903217054 (2009).

225 Casanova, L., Rutala, W. A., Weber, D. J. & Sobsey, M. D. Survival of surrogate coronaviruses in water. *Water Research* **43**, 1893-1898, doi:http://dx.doi.org/10.1016/j.watres.2009.02.002 (2009).

226 Phillpotts, R. J., Thomas, R. J., Beedham, R. J., Platt, S. D. & Vale, C. A. The Cystovirus phi6 as a simulant for Venezuelan equine encephalitis virus. *Aerobiologia* **26**, 301-309, doi:10.1007/s10453-010-9166-y (2010).

227 Casanova, L. M. & Weaver, S. R. Inactivation of an Enveloped Surrogate Virus in Human Sewage. *Environmental Science & Technology Letters* **2**, 76-78, doi:10.1021/acs.estlett.5b00029 (2015).

228 Vidaver, A. K., Koski, R. K. & Van Etten, J. L. Bacteriophage φ6: a Lipid-Containing Virus of Pseudomonas phaseolicola. *Journal of Virology* **11**, 799-805 (1973).

229 Frilander, M., Poranen, M. & Bamford, D. H. The large genome segment of dsRNA bacteriophage phi6 is the key regulator in the in vitro minus and plus strand synthesis. *RNA* **1**, 510-518 (1995).

230 Gonzalez, C. F., Langenberg, W. G., Van Etten, J. L. & Vidaver, A. K. Ultrastructure of Bacteriophage φ6: Arrangement of the Double-stranded RNA and Envelope. *Journal of General Virology* **35**, 353-359, doi:doi:10.1099/0022-1317-35-2-353 (1977).

231 Etten, J. V., Lane, L., Gonzalez, C., Partridge, J. & Vidaver, A. Comparative properties of bacteriophage phi6 and phi6 nucleocapsid. *Journal of Virology* **18**, 652-658 (1976).

232 Sinclair, J. F., Tzagoloff, A., Levine, D. & Mindich, L. Proteins of bacteriophage phi6. *Journal of Virology* **16**, 685-695 (1975).

233 Turgeon, N., Toulouse, M.-J., Martel, B., Moineau, S. & Duchaine, C. Comparison of Five Bacteriophages as Models for Viral Aerosol Studies. *Applied and Environmental Microbiology* **80**, 4242-4250, doi:10.1128/AEM.00767-14 (2014).

234 Casanova, L. M. & Weaver, S. R. Evaluation of eluents for the recovery of an enveloped virus from hands by whole-hand sampling. *Journal of applied microbiology* **118**, 1210-1216, doi:10.1111/jam.12777 (2015).

235 Titcombe Lee, M., Pruden, A. & Marr, L. C. Partitioning of Viruses in Wastewater Systems and Potential for Aerosolization. *Environmental Science & Technology Letters* **3**, 210-215, doi:10.1021/acs.estlett.6b00105 (2016).

236 Wei, H. *et al.* Three-Dimensional Structure of the Enveloped Bacteriophage Φ12: An Incomplete T=13 Lattice Is Superposed on an Enclosed T=1 Shell. *PLoS One* **4**, e6850, doi:10.1371/journal.pone.0006850 (2009).

237 ATCC. <https://www.atcc.org/> (

238 DSMZ. *Pseudomonas phage phi6* <https://www.dsmz.de/catalogues/details/culture/DSM-21518.html> (2017).

239 Sands, J. A. The phospholipid composition of bacteriophage φ6. *Biochemical and Biophysical Research Communications* **55**, 111-116, doi:http://dx.doi.org/10.1016/S0006-291X(73)80066-X (1973).

240 Mindich, L. *et al.* Isolation of Additional Bacteriophages with Genomes of Segmented Double-Stranded RNA. *Journal of Bacteriology* **181**, 4505-4508 (1999).

241 Poranen, M. M. & Tuma, R. Self-assembly of double-stranded RNA bacteriophages. *Virus Research* **101**, 93-100, doi:http://dx.doi.org/10.1016/j.virusres.2003.12.009 (2004).

242 Laurinavičius, S., Käkelä, R., Bamford, D. H. & Somerharju, P. The origin of phospholipids of the enveloped bacteriophage phi6. *Virology* **326**, 182-190, doi:http://dx.doi.org/10.1016/j.virol.2004.05.021 (2004).

243 Stitt, B. L. & Mindich, L. Morphogenesis of bacteriophage φ6. A presumptive viral membrane precursor. *Virology* **127**, 446-458, doi:http://dx.doi.org/10.1016/0042-6822(83)90157-5 (1983).

244 de Haas, F., Paatero, A. O., Mindich, L., Bamford, D. H. & Fuller, S. D. A symmetry mismatch at the site of RNA packaging in the polymerase complex of dsRNA bacteriophage φ61. *Journal of Molecular Biology* **294**, 357-372, doi:http://dx.doi.org/10.1006/jmbi.1999.3260 (1999).

245 Piercy, T. J., Smither, S. J., Steward, J. A., Eastaugh, L. & Lever, M. S. The survival of filoviruses in liquids, on solid substrates and in a dynamic aerosol. *Journal of Applied Microbiology* **109**, 1531-1539, doi:10.1111/j.1365-2672.2010.04778.x (2010).

246 Sinclair, R. G., Rose, J. B., Hashsham, S. A., Gerba, C. P. & Haas, C. N. Criteria for Selection of Surrogates Used To Study the Fate and Control of Pathogens in the Environment. *Applied and Environmental Microbiology* **78**, 1969-1977, doi:10.1128/AEM.06582-11 (2012).

247 Brown, J. D., Goekjian, G., Poulson, R., Valeika, S. & Stallknecht, D. E. Avian influenza virus in water: Infectivity is dependent on pH, salinity and temperature. *Veterinary Microbiology* **136**, 20-26, doi:http://dx.doi.org/10.1016/j.vetmic.2008.10.027 (2009).

248 Stallknecht, D. E., Kearney, M. T., Shane, S. M. & Zwank, P. J. Effects of pH, Temperature, and Salinity on Persistence of Avian Influenza Viruses in Water. *Avian Diseases* **34**, 412-418, doi:10.2307/1591429 (1990).

249 Keeler, S. P., Dalton, M. S., Cressler, A. M., Berghaus, R. D. & Stallknecht, D. E. Abiotic Factors Affecting the Persistence of Avian Influenza Virus in Surface Waters of Waterfowl Habitats. *Applied and Environmental Microbiology* **80**, 2910-2917, doi:10.1128/aem.03790-13 (2014).

250 Hardestam, J. *et al.* Ex Vivo Stability of the Rodent-Borne Hantaan Virus in Comparison to That of Arthropod-Borne Members of the Bunyaviridae Family. *Applied and Environmental Microbiology* **73**, 2547-2551, doi:10.1128/aem.02869-06 (2007).

251 Domanska-Blicharz, K. *et al.* H5N1 High Pathogenicity Avian Influenza Virus Survival in Different Types of Water. *Avian Diseases* **54**, 734-737 (2010).

252 Brown, J. D., Swayne, D. E., Cooper, R. J., Burns, R. E. & Stallknecht, D. E. Persistence of H5 and H7 Avian Influenza Viruses in Water. *Avian Diseases* **51**, 285-289, doi:10.1637/7636-042806R.1 (2007).

253 Lebarbenchon, C. *et al.* Reassortant influenza A viruses in wild duck populations: effects on viral shedding and persistence in water. *Proceedings of the Royal Society B: Biological Sciences* **279**, 3967-3975, doi:10.1098/rspb.2012.1271 (2012).

254 Brown, J., Stallknecht, D., Lebarbenchon, C. & Swayne, D. Survivability of Eurasian H5N1 Highly Pathogenic Avian Influenza Viruses in Water Varies Between Strains. *Avian Diseases* **58**, 453-457, doi:10.1637/10741-120513-ResNote.1 (2014).

255 Gundy, P. M., Gerba, C. P. & Pepper, I. L. Survival of Coronaviruses in Water and Wastewater. *Food and Environmental Virology* **1**, 10-14, doi:10.1007/s12560-008-9001-6 (2008).

256 Fischer, R. *et al.* Ebola Virus Stability on Surfaces and in Fluids in Simulated Outbreak Environments. *Emerging Infectious Diseases* **21**, 1243-1246, doi:10.3201/eid2107.150253 (2015).

257 Bøtner, A. Survival of Aujeszky's disease virus in slurry at various temperatures. *Veterinary Microbiology* **29**, 225-235, doi:http://dx.doi.org/10.1016/0378-1135(91)90130-8 (1991).

258 Bøtner, A. & Belsham, G. J. Virus survival in slurry: Analysis of the stability of foot-and-mouth disease, classical swine fever, bovine viral diarrhoea and swine influenza viruses. *Veterinary Microbiology* **157**, 41-49, doi:http://dx.doi.org/10.1016/j.vetmic.2011.12.010 (2012).

259 Casson, L. W., Sorber, C. A., Palmer, R. H., Enrico, A. & Gupta, P. HIV Survivability in Wastewater. *Water Environment Research* **64**, 213-215 (1992).

260 Dublineau, A. *et al.* Persistence of the 2009 Pandemic Influenza A (H1N1) Virus in Water and on Non-Porous Surface. *PLoS One* **6**, e28043, doi:10.1371/journal.pone.0028043 (2011).

261 Emmoth, E., Ottoson, J., Albihn, A., Belák, S. & Vinnerås, B. Ammonia Disinfection of Hatchery Waste for Elimination of Single-Stranded RNA Viruses. *Applied and Environmental Microbiology* **77**, 3960-3966, doi:10.1128/AEM.02990-10 (2011).

262 Kallio, E. R. *et al.* Prolonged survival of Puumala hantavirus outside the host: evidence for indirect transmission via the environment. *Journal of General Virology* **87**, 2127-2134, doi:doi:10.1099/vir.0.81643-0 (2006).

263 Keeler, S. P., Lebarbenchon, C. & Stallknecht, D. E. Strain-related variation in the persistence of influenza A virus in three types of water: distilled water, filtered surface water, and intact surface water. *Virology Journal* **10**, 13-13, doi:10.1186/1743-422X-10-13 (2013).

264 Lebarbenchon, C. *et al.* Viral Replication, Persistence in Water and Genetic Characterization of Two Influenza A Viruses Isolated from Surface Lake Water. *PLoS One* **6**, 1-8, doi:10.1371/journal.pone.0026566 (2011).

265 Moore, B. E. Survival of human immunodeficiency virus (HIV), HIV-infected lymphocytes, and poliovirus in water. *Applied and Environmental Microbiology* **59**, 1437-1443 (1993).

266 Nazir, J., Haumacher, R., Abbas, M. D. & Marschang, R. E. Use of filter carrier technique to measure the persistence of avian influenza viruses in wet environmental conditions. *Journal of Virological Methods* **170**, 99-105, doi:http://dx.doi.org/10.1016/j.jviromet.2010.09.007 (2010).

267 Nazir, J. *et al.* Long-Term Study on Tenacity of Avian Influenza Viruses in Water (Distilled Water, Normal Saline, and Surface Water) at Different Temperatures. *Avian Diseases* **54**, 720-724, doi:10.1637/8754-033109-ResNote.1 (2010).

268 Pietsch, J. P., Amend, D. F. & Miller, C. M. Survival of Infectious Hematopoietic Necrosis Virus Held Under Various Environmental Conditions. *Journal of the Fisheries Research Board of Canada* **34**, 1360-1364, doi:10.1139/f77-195 (1977).

269 Rabenau, H. F. *et al.* Stability and inactivation of SARS coronavirus. *Medical Microbiology and Immunology* **194**, 1-6, doi:10.1007/s00430-004-0219-0 (2005).

270 Sinclair, R., Boone, S. A., Greenberg, D., Keim, P. & Gerba, C. P. Persistence of Category A Select Agents in the Environment. *Applied and Environmental Microbiology* **74**, 555-563, doi:10.1128/AEM.02167-07 (2008).

271 Stallknecht, D. E., Goekjian, V. H., Wilcox, B. R., Poulson, R. L. & Brown, J. D. Avian Influenza Virus in Aquatic Habitats: What Do We Need to Learn? *Avian Diseases* **54**, 461-465, doi:10.1637/8760-033109-Reg.1 (2010).

272 Stallknecht, D. E., Shane, S. M., Kearney, M. T. & Zwank, P. J. Persistence of Avian Influenza Viruses in Water. *Avian Diseases* **34**, 406-411, doi:10.2307/1591428 (1990).

273 Toranzo, A. E. & Hetrick, F. M. Comparative stability of two salmonid viruses and poliovirus in fresh, estuarine and marine waters. *Journal of Fish Diseases* **5**, 223-231 (1982).

274 McDougal, J. S. *et al.* Thermal inactivation of the acquired immunodeficiency syndrome virus, human T lymphotropic virus-III/lymphadenopathy-associated virus, with special reference to antihemophilic factor. *Journal of Clinical Investigation* **76**, 875-877 (1985).

275 Brouwer, A. F. *et al.* Modeling Biphasic Environmental Decay of Pathogens and Implications for Risk Analysis. *Environmental Science & Technology* **51**, 2186-2196, doi:10.1021/acs.est.6b04030 (2017).

276 Carpenter, C., Fayer, R., Trout, J. & Beach, M. J. Chlorine disinfection of recreational water for Cryptosporidium parvum. *Emerging Infectious Diseases* **5**, 579-584 (1999).

277 Decrey, L., Kazama, S. & Kohn, T. Ammonia as an in-situ sanitizer: influence of virus genome type on inactivation. *Applied and Environmental Microbiology* **82**, 4909-4920, doi:10.1128/AEM.01106-16 (2016).

278 Kim, T.-D. & Unno, H. The roles of microbes in the removal and inactivation of viruses in a biological wastewater treatment system. *Water Science and Technology* **33**, 243-250 (1996).

279 Ward, R. L., Knowlton, D. R. & Winston, P. E. Mechanism of inactivation of enteric viruses in fresh water. *Applied and Environmental Microbiology* **52**, 450-459 (1986).

280 Gao, T. *et al.* Evaluation of the matrix effect of thermophilic anaerobic digestion on inactivation of infectious laryngotracheitis virus using real-time PCR and viral cell culture. *Bioresource Technology* **110**, 692-696, doi:http://dx.doi.org/10.1016/j.biortech.2012.01.166 (2012).

281 Pocock, D. H. & Garwes, D. J. The influence of pH on the growth and stability of transmissible gastroenteritis virusin vitro. *Archives of Virology* **49**, 239-247, doi:10.1007/bf01317542 (1975).

282 Brainard, J., Pond, K. & Hunter, P. R. Censored Regression Modeling To Predict Virus Inactivation in Wastewaters. *Environmental Science & Technology*, doi:10.1021/acs.est.6b05190 (2017).